
Physical Properties of Gas Hydrate Related Sediments, Offshore Vancouver Island

by

Ivana Novosel

B.Sc. Geology, McMaster University, 2000

A Thesis Submitted in Partial Fulfillment of the
Requirements for the Degree of

Master of Science

in the

School of Earth and Ocean Science

[REDACTED]
Dr. G.D. Spence, Supervisor (School of Earth and Ocean Sciences)

[REDACTED]
Dr. R.D. Hyndman, Member (Geological Survey of Canada)

[REDACTED]
Dr. T. S. Hamilton, Outside Member (Camosun College)

[REDACTED]
Dr. E. Van der Flier-Keller, Departmental Member (School of Earth and Ocean Sciences)

[REDACTED]
Mr. S. Dallimore, External Examiner (Geological Survey of Canada)


© Ivana Novosel, 2002

University of Victoria


All rights reserved. This thesis may not be reproduced in whole or in part, by photocopy or other means, without the permission of the author.

which use in situ thermal conductivity values, and 2) seafloor seismic impedance studies which depend on both velocity and density results, especially for higher frequency data which are more significantly affected by the properties of shallow sediments.

Examiners:



Dr. G.D. Spence, Supervisor (School of Earth and Ocean Sciences)




Dr. R.D. Hyndman, Member (Geological Survey of Canada)



Dr. T. S. Hamilton, Outside Member (Comosun College)



Dr. E. Van der Flier-Keller, Departmental Member (School of Earth and Ocean Sciences)



Mr. S. Dallimore, External Examiner (Geological Survey of Canada)

Supervisor: Dr. George D. Spence

ABSTRACT

A gas hydrate vent field on the South Vancouver Island continental slope was the target of a series of seafloor core sampling programs in years 2000 and 2001. The vent structures had been previously imaged on the Cascadia accretionary margin as prominent blank zones in seismic reflection data. In 2000, 26 piston cores, with maximum recovered lengths of approximately 8 m, were collected in the vent field region. Extensive physical property measurements were carried out on these cores. The objectives of the analyses were to: (1) provide ground-truth calibrations for seismic impedance and electrical resistivity remote surveys, and (2) examine the effect of high methane fluxes on the physical, chemical, and mineralogical character of sediments within the region of a vent field.

Gas hydrate was recovered in 4 cores located within the most prominent seismic blank zone (Blank Zone 1). Cores located within the blank zones contained low magnetic susceptibility authigenic pyrite, rather than high magnetic susceptibility magnetite and thus created a low magnetic zone within the vent. Leather clams (*genus acharax*) were recovered in several cores located inside the vent, indicating an environment high in sulfide. Increased seismic reflection coefficients and sample thermal conductivity values within the topmost sediments of Blank Zone 1 correlated with the presence of authigenic carbonate. All observations are consistent with high methane fluxes from seafloor sediments within a cold seep environment.

The comparison of core measured porosity, thermal conductivity, and velocity with physical properties from deeper in the stratigraphy from the Ocean Drilling Program (ODP) clearly indicates that within ~10 m of the seafloor sediment compaction is distinctly different from that indicated by deeper trends. Within these cored sediments porosity decreases from as much as 75% at the seafloor to 55% at 8 m below; in contrast, the porosities over this depth range extrapolated from the deeper ODP trends are consistently 60%. Thermal conductivity, being highly dependent on density and porosity, also increases dramatically within the top few metres of the sediment. However, no decrease in sample seismic velocity is observed over the same depth range. This particular behaviour of shallow sediments may be significant for: 1) heat flow studies

ACKNOWLEDGEMENTS

First and foremost I would like to thank my supervisor, Dr. George Spence and Dr. Roy Hyndman, for all their support, guidance, and understanding. Without them, this work could have not been accomplished as it did, and it definitely would not have been attained with as much enthusiasm and enjoyment. I would also like to thank Dr. Tark Hamilton for his great insight and all the valuable discussions on the various aspects of geology, sedimentology, geochemistry, and geophysics. I am also grateful to a member of my committee, Dr. Eileen Van der Flier-Keller, and to my External Examiner, Mr. Scott Dallimore, for their involvement and contributions to the thesis.

Furthermore, I am very thankful to Michael Riedel for all his help that he has provided (willingly) since the first day we started working together. One man without whom I would have never been able to collect so many successful cores and without whom I would have never fallen in love with marine research, and thus compromised the quality of this work, is Bob McDonald. I am also obliged to all the people that have helped me during the acquisition of this enormous data set, without whom I would have not been able to complete this thesis in the time given. These wonderful people are (in alphabetical order): C. Blay, M. Bolton, C. Currie, and S. Molnar. I wish to thank Dr. T. Lewis of GSC for his involvement with thermal conductivity data acquisition and analysis, J.S. Crockett and C. Nittrouer of University of Washington, Seattle, for providing and assisting with the MSCL equipment, as well as D. Mosher and K. Conway of GSC for all the help and assistance with the physical properties equipment.

I also wish to thank all the people that have kept me sane and somewhat sociable, especially: Johanna Hoenhe (my all around activity buddy), Sheri Molnar (the true Ontario buddy), Kumar Ramachandran (the philosophy buddy), as well as the rest of E-Hut (the party hut) and PGC (the outcastes). The last but definitely not the least, I must thank my boyfriend, Richard Fitton, and my parents, Dragutin and Ljubica Novosel, for their unconditional love, support, and understanding.

TABLE OF CONTENTS
CHAPTER 1

INTRODUCTION.....	1
1.1. GAS HYDRATES	1
1.1.1. Introduction.....	1
1.1.2. Gas Hydrate Structure and Stability	2
1.1.3. Sources of Methane.....	4
Thermogenic Methane	4
Biogenic Methane	4
1.1.4. Fluid and Gas Movement Within the Vent Fields	6
1.1.5. Gas Hydrate Detection Using Geophysical Methods	7
Bottom Simulating Reflector (BSR), AVO Analysis, and Wave-Form Inversion ..	7
Heat Flow	9
Downhole Logging Methods	11
1.1.6. Methods for Estimating Gas Hydrate Concentration.....	12
Geochemistry	12
Multichannel Velocity Analysis	13
Electrical Resistivity	14
1.1.7. Importance of Gas Hydrates	15
Energy Resource	15
Slope Stability	15
Climate Change.....	16
1.2. GEOLOGY AND TECTONICS OF THE STUDY AREA.....	19
1.3. PREVIOUS RELATED STUDIES OFFSHORE VANCOUVER ISLAND	22
1.3.1. ODP Leg 146	22
1.3.2. PGC96004 – Mi (1998) Study	23
1.3.3. Seismic Surveys	23
1.4. GENERAL DESCRIPTION OF THE STUDY.....	26
1.4.1. Introduction to Physical Properties.....	26
1.4.2. Objectives, Significance, and Contributions.....	27

CHAPTER 2

METHODS AND PHYSICAL PROPERTY MEASUREMENT.....	28
2.1. DATA ACQUISITION	28
2.1.1. Coring Cruise 2000 – PGC00-02.....	28
2.1.2. ROPOS Cruises 2000 and 2001	30
2.1.3. Gas Hydrate Recovery	33
2.1.4. Coring Procedure and Core Measurement Preparation	35
2.2. PHYSICAL PROPERTY MEASUREMENTS.....	36
2.2.1. Manual Physical Property Measurements.....	36
Magnetic Susceptibility	36
Thermal Conductivity	37
Electrical Resistivity	38
Compressional Velocity.....	40
Shear Strength.....	40

Bulk Density, Porosity, and Grain Density	41
2.2.2. Multi-Sensor Core Logger (MSCL).....	43
2.3. DATA CORRECTION.....	43
2.3.1. Density/Porosity Corrections for Missing Sediment Volume	43
UNDER-ESTIMATE	46
Scaling to Known Grain Density	50
2.3.2. Multi-Sensor Core Log (MSCL) Fractional Porosity Data Correction	53
CHAPTER 3	
OBSERVATIONS.....	55
3.1. PHYSICAL PROPERTIES.....	55
3.2. INDEX PROPERTIES	60
3.3. MULTI-SENSOR CORE LOGGER	63
3.4. SEDIMENTOLOGY	66
CHAPTER 4	
DATA SYNTHESIS – DISCUSSION	68
4.1. POROSITY PREDICTION VIA ARCHIE’S LAW	68
4.2. VELOCITY-POROSITY DATA ANALYSIS.....	72
4.3. THERMAL CONDUCTIVITY HIGH – PRESENCE OF AUTHIGENIC CARBONATE.....	77
4.4. HIGH REFLECTION COEFFICIENT ZONE – DISSEMINATED CARBONATE HYPOTHESIS	
81	
4.5. MAGNETIC SUSCEPTIBILITY ZONATION	85
4.5.1. Association of Low Magnetic Susceptibility with Presence of Pyrite.....	85
4.5.2. Magnetic Anomaly Expected From Low Magnetic Susceptibility Zone	91
CHAPTER 5	
CONCLUSIONS AND FUTURE RECOMMENDATIONS	93
5.1. GAS HYDRATE SURFICIAL ENVIRONMENTS	93
5.2. RECOMMENDATIONS FOR FUTURE WORK.....	95
5.2.1. Physical Properties.....	95
5.2.2. Marine Magnetic Anomaly	96
REFERENCES.....	97
APPENDIX A - CORE LOG.....	106
APPENDIX B - GENERAL CORE DESCRIPTION.....	111
APPENDIX C - SEDIMENTOLOGICAL CORE DESCRIPTION.....	113

LIST OF TABLES

Table 1. General hydrate description.....	33
Table 2. Percent change in values due to correction for core 21.....	42
Table 3. The effect of an estimate in the height of the unfilled plug.....	43

LIST OF FIGURES

1.1.	Structure I of the gas hydrate molecule	1
1.2.	Locations of known gas hydrate deposits worldwide	2
1.3.	Methane hydrate stability zone	3
1.4.	Methanogenic processes in anoxic conditions	6
1.5.	Multichannel seismic section showing BSR	8
1.6.	Heat flow values from Cascadia margin	10
1.7.	Relationship between fluid flow and seafloor topography	11
1.8.	Relationship between methane flux and sulfate replenishment	13
1.9.	$\delta^{13}\text{O}$ and paleo-temperature from various ice-core records	17
1.10.	An illustration of the “Clathrate Gun Trigger” hypothesis	18
1.11.	General tectonic setting of the Cascadia Subduction Zone	19
1.12.	Location of this study	20
1.13.	Marine seismic profile of the Cascadia’s sedimentary package	21
1.14.	DTAGS line showing blank zones 1 and 2	24
1.15.	Teledyne line SC-18 showing blank zones 1 and 2	25
2.1.	Core locations and previous seismic lines in the area	29
2.2.	Core locations and the extent of seismic blanking within Blank Zone 1	29
2.3.	Core locations and the extent of seismic blanking within Blank Zone 4	30
2.4.	ROPOS photos of vent environment	32
2.5.	Photo of hydrate sample	34
2.6.	Photo of gas expansion crack	34
2.7.	Typical split-core physical properties measurement order and position	39
2.8.	Original index properties for core 21	47
2.9.	Index properties corrected for missing sediment for core 21	48
2.10.	Index properties corrected for missing sediment for core 2	49
2.11.	Comparison of fractional porosity values for cores 2 and 21	50
2.12.	Index properties for core 9 after final correction	52
2.13.	MSCL fractional porosity data for core 19	54
3.1.	a) Physical property results for Blank Zone 1 cores	57

	b) Physical property results for Blank Zone 4 cores	58
	c) Physical property results for cores outside the vent field	59
3.2.	a) Index property results for Blank Zone 1 cores	61
	b) Index property results for Blank Zone 4 cores	62
3.3.	MSCL results for Blank Zone 1 cores	64
3.4.	Comparison of MSCL and manual data sets	65
3.5.	Sedimentological description of core 19	67
4.1.	Formation factor vs. fractional porosity for Blank Zone 1	69
4.2.	Comparison of measured and predicted porosity with depth for core 19	70
4.3.	Fractional porosity vs. formation factor for core 19 showing plug, MSCL, and predicted data sets	71
4.4.	Velocity vs. porosity for core 19	72
4.5.	Velocity vs. porosity for Blank Zone 1	74
4.6.	Athy's relationship	76
4.7.	Thermal conductivity with depth for Blank Zone 1	77
4.8.	a) Thermal conductivity with depth for Blank Zone 1	79
	b) Thermal conductivity with depth for Blank Zone 4	79
	c) Thermal conductivity with depth for cores outside the vent field	79
4.9.	Thermal conductivity vs. fractional porosity for Blank Zone 1	80
4.10.	Reflection coefficients along Transect 1 and Transect 2	82
4.11.	Density and velocity for cores with much different RC	83
4.12.	Surface RC of Blank Zone 1 calculated by Riedel (2001)	84
4.13.	Deep-tow seismic profile above Blank Zone 1	84
4.14.	a) Magnetic susceptibility along Transect 1	86
	b) Magnetic susceptibility along Transect 2	87
4.15.	3-D representation of magnetic susceptibility zonation at Blank Zone 1	88
4.16.	Photos showing authigenic pyrite	89
4.17.	Modeled magnetic anomalies due to low-magnetic susceptibility	92
5.1.	Proposed cold vent environment at Blank Zone 1	94

CHAPTER 1

INTRODUCTION

1.1. GAS HYDRATES

1.1.1. Introduction

Hydrates are a subgroup of clathrates, a compound formed by the inclusion of one type of molecule into the crystal lattice of another (e.g., Pellenbarg and Max, 2000). In the case of gas hydrates, a gas molecule, usually methane, is surrounded by the solid crystal lattice formed by water molecules (Figure 1.1). Until recently little was known about gas hydrates occurring in nature. One of the first gas hydrate deposits was discovered by Russian scientists in the Siberian permafrost sediments (Makogon *et al.*, 1972). They claimed that hydrate could represent a significant energy resource. This claim was initially opposed by other scientists, who believed it to be economically unfeasible (Stoll and Bryan, 1979), but there is now renewed interest.

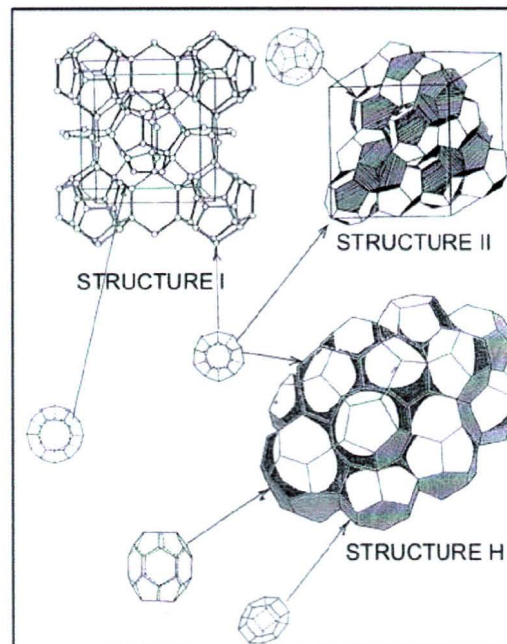


Figure 1.1 Gas hydrate molecular structures I, II, and H (after Sloan, 1998)

Since then, gas hydrate deposits have been discovered all over the world (Figure 1.2). Marine gas hydrates are mostly found in the upper few hundred meters below the sea floor along continental margins in water depths usually exceeding 500 m (Kvenvolden, 1998, 2000). Today, research on marine gas hydrates is justified because of their wide distribution and massive size of the associated methane reservoir, and because of their potential involvement in shaping the geology and climate of the past and their possible role in future climate change by being a large part of the global methane flux and budget. These topics will be discussed in more detail in the following sections.

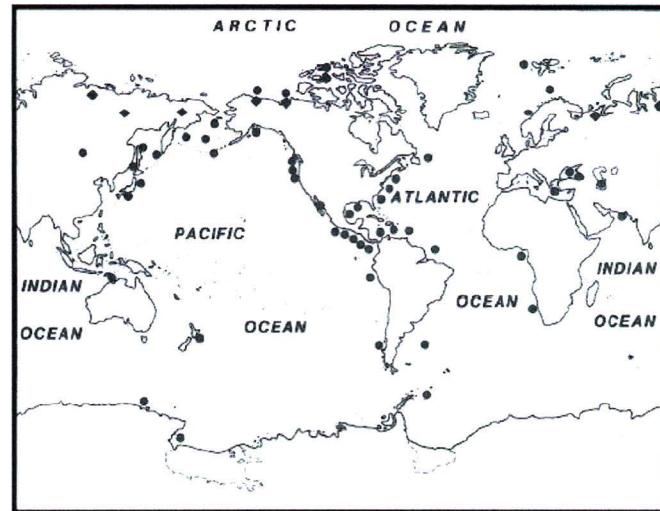


Figure 1.2 Locations of known gas hydrate deposits worldwide (from Kvenvolden, 2000)

1.1.2. Gas Hydrate Structure and Stability

Gas hydrates can form two cubic lattice structures, I and II, and one hexagonal structure, H (Sloan, 1998). Structure I is the most common structure, for which the body-centered packing permits methane, ethane, and other gas molecules of the similar size to be incorporated into the structure (Sloan, 1998). Structure II has water cages arranged in diamond packing which allows larger gas molecules such as propane and isobutane to be incorporated into the compound (Sloan, 1998). Structure H is the least known, as well as

least naturally observed structure, for which the cage is large enough to incorporate complex molecules such as naphtha and gasoline (Sloan, 1998).

The methane hydrate stability zone (MHSZ) is defined by temperature and pressure as well as fluid and gas composition. For the example of a water depth of ~ 1250 m, i.e., approximate water depth for this study area, methane hydrate occurrence is bounded by the seafloor and the intersection of the phase stability boundary with the geothermal temperature profile at ~ 1.6 km depth (Figure 1.3). In this case, gas hydrate will form only from the sea floor down to about 300 meters below the seafloor (mbsf). If the temperatures are too high, and/or pressures too low (i.e. outside the stability zone), the methane will be present as a free gas, if its concentration is greater than the solubility of methane in water. The boundary between sediments containing hydrate and underlying sediments containing water and free gas is usually observed to nearly follow a temperature isotherm, and can be detected as a strong negative reflector on marine seismic reflection profiles (Bottom Simulating Reflector Section).

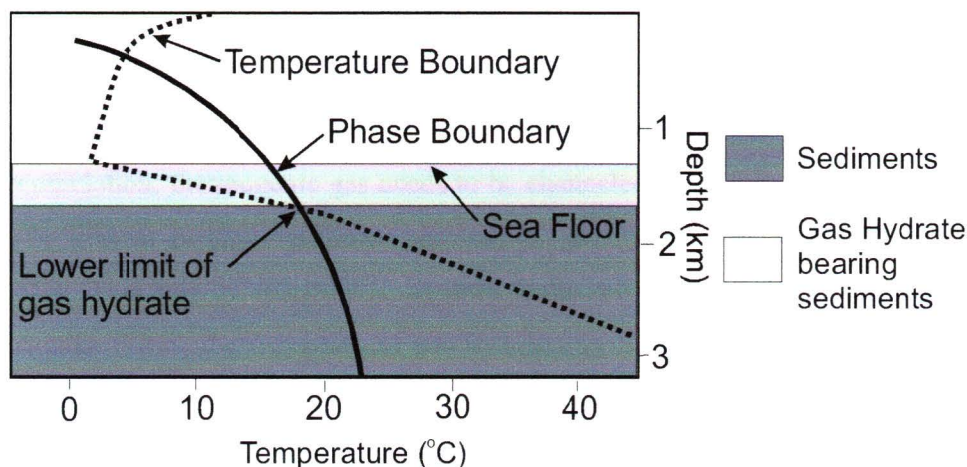


Figure 1.3. Methane hydrate stability zone with respect to temperature and pressure (after Dillon and Max, 2000)

Another essential factor in the formation of gas hydrate is the presence of adequate methane within the sediment (Dillon and Max, 2000). If the concentration of methane in the pore fluids is not approaching saturation, gas hydrate will not form even if the temperature-pressure conditions are ideal (Xu and Ruppel, 1999). Occasionally gas hydrate deposits will be observed at the seafloor. This will occur when the methane

supply from below is so high that it is not all removed to form hydrate in the underlying sediments. The methane saturates the pore water just below the seafloor and thus prevents the diffusion loss and dissociation of hydrate.

1.1.3. Sources of Methane

Thermogenic Methane

Thermogenic methane is formed from the thermal breakdown of organic matter. It is usually formed much deeper than the MHSZ and is related to petroleum accumulations (Kvenvolden, 1998). This type of methane is therefore often accompanied by higher hydrocarbons (Wellsbury and Parkes, 2000). The ratio of methane concentration to the concentration of higher hydrocarbons, or the C_1/C_{2+} ratio (where C_1 represents methane and C_{2+} represents any higher hydrocarbon), is used to characterize the quantity of higher hydrocarbons present within the gas. Thermogenic gases tend to have low C_1/C_{2+} ratios, with typical values less than one hundred (Matsumoto *et al.*, 2000). The carbon isotopic composition of thermogenic methane ($\delta^{13}C$) will be around -30‰ relative to the Peedee Belemnite (PDB) standard (Kvenvolden, 1998). Because only high and continuous concentrations of gas permit gas hydrate formation and accumulation, thermogenic gas needs to be channeled from deep source regions in order to be present in any significant amounts as gas hydrates (e.g., Hyndman and Davis, 1992). This may be observed along deep faults and fractures that act as fluid migration conduits. Thus, the formation of gas hydrates by thermogenic gases will be limited to these types of settings. A good example of gas hydrate deposits formed this way is in the Gulf of Mexico (MacDonald *et al.*, 1994). There, gas hydrates serve as a seal and form traps for thermal gas rising from underlying salt domes (Kvenvolden, 1998).

Biogenic Methane

Biogenic methane depends on bacterial activity at lower temperatures, and so can form in sediments within the MHSZ (Kvenvolden, 1998). Methane is the predominant hydrocarbon (over 99% of the gas hydrocarbon mixture) within the pore fluids affected by microbial production (Wellsbury and Parkes, 2000). Thus, the C_1/C_{2+} ratio of

biogenic methane is much higher than its thermogenic counterpart; it is typically around 10^3 and can reach as high as 10^5 (Matsumoto *et al.*, 2000). Moreover, its $\delta^{13}\text{C}$ is often smaller than -60‰ relative to PDB and thus $\delta^{13}\text{C}$ can be used in conjunction with C_1/C_2 ratios to discriminate between the two kinds of methane sources (Kvenvolden, 1998).

Oceanic gas hydrates are mostly formed by biologically derived methane (Kvenvolden, 1998). This methane is produced by methanogenic bacteria that break down organic matter to generate energy that is essential for their growth and survival (Wellsbury and Parkes, 2000). Methanogens, however, are only a small part to the whole process of bacterial decay of organic matter within anoxic conditions (Wellsbury and Parkes, 2000). They feed on the end products of the metabolism of other type of bacteria. Figure 1.4 illustrates the complex pathways involved in this type of decay. Anoxic decay is different from decay executed in oxic conditions, where one bacterium can complete the whole process.

Methanogens sometimes have to compete for substrate, and in the case of competition for hydrogen and acetate, they will often be excluded due to presence of sulfate-reducing bacteria (Wellsbury and Parkes, 2000). Methanogenic and sulfate-reducing bacteria do not exist in the same environment. Sulfate-reducing bacteria are often present in near-surface marine sediments (Borowski and Paull, 1996). Once the sediment becomes anoxic by initial organic breakdown, the bacteria will start depleting sulfate from the sediment (Berner, 1978). Once sulfate is depleted, the sulfate-reducing bacteria are excluded and the methanogens will initiate methane production (Berner, 1978). Because sulfate is being replenished from the seawater above, the amount of sulfate reduction will decrease with depth, inverse to the amount of methane production locally and transported from below (Borowski and Paull, 1996).

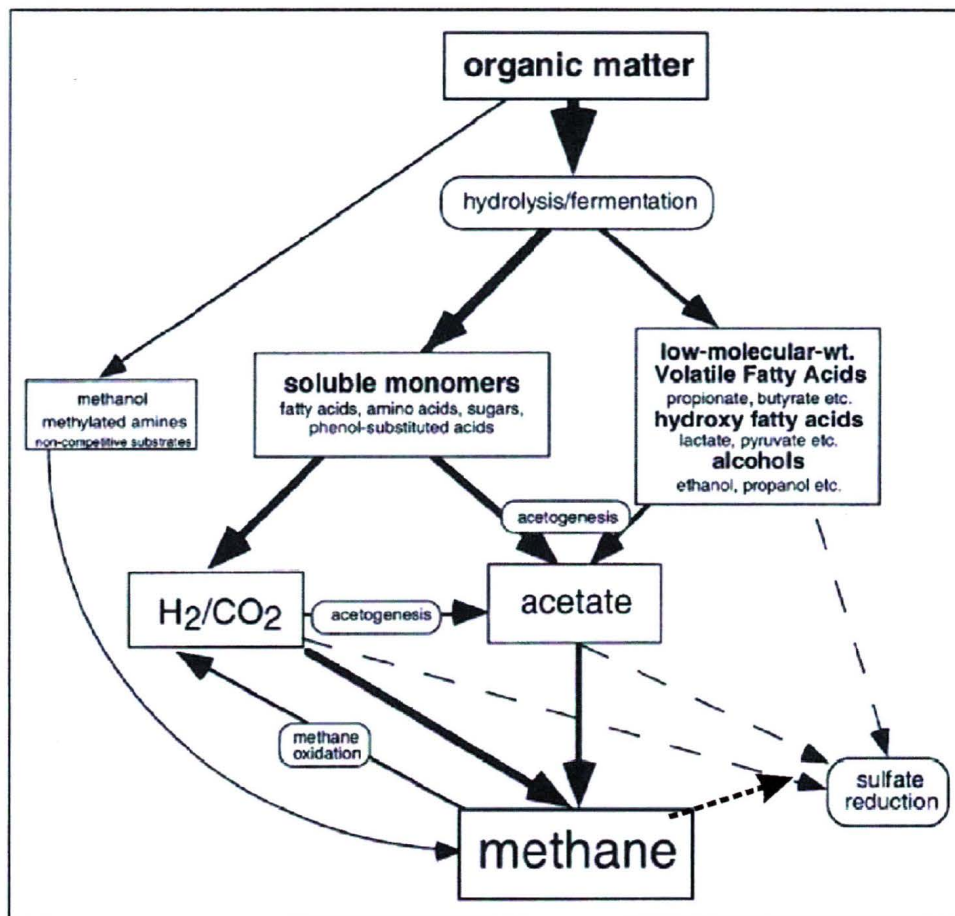


Figure 1.4. Processes making up methanogenesis in anoxic conditions of oceanic marine sediments. The thickness of arrows represents the relative importance of each process. Solid arrows represent pathways to methane and dashed arrows represent substrates to sulfate reduction (after Wellsbury and Parkes, 2000).

1.1.4. Fluid and Gas Movement Within the Vent Fields

Venting associated with accretionary sedimentary prisms at convergent boundaries differs substantially from the well-known mid-ocean ridge related venting. The vents are more scattered, the fluids and gases expelled are colder, and unlike hard basalt, soft accretionary sediments are the main matrix through which fluids and gas travel. Unfortunately, cold vents at convergent boundaries are less studied and understood than hot vents at ridges.

There are two main types of fluid/gas upward migration within the accretionary prism: distributed migration through the sedimentary matrix, occurring over a large area,

and focused migration, occurring along cracks and faults within the sediment matrix. Focused flow can be detected by locating thermal anomalies within sediments close to the vent (e.g. Ganguly *et al.*, 2000), by locating large bioherms that result from increased sulfide and methane flux (e.g. Sibuet and Olu, 1998), by visually observing the vent structures, and by measuring migrating fluid/gas exiting from the vent (Kastner *et al.*, 1995). Distributed fluid/gas migration is more difficult to detect and quantify. Although the amount of fluid/gas flux can be large, since it is widely distributed, the flux at a given location appears to be quite small. Thermal anomalies are poorly defined, venting sites are not visible, and the biological indicators are likely not present. This leaves the widespread presence of BSR (Bottom Simulating Reflector) as a key indicator of distributed upward flow (Hyndman and Davis, 1992). One commonality between the two types of flow is the formation of the authigenic carbonates near the sea floor. The increased methane flux associated with these environments will promote bacterial activity (see section 1.1.3), oxidizing methane to carbon dioxide which will then react with calcium, magnesium from seawater and pore fluids to precipitate carbonates.

1.1.5. Gas Hydrate Detection Using Geophysical Methods

The widespread detection and study of marine gas hydrates has largely relied on remote geophysical techniques. At present, the most common geophysical technique used in gas hydrate research is the marine seismic reflection method. This technique detects the impedance contrast between normal sediments and sediments containing gas hydrate or free gas and may provide seismic velocity information. Other important remote geophysical methods include seismic refraction, electrical profiling, and heat flow. Gas hydrates can also be detected through direct methods such as drillhole log analysis and coring, although in marine studies these are commonly secondary methods following a remote detection technique.

Bottom Simulating Reflector (BSR), AVO Analysis, and Wave-Form Inversion

During the 1970's, it was recognized that certain seismic reflections paralleling the seafloor are somehow related to gas hydrates (e.g. Markl *et al.*, 1970; Shipley *et al.*,

1979). This reflector was named a bottom simulating reflector or BSR (Figure 1.5). The following characteristics of BSR were summarized by Hyndman and Spence (1992): 1) in comparison to the reflection from the sea floor, the BSR has a reversed polarity, thus indicating a lower impedance below the BSR; 2) the reflection coefficients are often large, implying a large impedance contrast at the boundary; 3) a single pulse character of the BSR reflection implies a simple interface at seismic wavelengths. The exact nature of the interface is somewhat unclear. However, it is currently believed that the BSR marks the top of the free gas layer and possibly the base of the MHSZ (e.g. MacKay *et al.*, 1994; Fink and Spence, 1999).

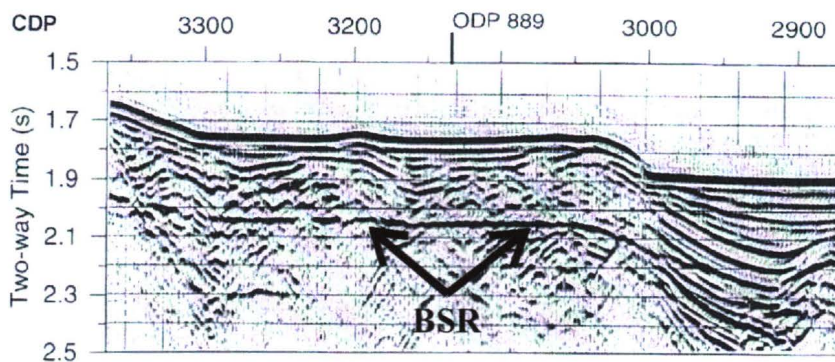


Figure 1.5. Multichannel seismic section showing BSR near ODP site 889 (from Spence *et al.*, 2000)

Hyndman and Spence (1992) used amplitude-versus-offset (AVO) analysis as an indicator of free gas at the base of the gas hydrate zone. This method is commonly used in hydrocarbon exploration because reflection angle variation in amplitude depends on velocity, density, and especially Poisson ratio contrasts. The presence of gas within the pore spaces of the sediment will greatly affect the Poisson ratio and cause an increase in amplitude with offset. In theory, an increased amount of free gas within the sediments will cause an increase in the magnitude of the near-offset reflection coefficient (Carcione and Tinivella, 2000). However, Riedel (2001) concludes that AVO will not always be able to discriminate between the presence and absence of small amounts of hydrate at the boundary. This is because the difference in density between a sediment with small

amounts of gas and sediment with small amounts of hydrate are negligible. The negative impedance contrast associated with the BSR is almost entirely due to P-wave velocity changes across the interface.

Better understanding of sedimentary sections underlying the BSR can be achieved through Ocean Bottom Seismograph (OBS) data analysis (Tinivella and Accaino, 2000). Unlike the conventional reflection profiles, the refracted waves can provide constraints on sediment velocities above and below the BSR. Tinivella and Accaino (2000) successfully used joint inversion of reflection and wide-angle travel times. They were able to identify the presence of gas hydrates through positive velocity anomalies, the presence of free gas below the BSR seen as a low velocity zone, and the base of the free gas zone through increased velocities below.

Heat Flow

Heat flow data can also be used to study controls of gas hydrate stability. Ganguly *et al.* (2000) showed a possible relationship between heat flow, gas hydrate fluid migration, and topographic features found on the Cascadia margin (e.g. accretionary ridges, thrust faults, extensional faults and folds). Figure 1.6 shows low heat flow values above topographic highs, caused by underthrusting of cooler, surface sediments, and high heat flow values above flanks of the topographic highs. The authors concluded that simple focusing and defocusing of heat flow due to various geological and topographic features is responsible for a portion of these observations (Figure 1.7).

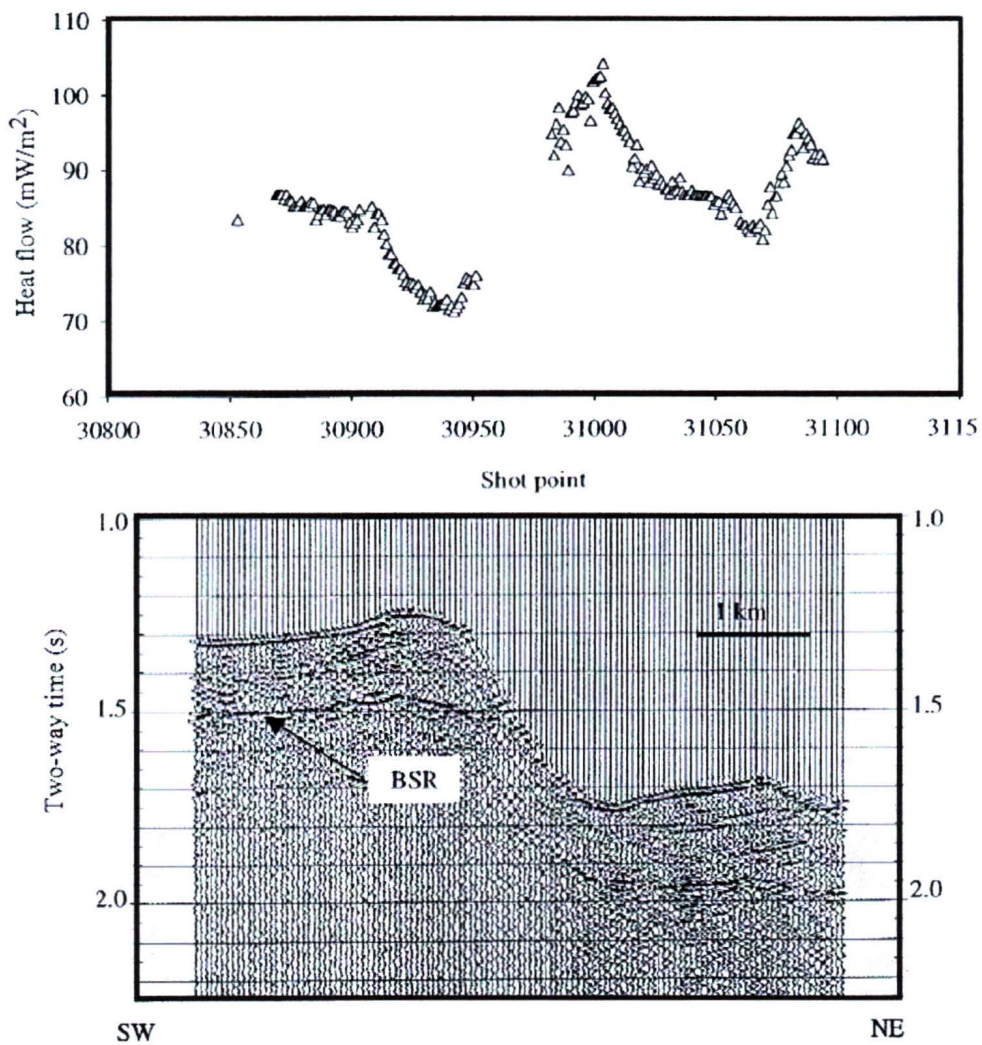


Figure 1.6. Heat flow values (top) over topographic highs seen on the migrated seismic section (bottom) from Cascadia margin (from Ganguly *et al.*, 2000).

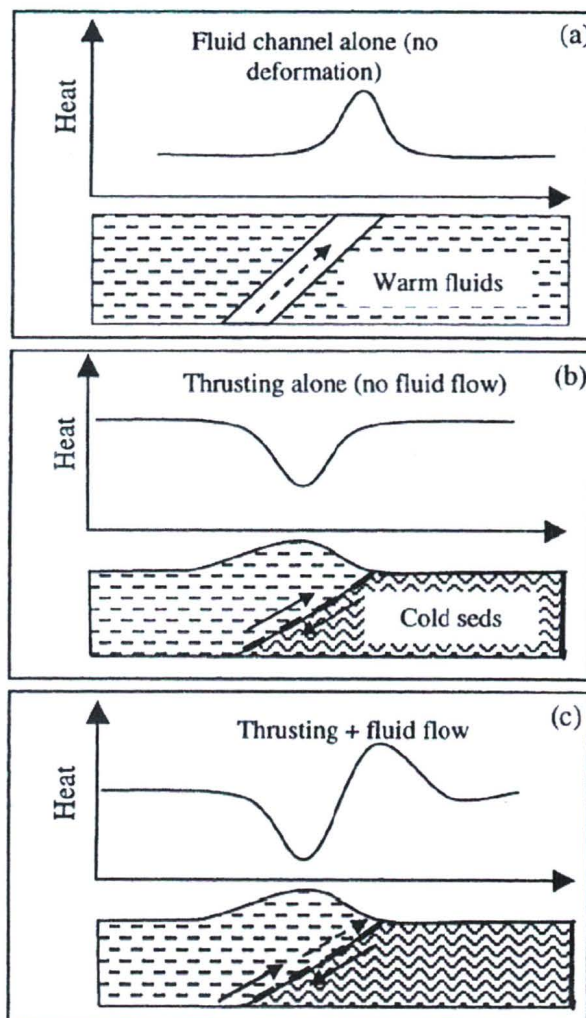


Figure 1.7. Schematic diagram showing the effect of topography on superficial heat flow. a) High heat flow caused by upward migrating warm fluids; b) lowered heat flow due to subsidence of colder sediments through thrust faulting; c) mixed heat flow when both thrusting and upward fluid flux are present (from Ganguly *et al.*, 2000).

Downhole Logging Methods

Downhole logging methods are very important in gas hydrate studies because they provide fine scale information about the in-situ sediment and gas hydrate properties and also serve as a calibration for remote geophysical surveys. Seismic velocity and

electrical resistivity have also been used to estimate gas hydrate concentration (see Methods for Estimating Gas Hydrate Concentration section).

Collett (1983) summarized common logging methods and their responses in gas hydrate environments. For example, electrical resistivity of partly gas or gas hydrate saturated sediment will be higher than sediments saturated only with sea water. Also, a less negative spontaneous-potential can suggest a presence of gas hydrate zone when compared with an underlying free gas zone, and acoustic transit time will be shorter when passing through gas hydrate layer than through normal sediment or free gas layer.

1.1.6. Methods for Estimating Gas Hydrate Concentration

Geochemistry

During gas hydrate formation within an open system, salt is excluded from the gas hydrate structure (Zatsepina and Buffett, 1999). Thus, when gas hydrate is removed out of its stability field by coring, it will dissociate and create pore water freshening. One can then estimate the amount of dissociated gas hydrate from the salt dilution, usually estimated through measurement of chlorinity of pore fluids extracted from the core samples (Hesse and Harrison, 1981). However, this technique does not take into consideration that there could be some salt trapped in the hydrate structure or between hydrate grains left from being excluded from forming hydrate (Yuan *et al.*, 1996).

Borowski *et al.* (1996) examined a possibility of using pore water sulfate profiles in identifying the presence and estimating the amount of gas hydrate. The sulfate profiles beneath the seafloor from the areas where gas hydrate is not present display curved convex-up shape, representing sulfate depletion by bacteria (Borowski *et al.*, 1996). The authors find that the sulfate profiles from the areas above gas hydrate deposits do not follow this trend and appear to be linear in shape. They propose that the mechanism driving this relationship is anaerobic methane oxidation from below. The linear shape of the profile is due to the 1:1 stoichiometric consumption of methane and sulfate presented below (Ritger *et al.*, 1987; Solem *et al.*, 2002):



A schematic diagram illustrating this phenomenon is shown in Figure 1.8. Borowski *et al.* (1996) conclude that steeper gradients imply more dissolved methane due to higher upward methane flux rates and thus can be used as proxy for the amount of gas below the sulfate reduction zone and to estimate the upward fluid expulsion rates.

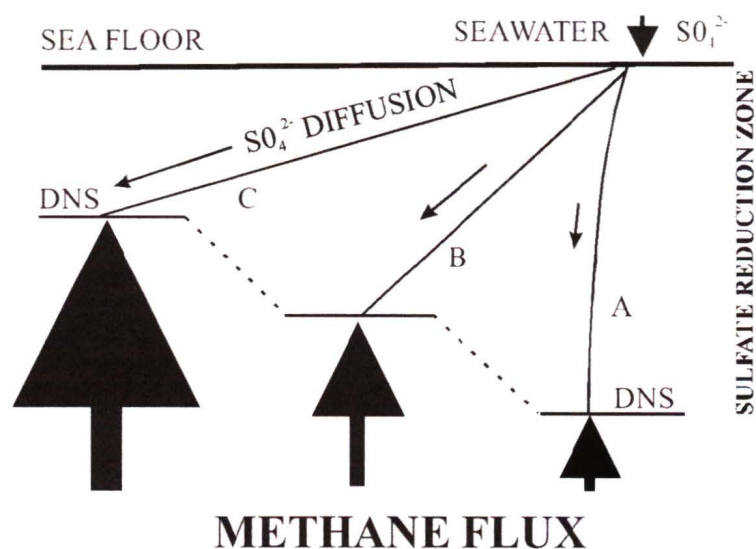


Figure 1.8. Schematic diagram showing upward methane migration and its impact on depth to no sulfate (DNS). Sizes of the arrows are proportional to methane flux. A) Typical, convex-up profile resulting from sulfate reduction of in-situ organic matter; B) and C) Linear profiles represent focussed sulfate consumption due to methane flux from below (from Borowski *et al.*, 1996).

Multichannel Velocity Analysis

Yuan *et al.* (1999) attempted to use the increase in velocity associated with gas hydrates to estimate its concentrations in the Cascadia region. Better constrained velocities allow more accurate velocity-depth reference models and thus can improve estimates of the quantity of gas hydrates within the MHSZ. Using detailed semblance velocity analysis Yuan *et al.* (1999) showed that in areas where gas hydrates are present, sediment velocities increase more rapidly with depth. They discovered that velocities increase from around 1500 m/s at the sediment-water interface, to a maximum of 1900 m/s immediately above the BSR, and then drop to 1700 m/s below the BSR and below

the thin free gas region. Using these velocity values, it was estimated that 10-25% of gas hydrate occupies the pore spaces of the underlying sediment in the region of ODP Site 889.

Electrical Resistivity

Electrical resistivity can be used to calculate concentration of gas hydrate within the sediment because hydrate is more resistive than the pore fluid it replaces. Hyndman *et al.* (1999) describe one method for calculating gas hydrate concentration from downhole log resistivity and core sample pore fluid salinity data. The method utilizes Archie's Law assuming that the effect of gas hydrate formation is simply that of porosity reduction, i.e., hydrate is effectively entirely resistive. For gas hydrate concentration calculation from downhole resistivity logs,

$$R_{fm} = aR_{in\ situ\ fl} [(1-S)\phi]^{-m}$$

where R_{fm} is the in situ formation resistivity at each depth, $R_{in\ situ\ fl}$ is the in situ pore fluid resistivity, S is the gas hydrate saturation, and ϕ is the sediment porosity at a given depth. $R_{in\ situ\ fl}$ is calculated through fluid salinity concentrations via following expression,

$$R_{in\ situ\ fl} = (C_{sw}/C_{in\ situ\ fl})R_{sw}$$

where, $C_{sw}/C_{in\ situ\ fl}$ is the conductivity ratio of reference seawater salinity to the in situ pore fluid, and R_{sw} is the resistivity of the reference seawater for a given temperature and depth.

As mentioned, pore water freshening occurs due to hydrate dissociation in recovered cores. Hyndman *et al.* (1999) describe this method where,

$$C_{core\ fl}/C_{in\ situ\ fl} = (1-S)$$

where, $C_{core\ fl}/C_{in\ situ\ fl}$ is the ratio of the core pore fluid salinity to salinity of the in situ pore fluid. Thus,

$$R_{in\ situ\ fl} = (1-S)(C_{sw}/C_{core\ fl})R_{sw}$$

Others have used a simplified version of the method proposed by Hyndman *et al.* (1999), by assuming that pore water salinities remain constant with depth (e.g. Collett and Ladd, 2000; Collett, 1998).

1.1.7. Importance of Gas Hydrates

Energy Resource

One of the most quoted estimates for the total volume of gas hydrate deposits is given by Kvenvolden (1988) stating that the global gas hydrate reserve represents approximately 10^4 gigatonnes of carbon (e.g., Haq, 1998). This is more than the estimated total volume of organic carbon in the world today and more than double that of all the carbon from known fossil fuel resources (Haq, 1998). However, hydrate recovery is hindered by their instability at standard temperature and pressure. During recovery, gas hydrates are taken out of their stability zone, and they quickly start to dissociate. Technology that can capture the escaping gas is still in its developing stages. Another possible solution to this problem is to design machinery that will simulate the temperature-pressure conditions found within the MHSZ and to allow drilling and transporting of gas hydrates without dissociation. However, drilling and recovering under these conditions might be too slow and too expensive, and thus economically unfeasible.

Slope Stability

Gas hydrate dissociates when exposed to temperatures and pressures out of its stability zone. As it dissociates, it releases methane gas and water. Because methane and water in the solid phase are smaller in volume, gas hydrate dissociation will cause an overall increase in sediment volume (Dillon and Max, 2000). An increase in volume, an addition of water and gas, and the increase in overall pressure increases the internal pressure in the pore spaces of the sediment and lowers the shear strength of the surrounding sediments (Dillon and Max, 2000; Paull *et al.*, 2000). The decrease in shear strength of the sediments may then initiate slope failure (Paull *et al.*, 2000).

There are different scenarios that could initiate gas hydrate dissociation and thus slope failure. An increase in water temperature, due to global warming for an example, will warm up the sediments and cause the stability zone to shift shallower into the sediments. However, because sediments are relatively good thermal insulators, the only hydrates affected by this change will be the ones situated close to the sea floor (Paull *et*

al., 2000). Another process causing gas hydrate dissociation is change in pressure. This can happen by removing overlying sediment and/or water load. Thus, changes in sea level could ultimately initiate slope failures in areas of gas hydrate deposits. Once a slide is initiated, either by temperature or pressure changes, it may incorporate some sediment load from the surrounding area and thus create cascading events (Dillon and Max, 2000).

Studying slope failure events and looking for evidence of their triggers is difficult. Most of the slide scars and canyons were formed a long time ago and have been altered by various seafloor processes since then. Furthermore, knowledge of the exact climate and ocean conditions at the time of their formation is usually poorly constrained. Paull *et al.* (2000) mention various studies of slope scars that are currently believed to have been initiated by gas hydrate decomposition. Most of those cases come from the US Atlantic margin where over 200 slump scars have been mapped. The scars occur in a region where gas hydrates are present and the BSRs can be directly related to the scar. Moreover, there is a correlation between known lowerings of the sea level and the frequency of slope failure occurrence (Paull *et al.*, 2000). However, testing this theory is complicated by the fact that sometimes lowering of the sea level can cause increased sedimentation in the same area, which can also initiate slope failures (Paull *et al.*, 2000).

Climate Change

Another currently debated gas hydrate topic is their influence and reaction to changes in climatic conditions. Even the most conservative estimates of the total volume of gas hydrates deposits are extremely large. Methane is a very effective greenhouse gas, almost twenty times more effective than carbon dioxide (Kvenvolden, 1998). If allowed to enter the atmosphere, it has the potential to cause global warming, or magnify already initiated warming trends.

Studies of the ice-core records have revealed that there is a correlation between the climatic warming and the amount of methane and carbon dioxide in the atmosphere (Figure 1.9) (Blunier, 2000). However, it is still unclear which came first, methane in the atmosphere or global climate warming (i.e. whether the increase in temperatures caused dissociation of gas hydrates and thus release of methane into the atmosphere, or whether

a decrease in water depth, i.e., pressure, caused the release of methane into the atmosphere which then caused climate warming).

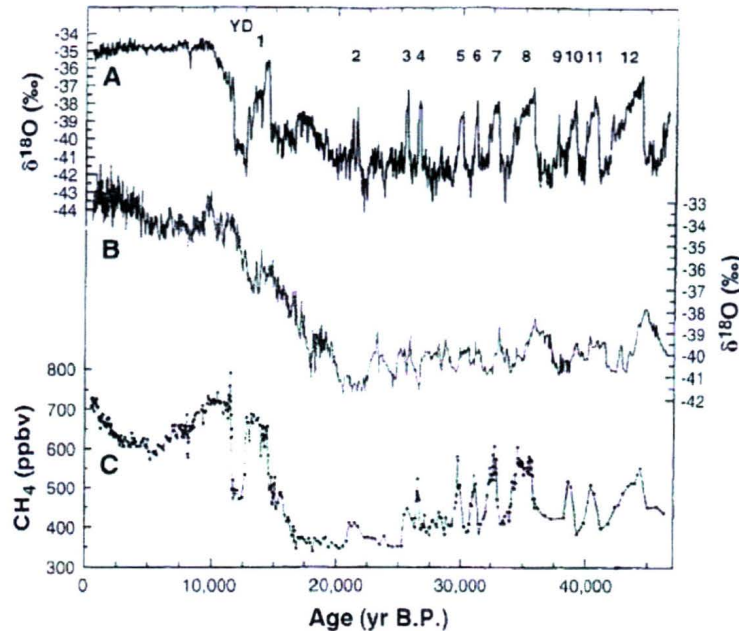


Figure 1.9. $\delta^{18}\text{O}$ (temperature indicator) changes in ice-core record from: a) Greenland, and b) Antarctic. c) Methane fluctuations in the Greenland core. Numbers at the top represent Dansgaard/Oeschger cycles, and YD stands for Younger Dryas event (from Blunier, 2000)

Some studies have correlated an initiation of glacial periods with increased slumping and thus release of methane from gas hydrates (e.g. Paull *et al.*, 1991). As the glaciers grow in size and water is removed from the oceans, the sea levels in low latitude regions drop, decreasing water pressure at the seafloor, and thus creating slumping and release of methane into the atmosphere. The increased atmospheric methane can then initiate a temperature increase, thus terminating glaciation. Paull *et al.* (1991) attribute this scenario to sharp terminations of Pleistocene glaciations including the Younger Dryas event.

There are several problems with this theory, however. It has been found from direct observations and modeling that as methane encounters the water-sediment interface it is oxidized and consumed in formation of sea floor carbonates (Haq, 2000). Significant

amounts of methane can only reach the atmosphere if the release from the gas hydrates is abrupt and massive in volume (Haq, 2000). Furthermore, there have been difficulties paralleling the time lag between glacial period initiation and periods of slumping, and between periods of slumping and climate warming.

Another more controversial view on this subject, the “clathrate gun trigger” suggests that methane release from gas hydrates is more evident during interstadials (Figure 1.10) (Kennett *et al.*, 2000). Their conclusions were based upon $\delta^{13}\text{C}$ signatures in benthic and planktonic foraminifera collected from the anoxic Santa Barbara Basin, off California. The authors stated that a temperature increase during interstadials can cause rapid release of methane and thus further temperature increase. It is possible that an increase in bottom water temperature of around 2-3°C is substantial enough to cause significant methane hydrate instability.

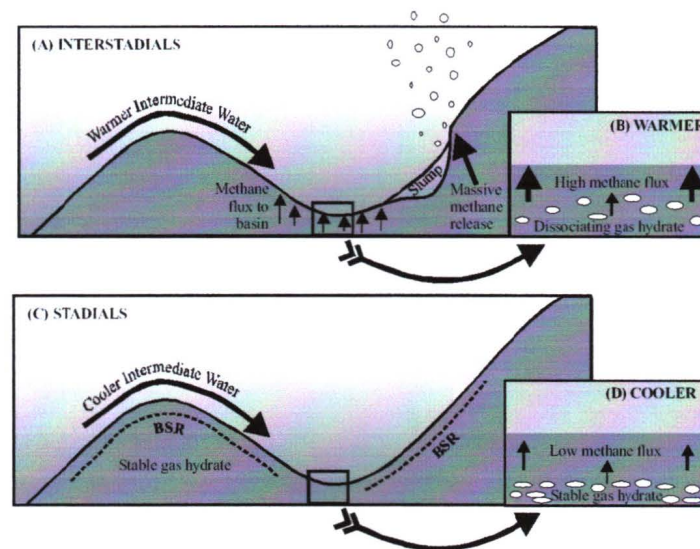


Figure 1.10. An illustration of the “Clathrate Gun Trigger” model proposed by Kennett *et al.* (2000), showing the influence of changing temperatures within the ocean on gas hydrate instability during interstadials (A and B) and stadials (C and D).

Hinrichs (2001) presented molecular paleontological data from the same basin showing alternating periods of high methane and low methane concentrations in the water. Because the periods of high methane concentrations are thought to have occurred during interstadials, this could serve as direct evidence supporting the “clathrate gun trigger” scenario. However, methane increase observed in Hinrichs (2001) study only represents a methane increase in ocean water, and there is no evidence that any reached the atmosphere. Many who disagree with Kennett and others (2000) agree that most of the methane released due to temperature warming would be consumed in carbonate production, and thus never enter the atmosphere (e.g. Dickens, 2000).

1.2. GEOLOGY AND TECTONICS OF THE STUDY AREA

The area of the current study is located on the Cascadia accretionary margin off Vancouver Island, BC, Canada (Figure 1.11 and 1.12).

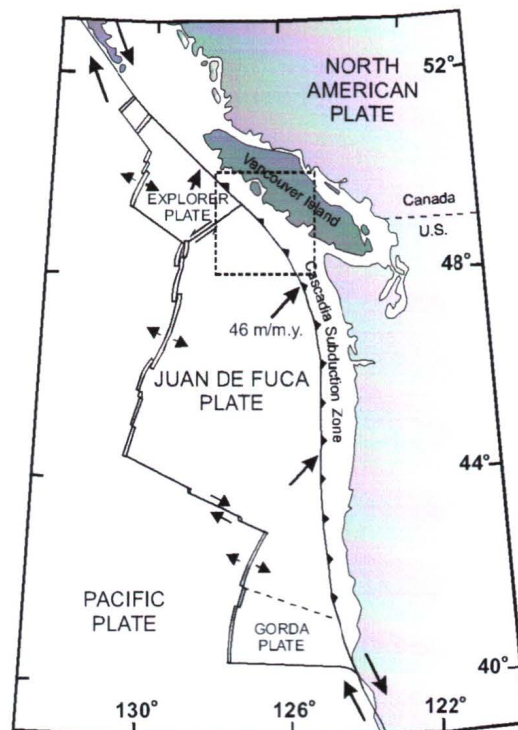


Figure 1.11. General tectonic setting of the Cascadia Subduction Zone. Outlined is the area of this study as shown in figure 1.12.

The tectonic activity of this area is produced by interactions between the Pacific, North America, and Juan de Fuca plate system (Figure 1.11). The Juan de Fuca plate system consists of several subplates (Explorer, Juan de Fuca, and Gorda). Presently, the Juan de Fuca plate is converging towards the North American plate at an approximate rate of 45 mm/a (Riddihough, 1984). In mantle-hot spot reference frame, the North America plate is moving in a westerly direction at a rate of 22 mm/a and is thus overriding the Pacific plates (Riddihough, 1984). It is believed that this plate regime has not significantly changed over the last 10 Ma and thus the overriding has resulted in a shallow subduction angle of the downgoing Juan de Fuca plate (Hyndman, 1995).

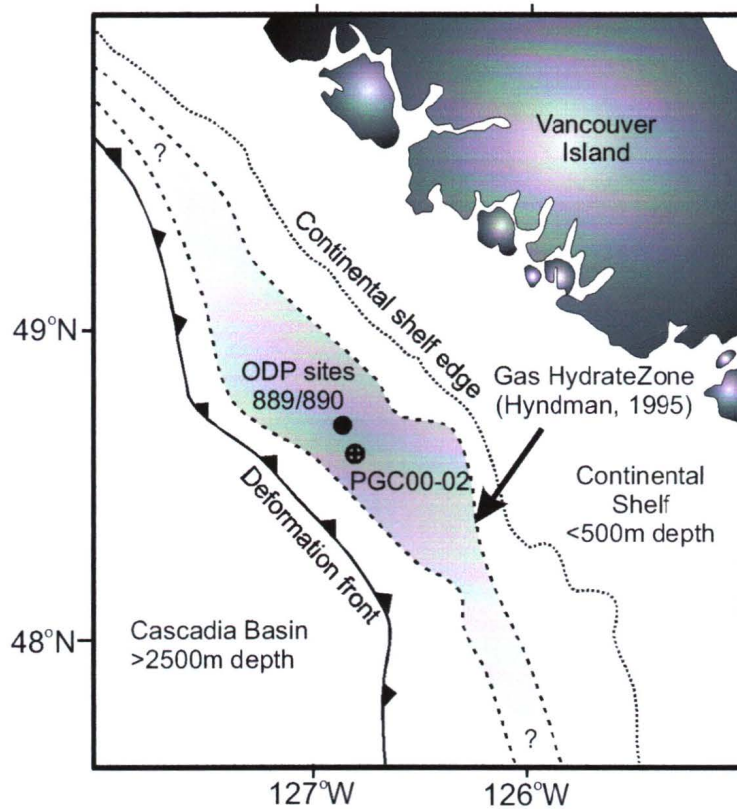


Figure 1.12. Map showing the location of this study (PGC00-02). Also shown are the ODP Leg 146 sites 889/890 and an approximate area of the gas hydrate occurrence based on the presence of a bottom simulating reflector (BSR).

The study site is on the large sedimentary prism that has formed as a result of almost complete accretion of the incoming subducting sedimentary cover. The 2-3 km thick incoming sedimentary package consists of layered Pleistocene turbidites, which are overlying pre-Pleistocene hemipelagic sediments (Figure 1.13). The sediments around the deformation front have been subjected to folding and faulting and are now forming anticlinal, approximately 700m-high ridges, which are sub-parallel to the margin. The large thickness of the incoming sedimentary section and the relatively young age of the subducting oceanic crust (approximately 6 Ma) have constrained the maximum water depth above the deformation front to 2.5 km (Hyndman, 1995). Just landward of the deformation front, around the area of this investigation, the water depth is further reduced by sediment prism thickening to about 1.5 km (Figure 1.13).

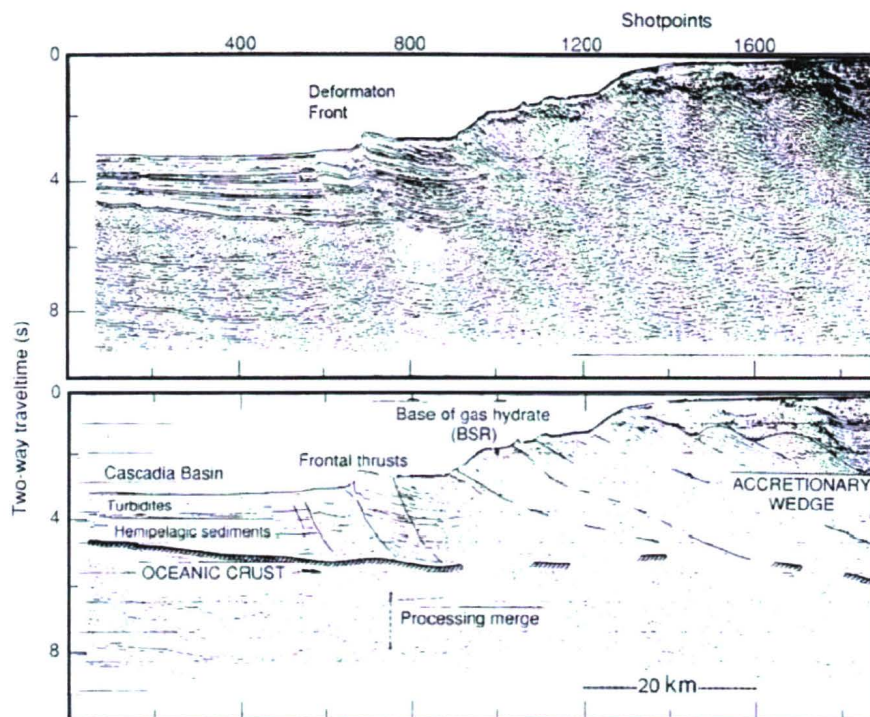


Figure 1.13. Multichannel reflection profile across the southern Vancouver Island margin (after Hyndman, 1995)

1.3. PREVIOUS RELATED STUDIES OFFSHORE VANCOUVER ISLAND

1.3.1. ODP Leg 146

In 1992, the Cascadia margin was investigated during Leg 146 of the Ocean Drilling Program (ODP). The primary objective of this leg was to study upward fluid flow and deformation of sediments within the accretionary wedge and their role in hydrate formation (Westbrook *et al.*, 1994). Specific attention was given to investigation of the BSR within the region (Westbrook *et al.*, 1994). Two sites were drilled in the vicinity of the current study (Figure 1.12). Drill sites 889 and 890 were located 4 km apart, on the continental slope of the Cascadia margin at a depth of approximately 1320 metres below sea level (mbsl).

The ages of sediments in this slope basin area spanned from Pleistocene to Holocene (Chamov and Murdamaa, 1995). The top-most unit was mostly composed of gray to olive gray finely laminated clayey silts and silty clays. Occasionally, millimetre- to centimetre-thick sandy as well as chlorite- and glauconite-rich, greenish and sulfide-rich black layers would occur. The sandy layers were mainly composed of angular to subrounded quartz, feldspars, lithic fragments, amphibole, and various opaque minerals. Clays were composed of various clay minerals which were commonly observed as flocculated aggregates.

The pore geochemistry results indicated that the depth to no sulfate occurred at approximately 10 m below the sea floor. As the sulfate concentration decreased downward in this zone, alkalinity and methane concentrations substantially increased. The ratio of methane to ethane (C_1/C_2) was greater than 10^3 within this zone which indicated a biogenic source (Westbrook *et al.*, 1994).

The BSR at site 889 was found at approximately 220 mbsf (Westbrook *et al.*, 1994). The Vertical Seismic Profiling (VSP) data showed a steady increase in velocity from the seafloor down to the BSR, and a sharp decrease in velocity below the BSR. This low velocity layer was attributed to the presence of free gas below the BSR (MacKay *et al.*, 1994). Solid gas hydrate was not observed at either drill site; however, sediment temperatures 10°C lower than expected were observed in cores taken near the

BSR (Westbrook *et al.*, 1994). The solid gas hydrate most likely dissociated due to pressure and temperature changes upon core recovery.

1.3.2. PGC96004 – Mi (1998) Study

In 1996, a detailed geophysical study was carried out by the University of Victoria and the Geological Survey of Canada in the vicinity of the ODP sites 889 and 890. The objectives of this study were to determine the lateral variation of the Cascadia gas hydrate through recording of short-offset Multi-Channel Seismic (MCS) data, and to examine physical properties of shallow sediments through the collection of piston cores (Mi, 1998).

During this study, a total of 18 cores were collected for physical property examination. The physical property suite included electrical resistivity, velocity, and density/porosity measurements. This was conducted in two stages. Seven cores were examined approximately 1-2 months after their recovery while the other 11 cores were examined almost a year after their recovery. Mi (1998) concluded that there was a noticeable discrepancy in resistivity measurements between the two data sets and was not confident in the results from the later examined cores which had probably partially dehydrated. The physical property results of the first seven cores mostly agreed with the ODP results from sites 889 and 890.

1.3.3. Seismic Surveys

In 1997, a deep towed multichannel seismic survey was conducted by deploying the Deep Tow Acoustic Geophysics System (DTAGS) off Vancouver Island. Several areas of reduced seismic reflectivity, later named 'blank zones', were observed (Figure 1.14). The largest blank zone, Blank Zone1, was seen to extend from the seafloor to approximately 150 mbsf, with a diameter of about 200 m (Riedel, 2001).

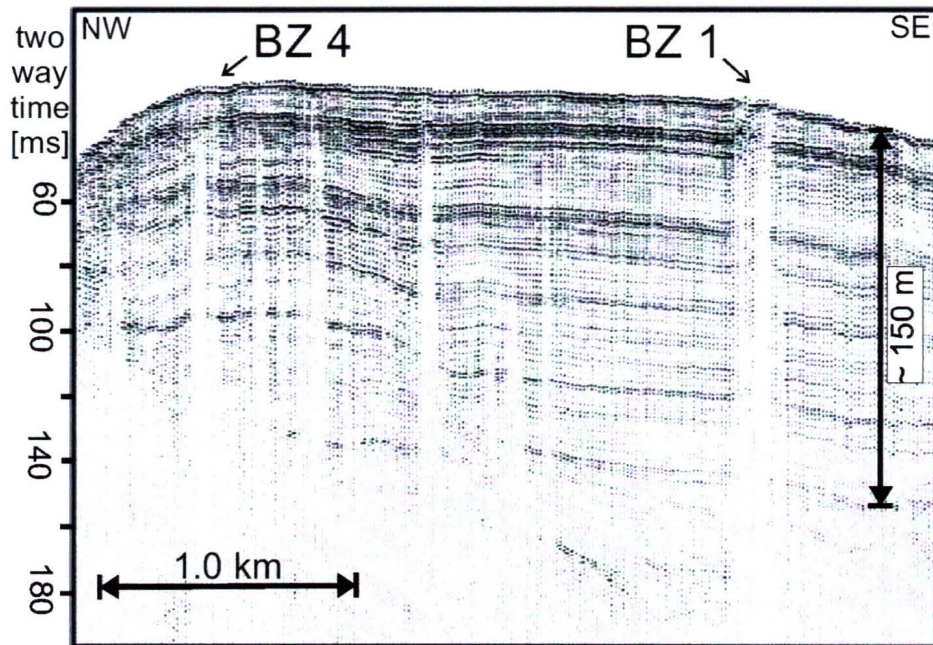


Figure 1.14. DTAGS line showing four blank zones (blank zones 1 and 4 are the focus of this study). The location of the line can be seen in figure 2.1 (equivalent to inline 27). Note approximate 10:1 vertical exaggeration. (After Riedel, 2001)

In 1999, the same area was further investigated during a multichannel 3-D seismic survey using Canadian Ocean Acoustic Measurement System (COAMS) and the Teledyne single channel streamer with an airgun source. Several multichannel seismic lines focused on the previously discovered blank zones. The diffraction hyperbola and the pulled up sedimentary layers are visible on both COAMS and Teledyne data (Figure 1.15). Riedel (2001) suggests that this increase of 5 to 10 ms in two-way-time (TWT) is likely due to either higher velocities, real deformation, or seafloor topographic effects.

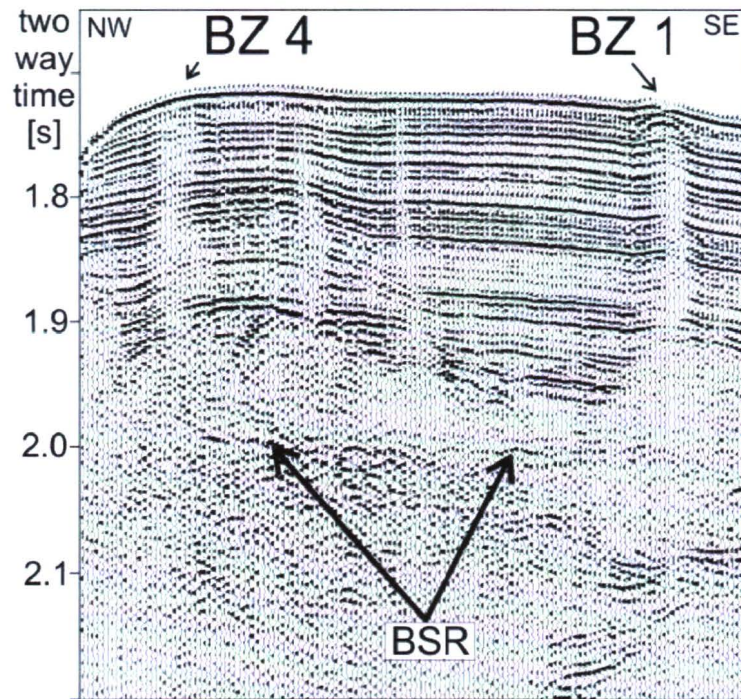


Figure 1.15. Teledyne airgun line showing four blank zones (blank zones 1 and 4 were the focus of this study). The location of the line is shown in figure 2.1 (equivalent to inline 27) (after Riedel, 2001).

1.4. GENERAL DESCRIPTION OF THE STUDY

1.4.1. Introduction to Physical Properties

Physical properties of marine sediments can provide information about their composition, provenance, depositional and formational history, as well as any alterations thereafter. Core sample physical property measurements have become standard all over the world and have been implemented consistently by the Ocean Drilling Project (ODP). Moreover, a detailed knowledge of the physical properties of the near-seafloor sediments can help to infer and quantify: 1) current and past geologic processes including formation and dissociation of gas hydrates, 2) unique seafloor morphology and biology, and 3) detailed engineering properties for assessments of seafloor stability. However, during coring by the large drill rig used by the ODP, the top 10 m of the sediment is often not recovered or is greatly disturbed. Thus, ODP sites frequently lack significant information on the shallowest sediments at the ocean floor. Shallow-penetration piston cores, such as the ones analyzed in this study, can fill this gap in information.

The physical properties measured in this study were: thermal conductivity, magnetic susceptibility, density/porosity, velocity, electrical resistivity, and shear strength. These properties are important because they are dependent on different aspects of the sediment composition and structure, and can be used independently or in combination to describe the nature of the sediment. For example, measuring density changes with depth within the sediment can provide constraints on the differences in porosity and mineralogy. Furthermore, combining density with velocity allows one to calculate the reflection coefficient (RC) of sediment layers which can be used to calibrate remote seismic reflection surveys.

Very little is known about the physical nature of the shallow sediments in the area of gas hydrate deposits. Most of the gas hydrate studies so far have concentrated on the nature and appearance of a BSR (e.g. Hyndman and Spence, 1992), biotic communities supported in these environments (e.g. Lewis and Cochrane, 1990), and chemistry of the circulating fluids and gasses within the sediments (e.g. Paull *et al.*, 2000). However, in order to completely understand these special settings, close attention also needs to be paid to the shallowest sediments, which are often overlooked during large scale research.

1.4.2. Objectives, Significance, and Contributions

The main objectives of this thesis study were to document the physical, chemical, and mineralogical character of sediments within the region of a vent field in order to: 1) provide ground-truth calibrations for seismic impedance and electrical resistivity remote surveys, and 2) examine the effect of high methane fluxes on these sediments. The first objective was undertaken by acquiring high resolution porosity, velocity, and resistivity data which allowed for calculation of the seafloor reflection coefficient, as well as Archie's Law relationship. The second, more comprehensive objective, was studied through careful analyses of various physical and mineralogical properties of the sediments.

Several challenges were met during the data acquisition and analysis process. The correction methods applied and the combination of different measuring techniques developed proved to be reliable and important. Hence, one of the contributions of this thesis was the development of new methodology which can be applied in other physical property studies. However, the major contributions of this research are: 1) the confirmation of the difference in nature of shallow marine sediments with respect to deep sediments; and 2) within zones of high methane flux, the observations of: massive near-surface gas hydrate, low magnetic susceptibility associated with the presence of authigenic pyrite, and high seismic impedance and thermal conductivity associated with the presence of authigenic carbonate.

CHAPTER 2

METHODS AND PHYSICAL PROPERTY MEASUREMENT

2.1. DATA ACQUISITION

2.1.1. Coring Cruise 2000 – PGC00-02

In July and August 2000 an extensive coring project was carried out to closely examine the nature of the seismically observed blank zones 1 and 4 (Figures 2.1-2.3) (Spence *et al.*, 2000). The seismic blank zones were found in 1997, during deep-tow multichannel DTAGS and single channel Teledyne surveys in this area (Chapman *et al.*, 2002). The blank zones are generally few hundred meters in diameter and, on seismic sections, are seen to disturb layered slope sediments. However, the actual depth extent of the anomalous region is not known, since a shallow scattering body could obscure all deeper seismic reflections. Because of the existence of the BSR in this area, it was suspected that the different blank zones could be related to the upward fluid and methane flow. To provide us with a better idea of the nature of the blank zones, the coring survey was accompanied by heat flow, reflection seismic profiles, and pore-fluid geochemical analysis.

During the two-week scientific cruise on board the Canadian Coast Guard Vessel J.P. Tully, a total of 26 piston cores were recovered (Figure 2.1). The area covered by cores 2 to 11 and 19 to 22 will be referred to as Blank Zone 1 (Figure 2.2). The area covered by cores 12 to 17 represents Blank Zone 4 (Figure 2.3). Cores 1 and 23 to 26 were recovered from the region outside the vent field and away from seismic blanking, in order to represent the sediments not obviously affected by focused fluid or methane flow. Four of the cores from within Blank Zone 1 contained solid gas hydrate (core locations in Figure 2.2).

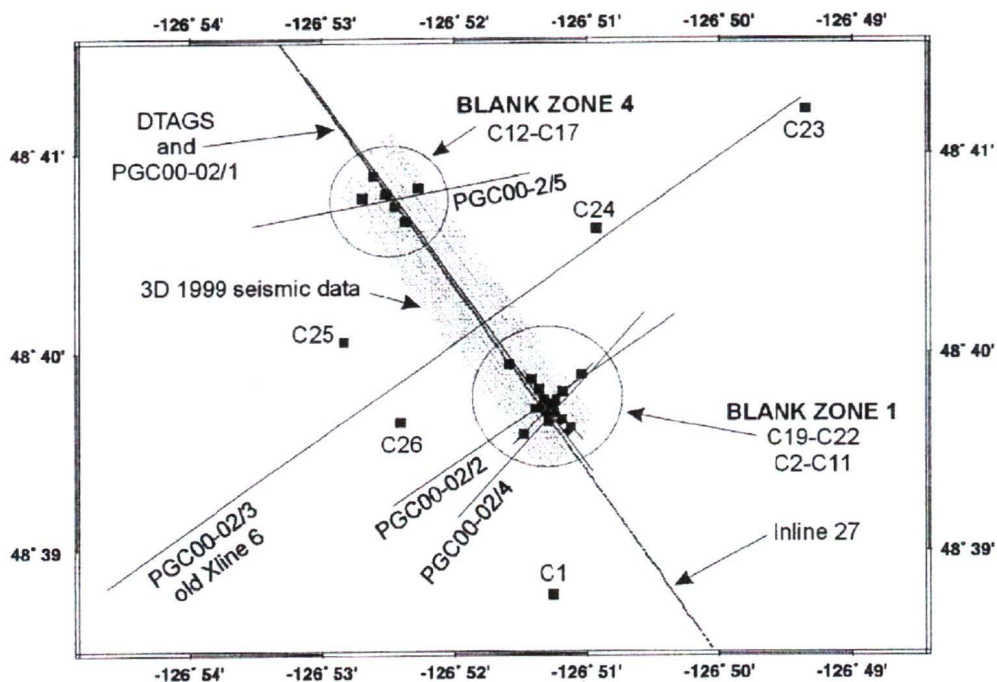


Figure 2.1. The locations of the 26 cores extracted during the PGC00-02 coring cruise. Also shown are the locations of the seismic blank zones 1 and 4 as determined by the previous studies in this area.

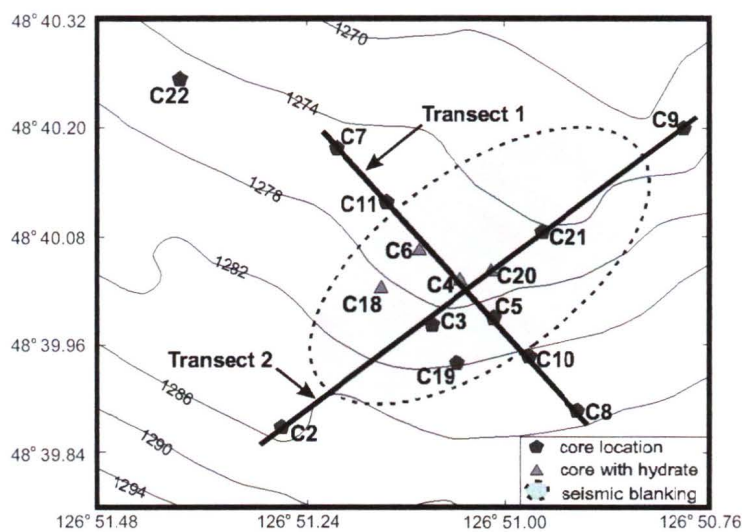


Figure 2.2. The locations of cores in Blank Zone 1, Transect 1, and Transect 2. Also shown is the area of seismic blanking as determined by Riedel (2001).

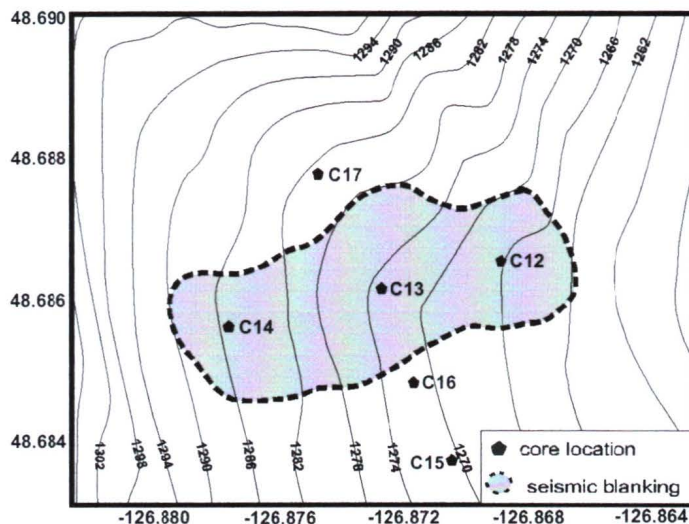


Figure 2.3. The locations of cores in Blank Zone 4. Also shown is the area of seismic blanking as determined by Riedel (2001).

2.1.2. ROPOS Cruises 2000 and 2001

The 2000 coring cruise was closely followed by a cruise with the remotely-operated vehicle ROPOS (Remotely Operated Platform for Ocean Science) in August 2000 (Riedel *et al.*, 2000). The target of this cruise was to visually examine the seafloor environment within the Blank Zone 1 and find visual evidence of gas hydrate existence in this area. In particular, we searched for any indication of special biotic communities known to be indicative of cold vent environments (e.g. tube worms, clams, etc.), and any signs of upward gas migration (e.g. ascending gas bubbles). During the one-week cruise, poor weather conditions were encountered and only a few complete dives were carried out.

Neither sea floor gas hydrate, nor visual gas venting was found. A few isolated biotic communities of clams and tubeworms (Figure 2.4a) were located in this area, but they did not appear to be currently alive; nevertheless, since their shells have not yet dissolved it is expected that they were alive only a few months or a few years ago (Tunnicliffe, pers.comm, 2001). Most of the time, the sea floor appeared barren. Occasionally, sea pens were found scattered on the sea floor with brittle stars and sea

spiders attached to them (Figure 2.4 b,d). At several locations, large outcrops of carbonates were found. Typically, the 10 to 15 cm thick carbonate would cover a large area of the sea floor and would be located around relatively steep ridges that were approximately 3 m high (Figure 2.4 c,f). Sometimes the carbonates were fragmented into 30 to 50 cm pieces. Several of these pieces were collected for further analysis.

A second ROPOS cruise was carried out in May 2001 (Beaudet *et al.*, 2001). During this survey, colonies of live *vesicomyids* clams and *vestmentiferan* *Lamellibrachia barhami* tube worms (Figure 2.4e) were found within Blank Zone 1. Furthermore, large outcrops of sea floor carbonate were found either laying flat on the surface, sometimes covered by a thin layer of fine mud, or as few metre high ridges protruding through the sea floor sediment (Figure 2.4f). During this cruise twelve ½ meter long push cores were recovered using ROPOS and sent for a micropaleontological analysis by L. Kobayashi at McMaster University.

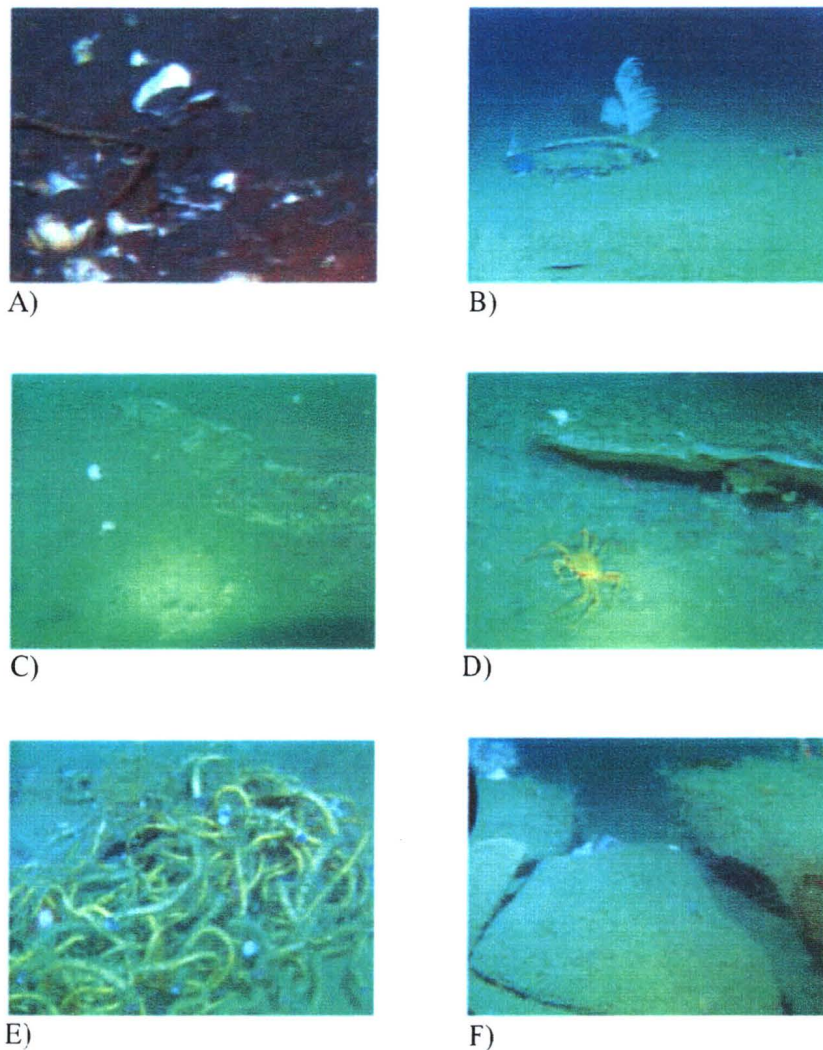


Figure 2.4. Photos of various features of the Blank Zone 1 seafloor environment. Photos were taken using during 2000 (a-d) and 2001 (e-f) using remotely operated vehicle ROPOS. (A) scattered dead clams and tube worms; (B) sea-pen on an otherwise barren seafloor; (C) carbonate seafloor; (D) sea-spider next to carbonate outcrop; (E) living tube worms; (F) large carbonate boulders (~1 m diameter).

2.1.3. Gas Hydrate Recovery

During the PGC00-02 coring cruise, four cores extracted from within Blank Zone 1 contained solid gas hydrate (Figure 2.2). The hydrate was found ranging from 2 to 8 metres below sea floor (Table 1). In cores 4, 6, and 18 the hard hydrate layers halted the core penetration. Within Core 20, a massive hydrate sample about 20 cm thick was recovered. In general, the hydrate specimens appeared as white, gravel-size chunks, with a diameter somewhat smaller than the core liner (i.e. around 5 cm) (Figure 2.5). Silty-clay sediments that surrounded the hydrate were quickly ‘watered-down’ by the hydrate dissociation during recovery. The sediment immediately surrounding and above the hydrate contained disseminated authigenic carbonate granules usually <2 mm in diameter. No other sedimentary differences were observed. Gas hydrate was extracted as quickly as possible from the sediment, visually examined and photographed. Some samples were placed in liquid nitrogen for preservation and subsequent geochemical analysis (Solem *et al.*, 2002).

Several small, centimetre-sized gas hydrate samples were visually observed during dissociation at room temperature. Initially, the dissociation was observed as lively fizzing of gas and water. As the hydrate would “melt”, the gas would escape and the fresh water would be left behind (determined by tasting). As the hydrate samples got smaller (around 1 cm), they would adopt a more disk-like shape. At this time, the fizzing would drastically decrease and the dissociation rate would appear to slow down. The entire dissociation process would last about 1 minute, depending on the size of the initial sample. The samples were also ignited, and they would burn until the sample reached the disk-like shape. Attempts were made to re-ignite several of these smaller samples, but without success.

Table 1. General hydrate description.

Core #	Depth BSF (cm)	Comments
4	804 - 829	Massive hydrate; base of core; halted penetration
6	643 - 733	Hydrate within sediments; carbonate at the base
18	257 - 267	Bottom of core catcher
20	559-585	Hydrate within sediment
20	589-622	Massive hydrate; black clay material at the base



Figure 2.5. Photograph of a hydrate sample. Diameter of the sample was restricted by the diameter of the core liner (i.e. ~5 cm). The length of the sample is approximately 20 cm.

Most of the cores that were located within either of the blank zones, including cores that contained gas hydrate, were highly gas charged and the expulsion of the sediment from the core liners was sometimes difficult to prevent (Figure 2.6). Once the cores were stored in the cold room, the gas expansion decreased until the sediment had stabilized and the gas expansion ceased entirely.



Figure 2.6. Photograph showing the effect of gas expansion on the surrounding sediments. The gas expansion crack is ~10 cm in this case.

2.1.4. Coring Procedure and Core Measurement Preparation

In total, 26 cores were recovered during the PGC00-02 scientific cruise. Cores 2 to 11 and 18 to 22 were located within Blank Zone 1, 12 to 17 were within Blank Zone 4, and the core 1 and cores 23-26 were located away from the blank zones and served as controls (Figure 2.1).

Upon recovery, the total core length usually ranged between 6 and 8 meters. The cores were cut into approximately 1.5 m long sections to ease handling (Appendix A). The top 10 cm of most 1.5-metre sections was cut off and utilized for geochemical analysis by C. Solem from Scripps's Institution of Oceanography, La Jolla. The cores, stored vertically, were allowed to equilibrate to room temperature for several hours before the physical property analysis. The analysis consisted of magnetic susceptibility, thermal conductivity, electrical resistivity, compressional wave velocity, shear strength, and sampling for index property measurements.

The magnetic susceptibility and needle probe thermal conductivity measurements were conducted on whole, unsplit cores, after which the cores were split to allow access for the remaining measurements. One half of the core was designated as a working core and it was photographed before any damage was done to the sediment during sampling. The second half was immediately stored horizontally in a cold room and will serve as an archive core.

The physical property analysis on cores 1 to 18 and 23 was conducted onboard the ship within 1 to 2 days of their recovery. Only the whole-core measurements (i.e. magnetic susceptibility and thermal conductivity) were completed for cores 19 to 22 and 24 to 26 onboard the ship. Following the cruise, approximately 1 to 2 weeks after the core recovery, these cores were taken to University of Washington, Seattle where the measurements of magnetic susceptibility, density, and p-wave velocity were conducted using Multi-Sensor Core Logger. The cores were then transported to the sedimentology laboratory at the Pacific Geoscience Centre in Sidney, British Columbia, where the cores were split, photographed, and sampled for the rest of the physical property measurements (i.e. electrical resistivity, velocity, shear strength, and index properties). Details of each measurement procedure are described in the following section.

Several cores, located inside and outside of the vent, as well as one core located away from the vent sites, were also chosen for sedimentological and micropaleontological analysis. With the assistance and supervision of Dr. T. S. Hamilton, the cores were described in detail and whole section scrape samples were taken and described under a microscope including sand fractions >45 microns. Samples were taken at about 50-cm intervals from each of these cores and were sent to McMaster University, Hamilton, to be processed for foraminifera and grain size analysis by L. Kobayashi.

2.2. PHYSICAL PROPERTY MEASUREMENTS

2.2.1. Manual Physical Property Measurements

Magnetic Susceptibility

Magnetic susceptibility is a dimensionless constant that represents the degree to which magnetization is induced in a material by an external field. Ferrous-rich minerals such as magnetite have very high magnetic susceptibility (~0.01 to 1 SI units). The magnetic properties of most sediments and rocks thus depend on the proportion of magnetite present. Most minerals have low magnetic susceptibilities and as a result will not produce large magnetic anomalies.

Magnetic susceptibility measurements were conducted first. With a measurement interval of 5 cm, the measuring procedure took approximately 5 minutes for each core section. The equipment consisted of a 10.5 cm diameter Sapphire Instruments SI2 coil-meter. The magnetic susceptibility meter was calibrated by taking a measurement of an empty coil before and after each section measurement in order to account for any drift.

To minimize the errors due to edge effects, the top and bottom 10 cm of each section were commonly not measured. Obviously erroneous values on the order of several magnitudes of difference appeared for the sediments that were deformed and cracked by gas expansion due to temperature/pressure changes. When the gas cracks were large enough to be visible through the core liner, the measurements were omitted. However, in most cores these cracks were significantly less than 1 cm wide and thus not observable through the core liner. The gas cracks generally occurred in the lower

sections of the core (i.e. below 5 m depth) and thus increased the variability of data only at those depths. The fairly good accuracy of the method was thus compromised by the nature of the sediment inside the core liner and the presence of gas cracks, ultimately increasing the error to approximately 5%.

Thermal Conductivity

Thermal conductivity of the sediments is required to determine heat flow. Thermal conductivity measures how rapidly heat is transported through a medium. The pulsed needle probe transient method used in this study was developed by Lister (1979) and Lewis *et al.* (1993) and provided by T. Lewis (GSC-PGC). The measurements were conducted on whole cores following the magnetic susceptibility measurements. Measurements were conducted several hours after the core recovery to allow sediment temperatures to equilibrate to the room temperature. The measuring equipment consisted of a 2 mm thick and 7 cm long needle probe with 40.3 ohm calibration resistance, a programmable power supply producing 2.6 J of total energy per centimetre length of the probe, a multi-meter that measured the resistance of the thermistor every 0.5 s, and a computer to log and convert the resistance values to temperatures. The system was calibrated only once, for the same needle probe was used throughout the entire time. A clear gelatin substance was used instead of water to calibrate the needle probe in order to prevent water convective mixing and probe movement. The gelatin was assumed to have similar thermal conductivity properties as water. Since the water thermal conductivity is known for a given temperature (Powell *et al.*, 1983), the needle probe resistance was scaled to fit this conductivity value.

Thermal conductivities were measured approximately every 70 cm, providing two measurements for a standard 1.5 m core. A small hole was hand-drilled into the core liner through which the needle probe was immediately inserted. At this point the temperature drift was measured and the heat pulse was applied only if the drift was less than 0.0003 K/s. The decay of temperature with time was measured and displayed on a graph in order to check the quality of the data and to choose the proper time window where the finite heating duration can be represented adequately as a pulse. In this study, the window was commonly between 30 and 100 s after initiation of the heat pulse.

The short term temperature of the probe after the pulse is complex. However, the change in the temperature inside the probe can be described by the following relationship (Lewis *et al.*, 1992):

$$T(t)=Q/(4\pi\kappa t)$$

where Q is the total heat input per unit length of the probe, κ is the thermal conductivity, t is the time since the heat pulse, and T is the temperature in degrees Kelvin. The thermal conductivity is obtained by defining the slope of the temperature decay curve on a T versus 1/t graph.

To ensure good data collection, the needle-probe has to have a full contact with the sediment. This was sometimes difficult to achieve due to ship's unsteadiness and thus created probe movement and an estimated accuracy error of 10%.

Electrical Resistivity

Electrical resistivity was the first measurement done on a split core in order to minimize water evaporation and thus a potential salinity increase. The measurements were taken at a 10 cm interval (Figure 2.7). The measurements were omitted if the sediments were visibly altered during core recovery or due to gas expansion.

The equipment was designed and assembled by D. Heffer, D. Mosher, and T. Hewitt of Geological Survey of Canada (GSC). The measuring device consisted of a 4-pin Wenner electrode array and a digital temperature probe (to minimize the contact resistance). The pins were gold plated and approximately 3 mm in length, separated from each other by 2 mm. The outer 2 pins were connected to a circuit board with AC voltage source through current limiting resistors; by using an AC source, the buildup of chemical potentials at the electrodes is avoided. The inner 2 pins were connected to a Fluke voltmeter. The entire instrument was connected to a PC through an RS-232 output thus allowing all raw data processing and display to be done automatically.

Electrical resistivity can be defined by the following formula:

$$R = \frac{V}{I * C}$$

where V is the voltage, I is the current, and C is a cell constant. The cell constant was calculated before each section measurement from calibration in seawater. Standard

seawater has a known resistivity, R_w , which can be described by the following formula (Hewitt, 1998):

$$R_w = (2.8 + 0.1 * T)^{-1}$$

where T is the temperature in degrees Celsius. Since the temperature, voltage, and current can be measured, the cell constant can be determined. The instrument is thus calibrated by adjusting the cell constant until $R_w=0.209$ ohm-meters for a temperature of 20°C.

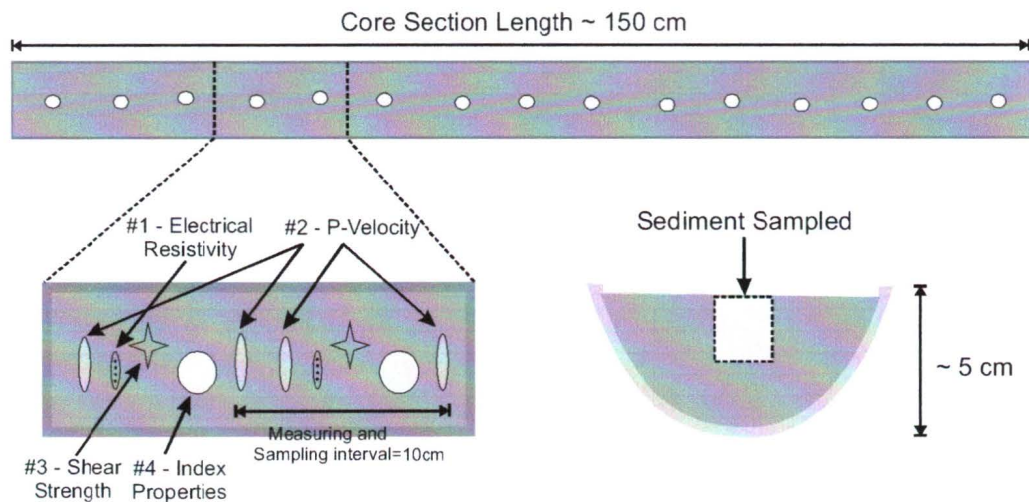


Figure 2.7. A schematic representation of the typical split-core physical properties measurement order and position.

Sample resistivity was then derived using the following formula:

$$R_o = R * (1 + 0.025 * (T - 20))$$

where R is the measured, uncorrected for temperature sample resistivity (Hewitt, 1998)

The data logging and processing program, written by T. Hewitt using computer software LabView, calculated resistivity formation factor using the following relationship:

$$F = \frac{R_o}{R_w}$$

Majority of errors were produced by the inconsistencies in the depth of the pin penetration into the sediment as well as the abundance of gas cracks in lower sections of the cores, thus increasing the error to approximately 5%.

Compressional Velocity

Compressional or p-wave velocity measuring equipment consisted of 2 ultrasonic transducers, a transmitter and a receiver, attached to a base plate. The transducers were 7 cm apart. Before each section measurement the system was calibrated by measuring the traveltime between the transducers for water, t_{water} , at a known temperature and velocity, and thus checking the distance between the transducers. The transducers were aligned to measure the velocity along the length of the core (Figure 2.7). The interval between velocity measurements was 10 cm and the reference depth along the length of the core for the measurement was taken to be in the middle of the 2 transducers. The traveltime, t_{sample} , was determined by visually locating the displayed arrival time curve of the first non-zero voltage (the first break was consistently chosen as the point on the curve where the voltage starts to be non-zero, ± 5 m/s). The velocity is calculated using the following formula:

$$V_{p_{\text{sample}}} = \frac{t_{\text{water}}}{t_{\text{sample}}} * V_{p_{\text{water}}}$$

where $V_{p_{\text{sample}}}$ and $V_{p_{\text{water}}}$ are the compressional velocities of a sample and water respectively.

As with magnetic susceptibility and resistivity measurements, sediment cracking due to gas expansion resulted in the partial or complete attenuation of the acoustic signal so that no p-velocity measurements could be made in many cores below ~4 m depth. This however, as well as being able to visually examine the nature and the quality of the p-wave, ensured that the error was likely less than 5%.

Shear Strength

The shear strength equipment consisted of the Wykeham-Farrance motorized shear vane (Hewitt, 1998). A torque caused by the sediment strength is displayed as a

function of angular rotation through the use of calibrated spring vane as the torque sensor. The sediment throughout the cores was of relatively similar strength and the same spring and vane were kept throughout all measurements. The shear vane was inserted into the sediment, often next to where the resistivity measurement took place (Figure 2.7). The motor was then turned on and the vane started to rotate. The point at which the sediment sheared or failed, was recorded on a computer. Shear strength (S), measured in N/m^2 or Pa, can be described by:

$$S = \tau\gamma/K$$

where τ is the spring constant (0.00186 Nm/deg), γ is the degrees of stress rotation, and K is the vane constant ($3.25 \times 10^{-7} \text{ m}^{-3}$) (Hewitt, 1998).

Once more the sediment cracking influenced the measurement by lowering the shear strength of the sample and when evident, these measurements were omitted. Also, sometimes the point of failure was gradational and determining the actual value of the shear was difficult and somewhat interpretative, leading to an estimated error of approximately 5%.

Bulk Density, Porosity, and Grain Density

The volume samples for the density/porosity analysis were taken at two different time intervals using three different volume samplers or plugs. The two smaller plugs (6.60 cm^3 and 6.65 cm^3) were used immediately after core recovery onboard the ship for cores 1 to 18 and core 23. Cores 19 to 22 and 24 to 26 were sampled in the laboratory at the GSC Pacific Division approximately 2 weeks later using the larger plug (10.04 cm^3) in conjunction with one of the smaller plugs (6.65 cm^3). Sediment compaction and/or extrusion from the plug were commonly observed during sediment sampling using the two smaller plugs. After estimating the length of the unfilled portion of the smaller plugs, a correction was made for the missing sediment (see Data Correction section).

The samples were placed in glass vials and stored in a refrigerator in order to minimize sediment moisture loss. The mass of wet sediment was measured approximately 3 weeks after the recovery. The samples were then dried at 95°C for a period of 24 hours in a Fisher IsoTEMP Oven 338 and their mass was measured again.

The formulae for bulk density, porosity, and grain density were derived and modified using the standard and the ODP laboratory procedure formulae (Westbrook *et al.*, 1994) as follows:

Bulk Density:

$$\rho_{bulk} = \frac{M_{wet_sample}}{V_{sample}}$$

Water Content:

$$M_{fresh_water} = M_{wet_sample} - M_{dry_sample}$$

Porosity:

$$\Phi = \frac{V_{pore_space}}{V_{sample}} = \frac{V_{pore_fluid}}{V_{sample}} = \frac{M_{pore_fluid}}{V_{sample} * \rho_{pore_fluid}} = \frac{M_{fresh_water} + M_{salt}}{V_{sample} * \rho_{pore_fluid}}$$

where V_{pore_space} = volume of pore space, V_{sample} = volume of sediment sampler, V_{pore_fluid} = volume of pore fluid, M_{pore_fluid} = mass of pore fluid, ρ_{pore_fluid} = assumed density of pore fluid (1.024 g/cm³), M_{wet_sample} = mass of wet sediment, M_{dry_sample} = mass of dry sediment, M_{salt} = mass of salt within the pore fluid.

Because the mass of salt within the sediment and pore fluids is unknown and difficult to estimate directly, one can assume the value of salinity for the pore fluid and calculate the mass of the pore fluid from the measured mass of fresh water by using the salinity correction as follows:

$$\Phi = \frac{M_{wet_sample} - M_{dry_sample}}{V_{sample} * \rho_{pore_fluid} * (1 - \sigma)}$$

where σ = assumed salinity of pore fluid (0.035).

Grain Density:

The above formula can then be used to calculate the mass and volume of salt within the sediment and pore fluid:

$$M_{salt} = M_{pore_fluid} - M_{fresh_water} = \Phi * V_{sample} * \rho_{pore_fluid} - M_{fresh_water}$$

$$V_{salt} = \frac{M_{salt}}{\rho_{salt}}$$

Grain density is thus:

$$\rho_{\text{grain}} = \frac{M_{\text{dry_sediment}}}{V_{\text{dry_sediment}}} = \frac{M_{\text{dry_sample}} - M_{\text{salt}}}{V_{\text{dry_sample}} - V_{\text{salt}}}$$

where, ρ_{salt} = density of salt (2.257 g/cm³), ρ_{grain} = grain density, $M_{\text{dry_sediment}}$ = mass of dry sediment without salt content, $V_{\text{dry_sediment}}$ = volume of dry sediment without salt content.

2.2.2. Multi-Sensor Core Logger (MSCL)

Approximately 1 to 2 weeks after core recovery, cores 18-22 and 24-26 were analyzed using Geotek Multi-Sensor Core Log (MSCL) 5.2 in the Marine Sciences laboratory at University of Washington, Seattle. All the measurements were conducted on the unsplit cores with a 1 cm sampling interval. The measurements consisted of p-wave velocity, magnetic susceptibility, and Gamma Ray attenuation (bulk density). The MSCL conveyor system would push each core section pass the sensors. All the measurements are conducted at exactly the same section depth, and are automatically correlated. P-wave measurements were conducted using piezo-electric ceramic transducers. Gamma ray attenuation was measured using a 137-Cs gamma source, and automatically converted to bulk density. Magnetic susceptibility was measured using a Bartington loop sensor. The results of MSCL measurements were used as a direct comparison with the manual physical property measurements described above.

2.3. DATA CORRECTION

2.3.1. Density/Porosity Corrections for Missing Sediment Volume

The sediment samples for the density/porosity analysis were extracted using two small plugs (approximately 6.6 cm³) and one large plug (approximately 10.0 cm³). The smaller width and higher friction of the smaller two plugs resulted in partly filled sampling plugs. For this reason the sediment volume sampled had to be estimated. During sampling, the length of the unfilled portion of the plug was noted in millimetres. This measurement was then used to estimate the missing sediment volume and mass.

The height of the unfilled portion of the smaller plugs varied from zero to 10 mm, with an average value of 2.1 mm. Because the total height of the plugs was 30 mm, plugs with unfilled sections of over 5 mm were not measured. This lowered the average height of unfilled plugs to 1.8 mm, i.e., 6% of the total height.

Several factors had to be assumed. First, the correction is only adequate if the sediment was missing due to sediment extrusion only. The effects of sediment compaction were not taken into consideration. Second, in order to calculate the mass of the missing wet and dry sediment, sediment porosity and bulk density had to be estimated. The correction method consisted of using iterative calculations of porosity and bulk density. Initially, the mass of missing wet and dry sediment was estimated using the initial, uncorrected values. This allowed for new values of density and porosity to be calculated, which were then used again to calculate missing wet and dry sediment mass. The iteration was conducted one hundred times.

Several samples were randomly chosen in order to illustrate the effect of the correction on bulk density, fractional porosity, and grain density for different amounts of missing sediment. The results of one of these samples are illustrated in Table 2. The magnitude of correction is lowest for bulk density and highest for grain density, so that grain density has the greatest sensitivity to errors in estimating the missing sediment.

Table 2. Percent change in values due to correction for core 21, sample 1908.

Empty Vial Height (mm)	Calc. Bulk Density (g/cm ³)	% Difference From Original	Calc. Fractional Porosity	% Difference From Original	Calc. Grain Density (g/cm ³)	% Difference From Original
0	1.49	0	0.60	0	2.12	0
1	1.54	3	0.63	5	2.33	10
2	1.60	7	0.67	12	2.63	24
3	1.65	11	0.71	20	3.06	45
4	1.72	15	0.77	29	3.79	79
5	1.78	20	0.84	42	5.34	152

Table 3 shows the same calculation for the average value of 2 mm for the unfilled portion of the plug. An underestimate of the height by 1 mm would imply an underestimate in bulk density by 4% or 0.06 g/cm^3 , porosity by 6% or 0.04, and grain density by 11% or 0.3 g/cm^3 . An overestimate of the height by 1 mm would imply an overestimate in bulk density by 4% or 0.06 g/cm^3 , porosity by 7% or 0.08, and grain density by 17% or 0.74 g/cm^3 .

Figure 2.8 shows data sets for core 21 for both smaller and larger plugs, before and after the correction to the smaller-plug data was applied. It is assumed that data collected with the larger plug is more correct and thus the correction should reduce the difference between the two data sets. The increase in the trendline similarity between the two data sets is taken as an indicator of correction. It is evident that after the correction was applied, the data sets were less spread out and followed the same trend more closely.

Figure 2.9 shows the result of correction with two data sets combined after the correction to the smaller-plug data was applied. The root-mean-square of the deviations (Drms) shows the improvement contributed by the correction. For example for core 21, the Drms value for bulk density decreased from 0.10 to 0.07, for fractional porosity from 0.06 to 0.05, and for grain density from 0.29 to 0.17. Moreover, with the uncorrected data, a best fit line to the combined data sets shows a trend of decreasing bulk density with increasing depth (Figure 2.9a). This is contrary to the normally expected trend in which density increases with depth due to compaction. After the correction, bulk density increases with depth (Figure 2.9d). Similarly, grain density is expected to be nearly constant with depth but the uncorrected data shows a decrease with depth (Figure 2.9c). After the correction, as anticipated, the data are less dispersed and grain density has a nearly constant value of 2.5 g/cm^3 (Figure 2.9f).

Table 3. The effect of an under- and over-estimate in the height of the unfilled plug. A sample with an average value for the unfilled portion of the plug is used.

Missing Sediment (mm)		Calc. Bulk Density (g/cm³)	% Change From Original	Calc. Fractional Porosity	% Change From Original	Calc. Grain Density (g/cm³)	% Change From Original
Average Value	2	1.60	-	0.67	-	2.64	-
Under-estimate	1	1.54	-4	0.63	-6	2.34	-11
Over-estimate	3	1.66	4	0.71	7	3.08	17

Figure 2.10 shows the result of the same iterative correction procedure on core 2, which was sampled using only the two smaller plugs. The most striking difference is the change in the position of the y-intercept value for the bulk density, fractional porosity, and grain density. In the original data set, all values are significantly lower than expected based on ODP Leg 146 and the larger plug results. After the correction, bulk density at the surface increases from 1.42 to 1.53 g/cm³, fractional porosity increases from 0.58 to 0.67, and grain density increases from 1.9 to 2.5 g/cm³ (Figure 2.10). Moreover, Figure 2.11 shows that after the correction was applied to core 2, fractional porosities are in much better agreement with the results from core 21.

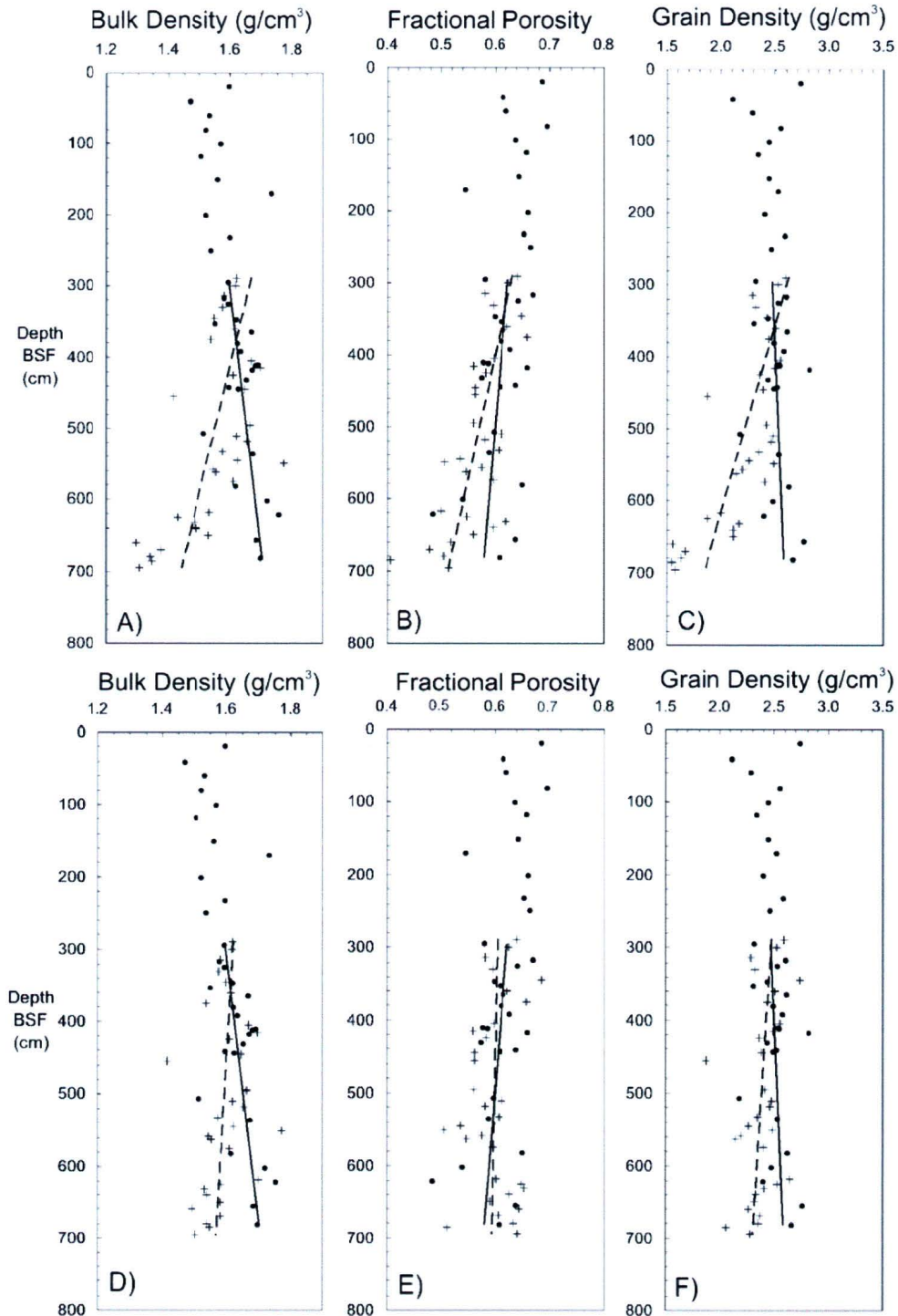


Figure 2.8. Core 21 index properties. Data collected using the smaller plug are represented by crosses and data collected using the larger plug are represented by filled circles. Solid and dashed lines represent linear trendlines for larger and smaller plugs. (a,b,c) Original, uncorrected values for bulk density, porosity, and grain density for both data sets. (d, e, f) Values for both sets after the smaller plug data was corrected using iterative correction method for unfilled plugs.

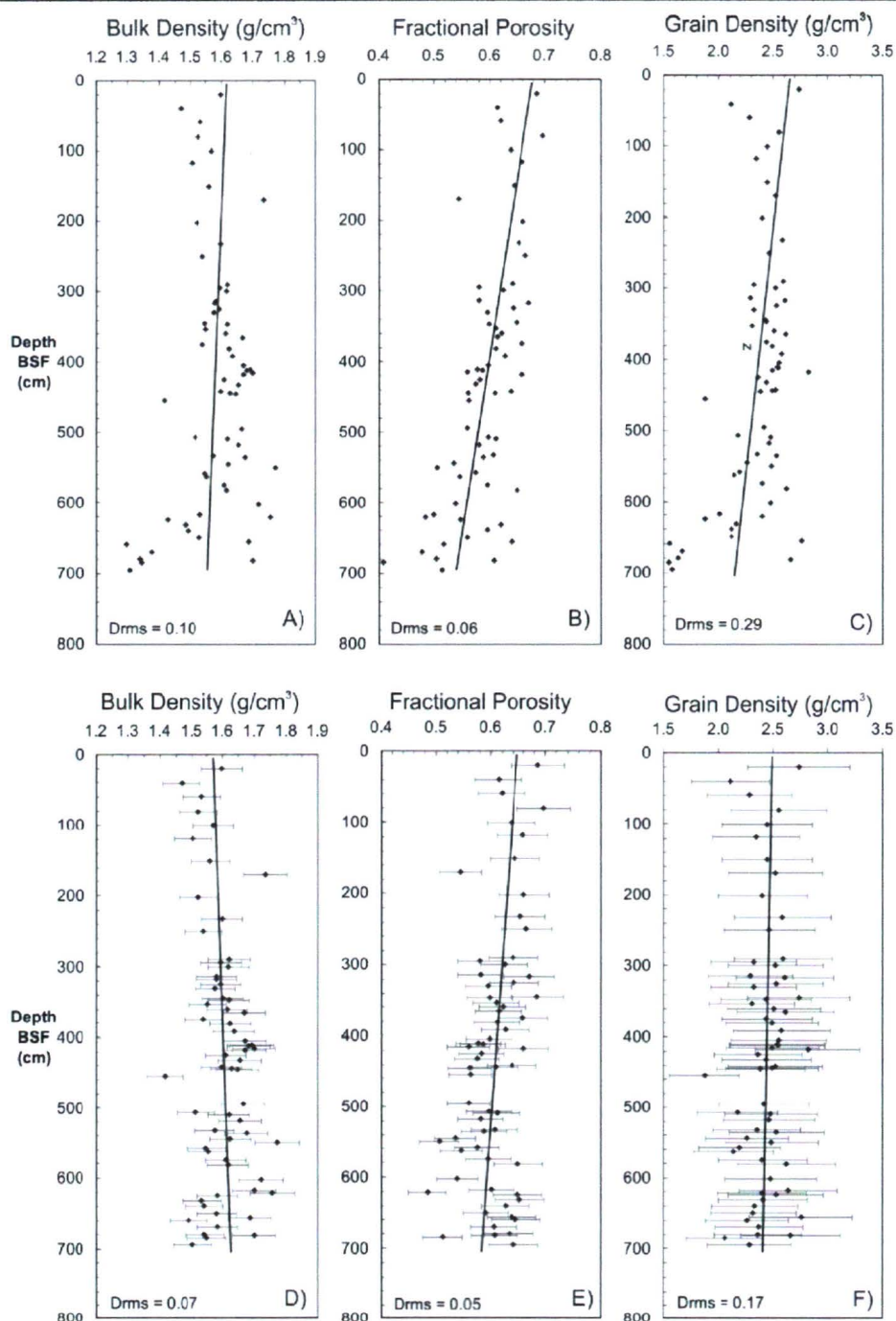


Figure 2.9. Core 21 index properties. The solid line represents linear trendline with the root-mean-square deviations (Drms) shown in the bottom left corner of each diagram. (a,b,c) Original, uncorrected values for bulk density, porosity, and grain density. (d,e,f) Same data sets after iterative correction method for unfilled plugs was applied. The error bars were calculated assuming ± 1 mm error in the missing sediment height (4% error for bulk density, 7% for fractional porosity, and 17% for grain density).

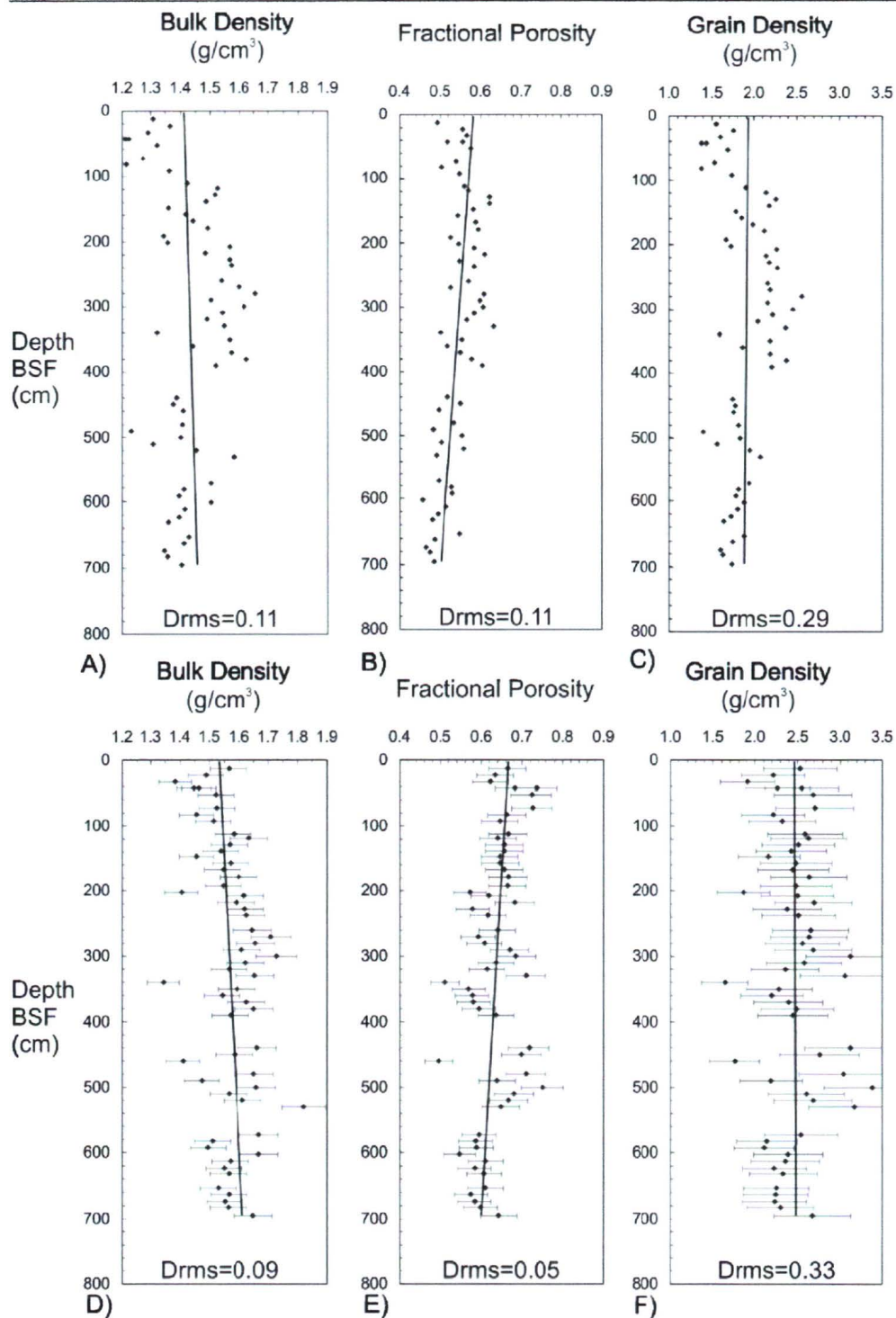


Figure 2.10. Core 2 index properties. The solid lines represent linear trendlines with the root-mean-square deviations (Drms) shown in the bottom left corner of each diagram. (a,b,c) Original, uncorrected values for bulk density, porosity, and grain density. (d,e,f) The correction using iterative method for unfilled plugs. The error bars were calculated assuming ± 1 mm error in the missing sediment height (4% error for bulk density, 7% for fractional porosity, and 17% for grain density).

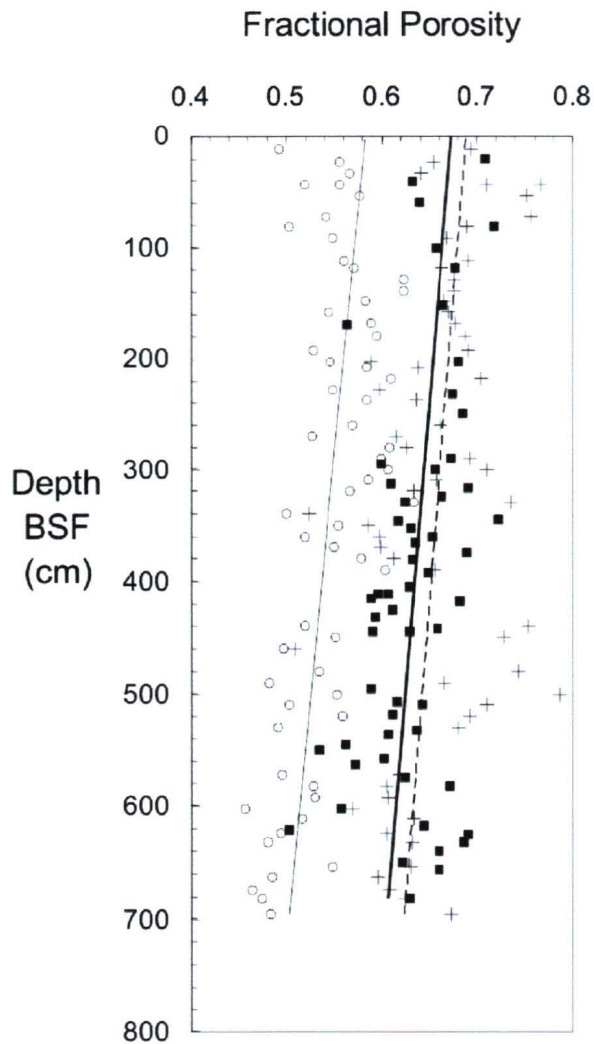


Figure 2.11. Fractional porosity for core 21 and core 2. Corrected data for unfilled plugs using iterative method for core 21 and their best-fit line are represented by filled squares and a thick line. Original data for core 2 and their best-fit line are represented by unfilled circles and a thin line. Corrected data for unfilled plugs using iterative method for core 2 and their best-fit line are represented by pluses and a dashed line.

Scaling to Known Grain Density

At ODP Leg 146 Site 889, located less than 5 km from the study area, grain densities of the surface sediments ranged between 2.6 and 2.7 g/cm³. Assuming that the two environments are similar, the grain density values indirectly measured during PGC00-02 cruise needed to be increased by approximately 0.2 g/cm³. Although the

agreement between the two data sets is within the expected error, even for an uncertainty of ± 0.5 mm in the length of the unfilled portion of the plug (Table 2), it was decided that average scaling to the ODP grain density value of 2.65 g/cm^3 should be applied to all cores. This implied that the values for the missing sediments in the plugs were on average underestimated by approximately 0.5 mm. The correction was executed by calculating an average grain density value for each core. The amount of sediment missing was then increased until the average value of the grain density for that core equaled 2.65 g/cm^3 . The values for bulk density and fractional porosity were automatically corrected to agree with the new grain density values. By doing this, the characteristic variations within the core were left unchanged and the final results agreed with the ODP Leg 146 results (Figure 2.12).

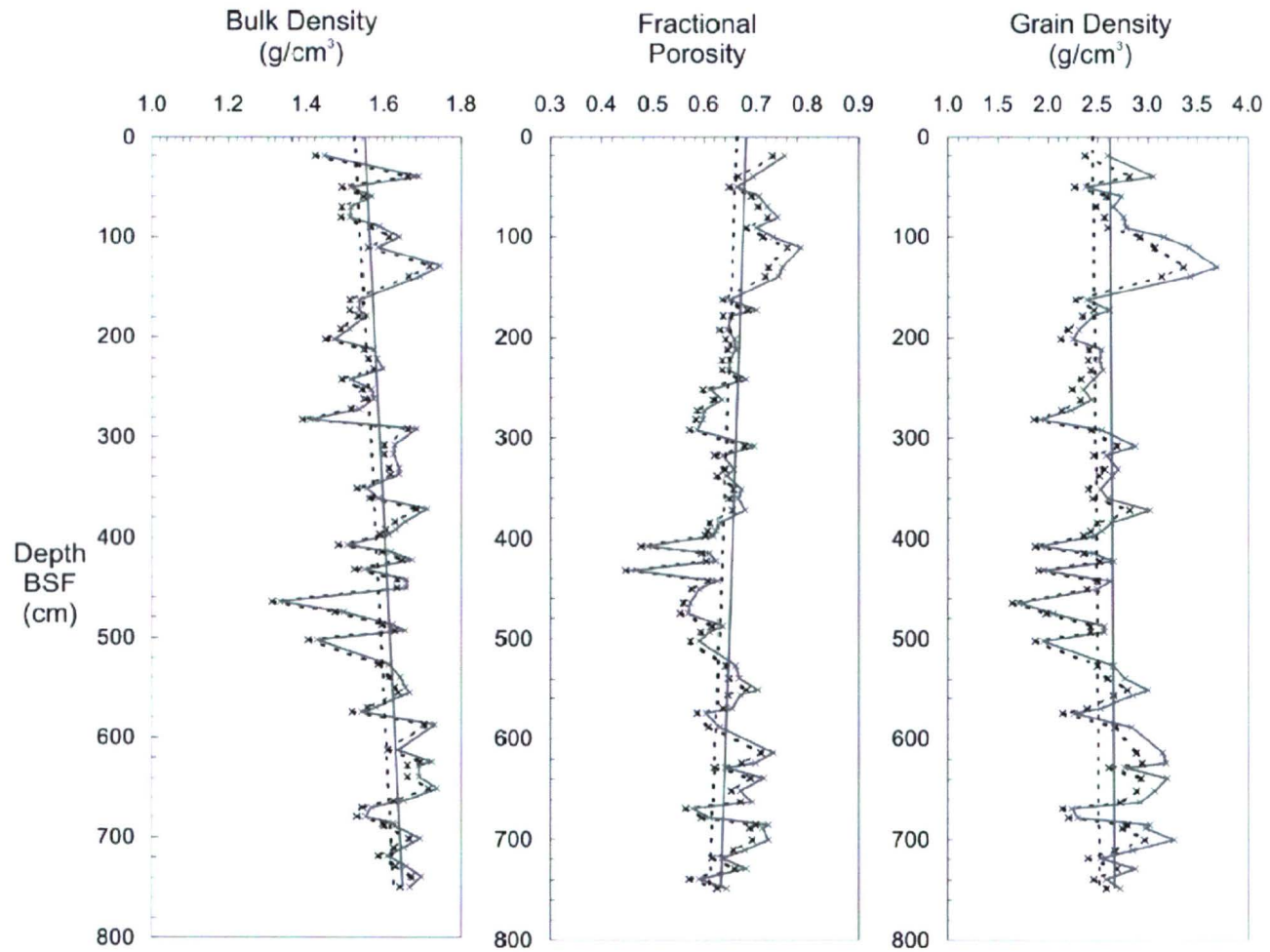


Figure 2.12. Core 9 index properties. The dashed line represents data for which the small sample plug were corrected for missing sediment using iterative method, whereas the solid line shows the same data set after the grain density has been scaled to fit ODP Leg 146 average grain density value of 2.65 g/cm³.

2.3.2. Multi-Sensor Core Log (MSCL) Fractional Porosity Data Correction

Cores 18-22 and 24-26 were analyzed using Geotek Multi-Sensor Core Log (MSCL) 5.2 at University of Washington, Seattle. Among other properties, bulk density of the cores was measured using the Gamma Ray Attenuation method. Each core had been previously cut into approximately 1.5 m sections, and all sections were analyzed over a 3-day period, but not in any particular order. The data sets for each core were subsequently combined.

Values of fractional porosity were exceedingly high in comparison to what is expected based on the fractional porosity data measured using sampling plugs and ODP Leg 146 porosity data (Figure 2.13). Also, this difference was not consistent between different sections of the core. The origin of this significant discrepancy is not well understood, although some of the difference may be attributed to varying ambient and core temperatures during measurements.

The corrected plug-data were used to calibrate the MSCL data. The MSCL fractional porosity data were corrected by lowering each section by some consistent amount (0.2 in average) until its trendline overlapped with the trendline of the corrected plug-data (i.e. until the mean value for a MSCL section matched the mean value for the corresponding set of plug-data values). With few exceptions, the plug-data points matched well with the much more rapidly varying MSCL data set. It was thus concluded that the MSCL data could be used for analysis of shorter spatial scale anomalies, whereas the corrected plug-data provided information on the more general trends.

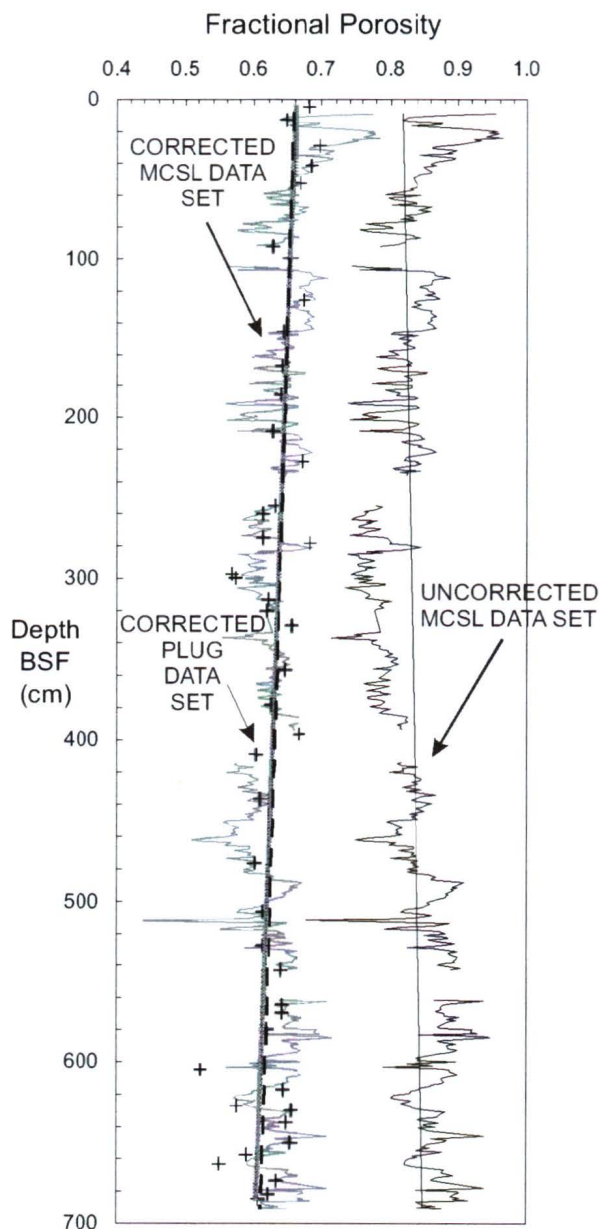


Figure 2.13. Multi-Sensor Core Log (MSCL) fractional porosity data for core 19. The original, uncorrected data set and the best-fit line are represented by thin solid lines (1cm sampling interval). The corrected MSCL data set and the best-fit line are represented by thick, solid lines. The pluses and the dashed line represent corrected plug-data set and its best-fit line.

CHAPTER 3

OBSERVATIONS

Within this chapter, general observations will be brought to readers attention. A complete set of results is included on the CD-ROM supplement that is included with this thesis.

3.1. PHYSICAL PROPERTIES

Most of the core thermal conductivity data fall in the narrow range between 1 and 1.1 W/mK for all three areas, with a mean of 1.04 ± 0.08 . The hydrate cores within Blank Zone 1 were plotted as filled triangles and appear to have slightly higher thermal conductivities, mostly ranging from 1.1 to 1.2 W/mK (Figure 3.1).

The magnetic susceptibility values ranged from 0 to 8000×10^{-6} SI. The cores located within the Blank Zone 1 and 4 had susceptibility values up to 4000×10^{-6} SI (Figure 3.1a and b). Only the cores outside the vent area had greater values (Figure 3.1c). Also, the cores located within the actual extent of seismic blanking generally had significantly lower magnetic susceptibility values than the cores located outside this area. For example, the cores represented by triangles in Figure 3.1 (a) are the cores located within the area of seismic blanking and have lower values of magnetic susceptibility around 500×10^{-6} SI. The cores represented by crosses are located just outside the seismic blanking, but still within the vent site, and have susceptibility values around 3000×10^{-6} SI.

No evident spatial pattern was observed in electrical resistivity and p-velocity measurements. Electrical resistivity values varied generally between 0.4 and 0.7 Ohm-m (Figure 3.1). The cores located outside the vent area had a slightly higher upper range (i.e. 0.9 Ohm-m). In general, there was a well defined but small linear increase with depth in resistivity for all cores. P-velocity had a similar increasing trend. P-velocity values for cores within Blank Zone 1 and outside of the vent area ranged from 1470 to 1530 m/s with a mean and standard deviation of 1502 and 20 m/s, respectively. The values for Blank Zone 4 showed slightly less variation, ranging from 1500 to 1530 m/s with a mean 1526 ± 15 m/s. Due to the common presence of gas expansion cracks in the lower portion of most cores, velocity measurements were mainly restricted to the upper 5

m of the core, except for some of the cores located just outside the seismic blanking area within Blank Zone 1 and 4 (Figure 3.1a and b).

Shear strength measurements were better constrained within the upper 4 m of the cores (Figure 3.1). The values for cores within the blank zones generally ranged between 10 and 80 kPa with a mean and standard deviation of 46 and 17 kPa, respectively. The cores located outside of the vent area had slightly higher values that ranged between 20 and 150 kPa with a mean and standard deviation of 65 and 33 kPa, respectively. For all cores, shear strength generally increases with depth. Particularly for the two blank zones (Figure 3.1a and b), the values increase rapidly within the top 4 m of the sediment from 10 to 70 kPa. Below 4 m, shear strength is nearly uniform, with values ranging between 70 and 80 kPa. For cores located outside the vent area, shear strength continues to increase with depth below 4 m, although the values are highly scattered.

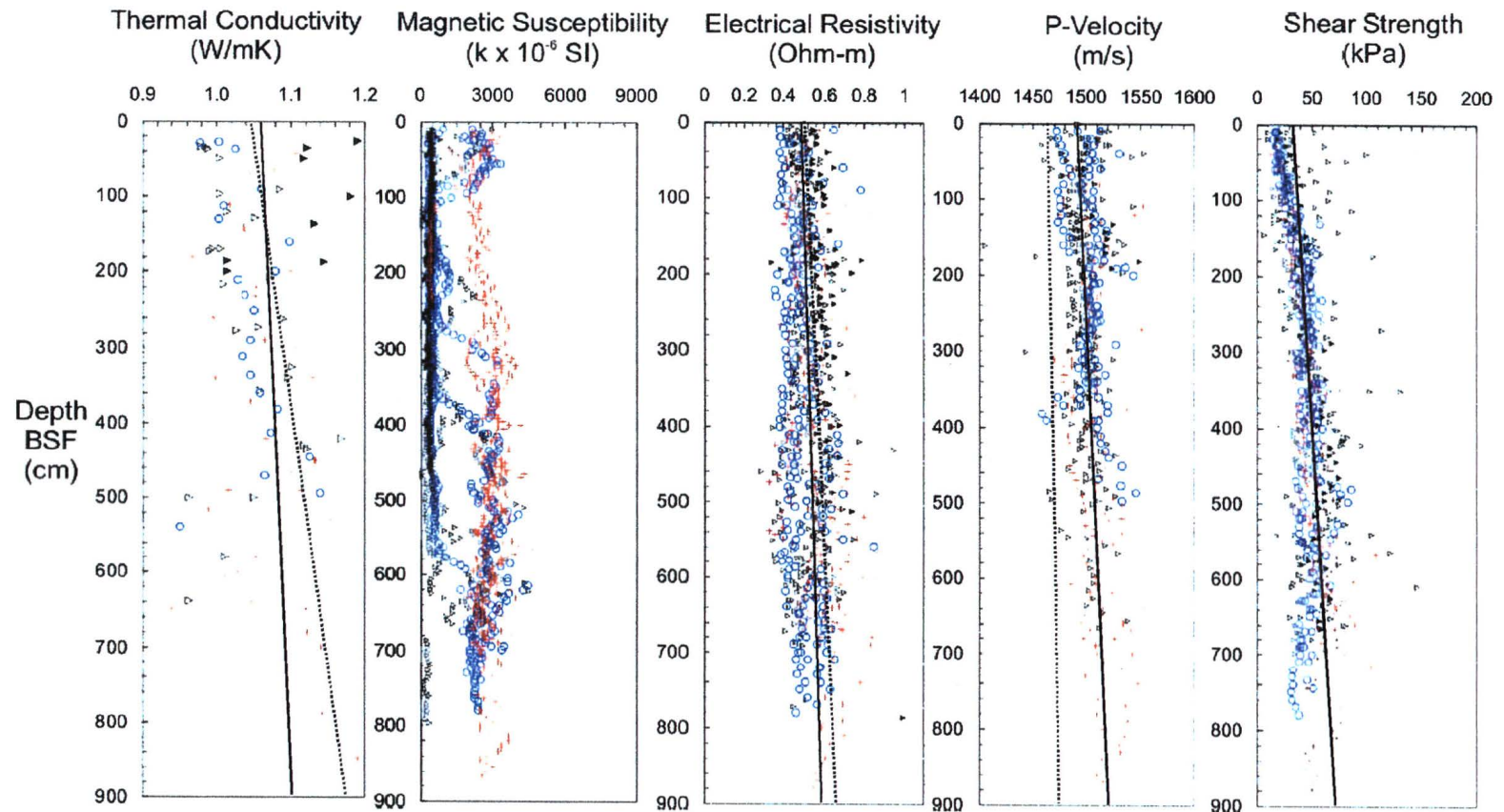


Figure 3.1 a) Thermal conductivity, magnetic susceptibility, electrical resistivity, P-velocity, shear strength, and their trends (solid lines) for cores at Blank Zone 1. Triangles represent cores located within the seismic blanking zone (C3-6, C18-21), filled triangles represent cores that contained hydrate, circles represent cores located near the boundary of seismic blanking (C9-10), and pluses represent cores located outside the blanking zone (C2, C7-8, C22). Dotted lines represent ODP Leg 146 trends for measurements down to 10 m BSF.

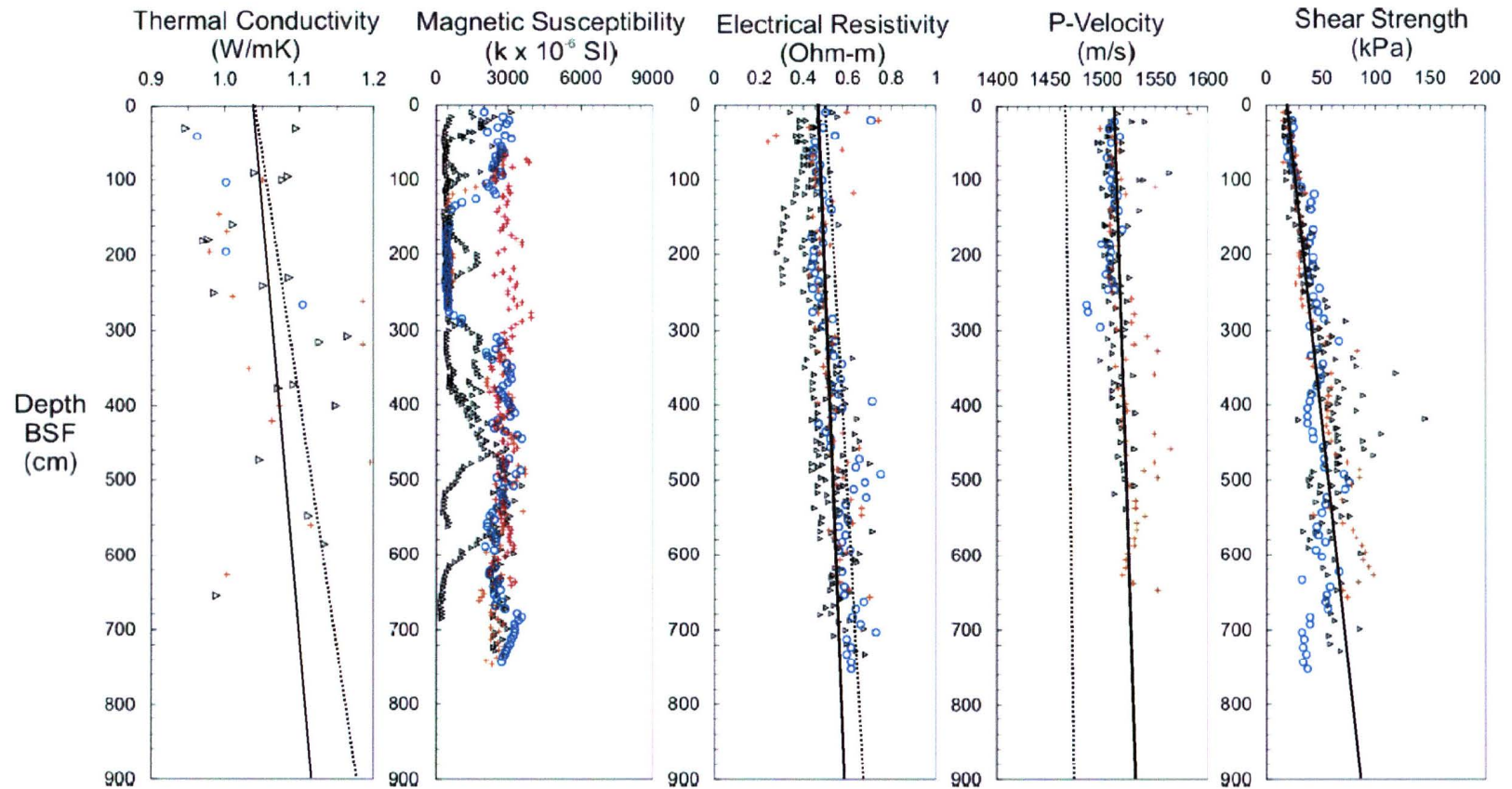


Figure 3.1. b) Thermal conductivity, magnetic susceptibility, electrical resistivity, P-velocity, shear strength, and their trends (solid lines) for cores at Blank Zone 4. Triangles represent cores located within the seismic blanking zone (C12-14), circles represent cores located near the boundary of seismic blanking (C16), and pluses represent cores located outside the blanking zone (C15 and C17). Dotted lines indicate ODP Leg 146 trends for measurements down to 10 m BSF.

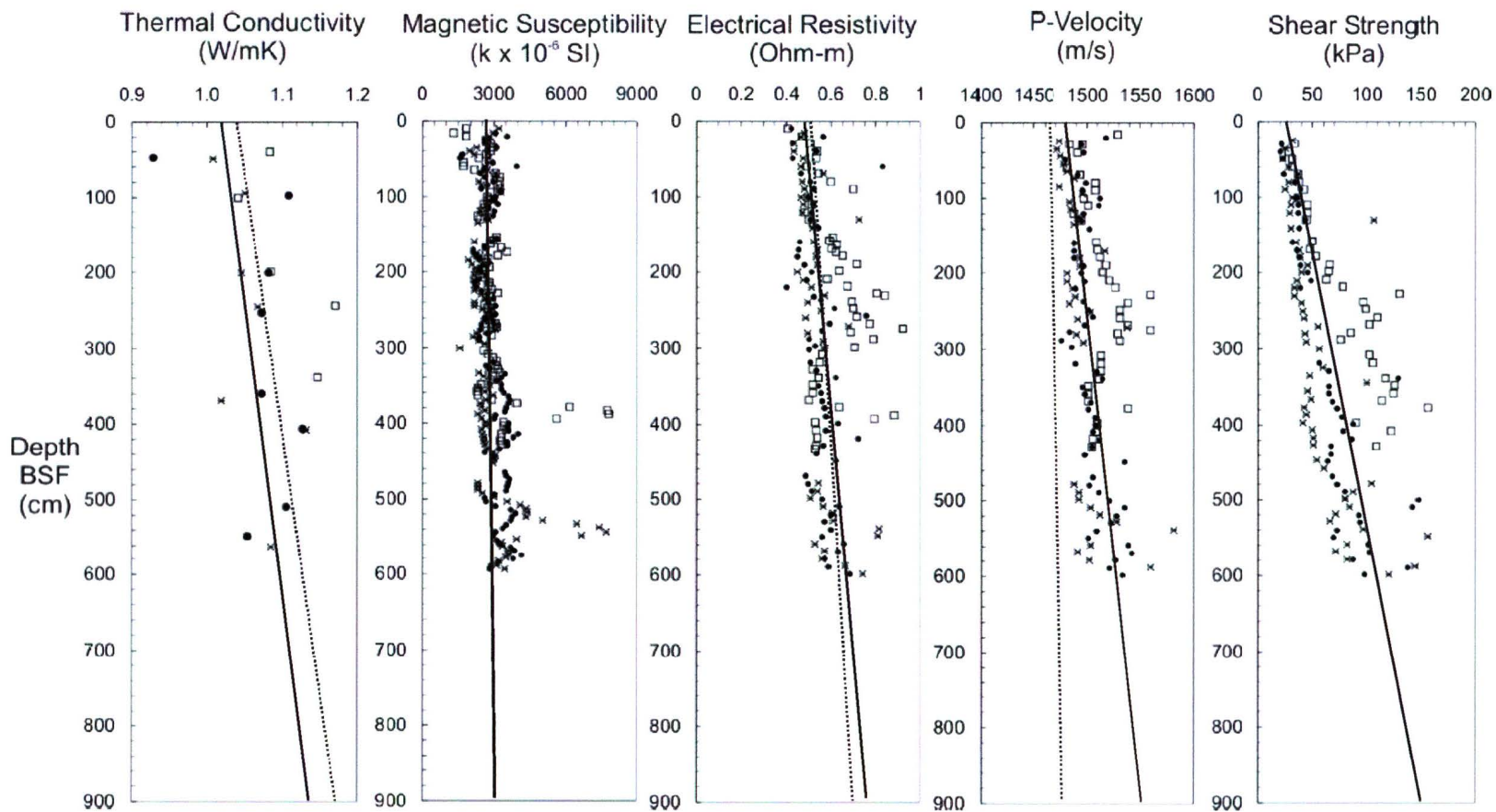


Figure 3.1. c) Thermal conductivity, magnetic susceptibility, electrical resistivity, P-velocity, and shear strength for cores located outside the vent area. Data for core 24 is represented by stars, for core 25 by filled circles, and for core 26 by open rectangles. Dotted lines indicated ODP Leg 146 trends for measurements down to 10 m BSF.

3.2. INDEX PROPERTIES

The entire suite of cores was sampled for density measurements using the plug method (see Methods section). Cores that were examined onboard the ship were sampled using smaller plugs, whereas the cores analyzed on land were sampled using a combination of smaller and larger plugs. The larger plugs were used in order to help with data correction for missing volume of the sediment within the smaller plugs (see Data Correction section).

The index property values showed a large amount of scatter (Figure 3.2), although the scatter was reduced by corrections for missing sediment volume from the smaller plugs. Grain density ranged from 2 to 3.5 g/cm³ with an average of 2.6 ± 0.3 , fractional porosity ranged between 0.5 and 0.8 with an average of 0.65 ± 0.05 , and bulk density ranged from 1.4 to 1.9 g/cm³ with an average of 1.6 ± 0.1 . However, general trends in properties were easily observed. For example, within Blank Zone 1, grain density and bulk density increased at rates of 2×10^{-4} and 1×10^{-4} g/cm³, respectively, whereas fractional porosity decreased 7×10^{-5} g/cm³, with depth in centimetres (Figure 3.2). More scatter was observed in upper and lower sections of the core than in the middle. This portion of the scatter is attributed to the overall nature of the sediment (i.e. the top most sediments were of 'soupy' consistency and their sampling was often made difficult, whereas the bottom most sediments were affected by the presence of gas within the pore spaces). The other portion of the scatter is believed to be the result of real compositional differences as confirmed by the MSCL results.

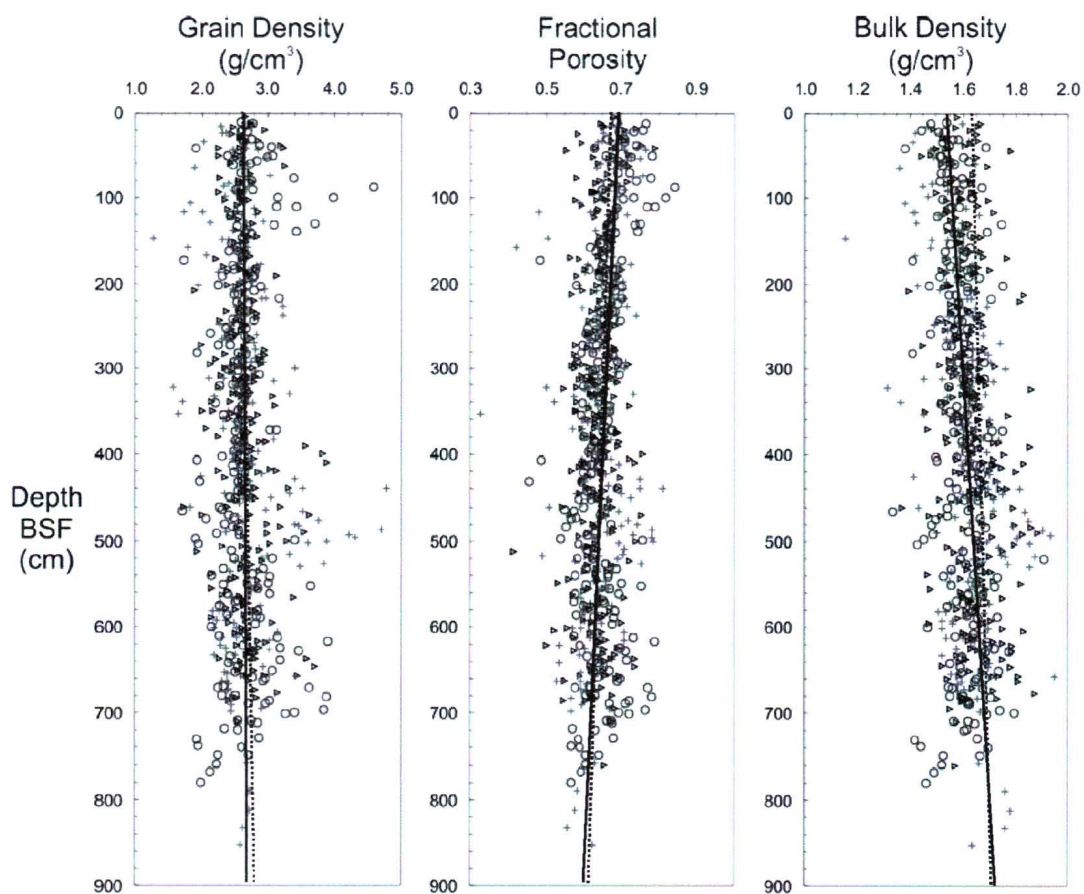


Figure 3.2. a) Grain density, fractional porosity, bulk density and their trend lines (solid lines) for cores at Blank Zone 1. Triangles represent cores located within the seismic blanking zone (C3-6, C18-21), circles represent cores located near the boundary on the seismic blanking (C9-10), and pluses represent cores located outside the blanking zone (C2, C7-8, C22). Dotted lines indicate ODP 146 trends for measurements down to 8 m BSF.

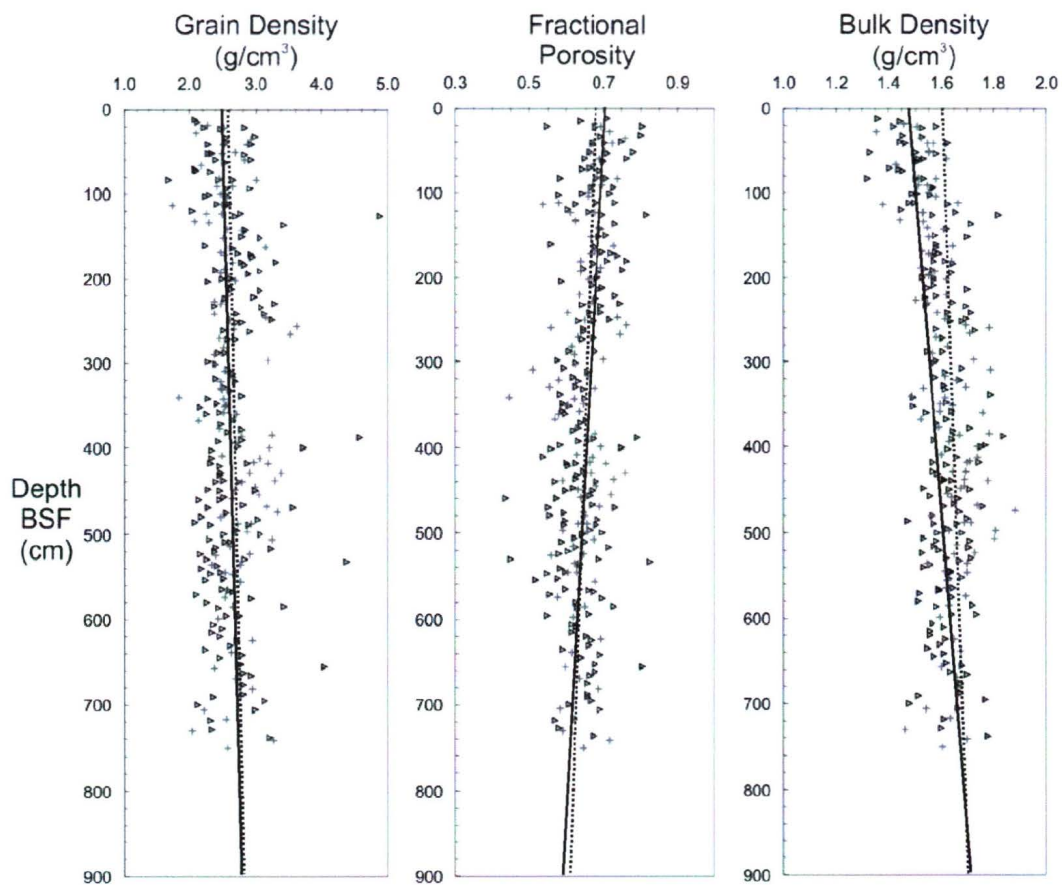


Figure 3.2. b) Grain density, fractional porosity, bulk density, and their trend lines (solid lines) for cores at Blank Zone 4. Triangles represent cores located within the seismic blanking zone (C12-14), and pluses represent cores located outside the blanking zone (C16-17). Dotted lines indicate ODP 146 trends for measurements down to 9 m BSF.

3.3. MULTI-SENSOR CORE LOGGER

The Multi-Sensor Core Logger instrument was used on cores 18 to 26 (excluding core 23), about two weeks after the core recovery, at University of Washington (see Methods section). The cores were analyzed for magnetic susceptibility, P-wave velocity, and bulk density. The data were corrected for inferred shifts in bulk density and fractional porosity data sets (see Data Correction section) (Figure 3.3 and 3.4). The MSCL magnetic susceptibility data especially mimicked the individually measured magnetic susceptibility. The same pattern of lower magnetic susceptibility values mentioned previously was also observed in the MSCL data for the cores located within the region of seismic blanking (Figure 3.3). This result served as an indication of the validity of the both methods. MSCL P-wave velocity data also agreed very well with the manually collected velocities (Figure 3.4). The MSCL P-wave velocities within the top 2 m of the cores located within the seismic blanking were slightly higher than for the core located outside the area (i.e. approximately 1500 m/s versus 1480 m/s, respectively). The MSCL measurements for velocity sometimes extended to greater depths than the individual measurements did; however, these results should be viewed with caution due to the presence of gas expansion cracks and the absence of visual control during measurements. MSCL bulk density and fractional porosity trends were as expected, with bulk density increasing and porosity decreasing with depth. The top two metres of the core located outside the blanking area (core 22) had slightly lower bulk density values than the cores located inside the blanking (i.e. approximately 1.5 g/cm³ versus 1.6 g/cm³, respectively).

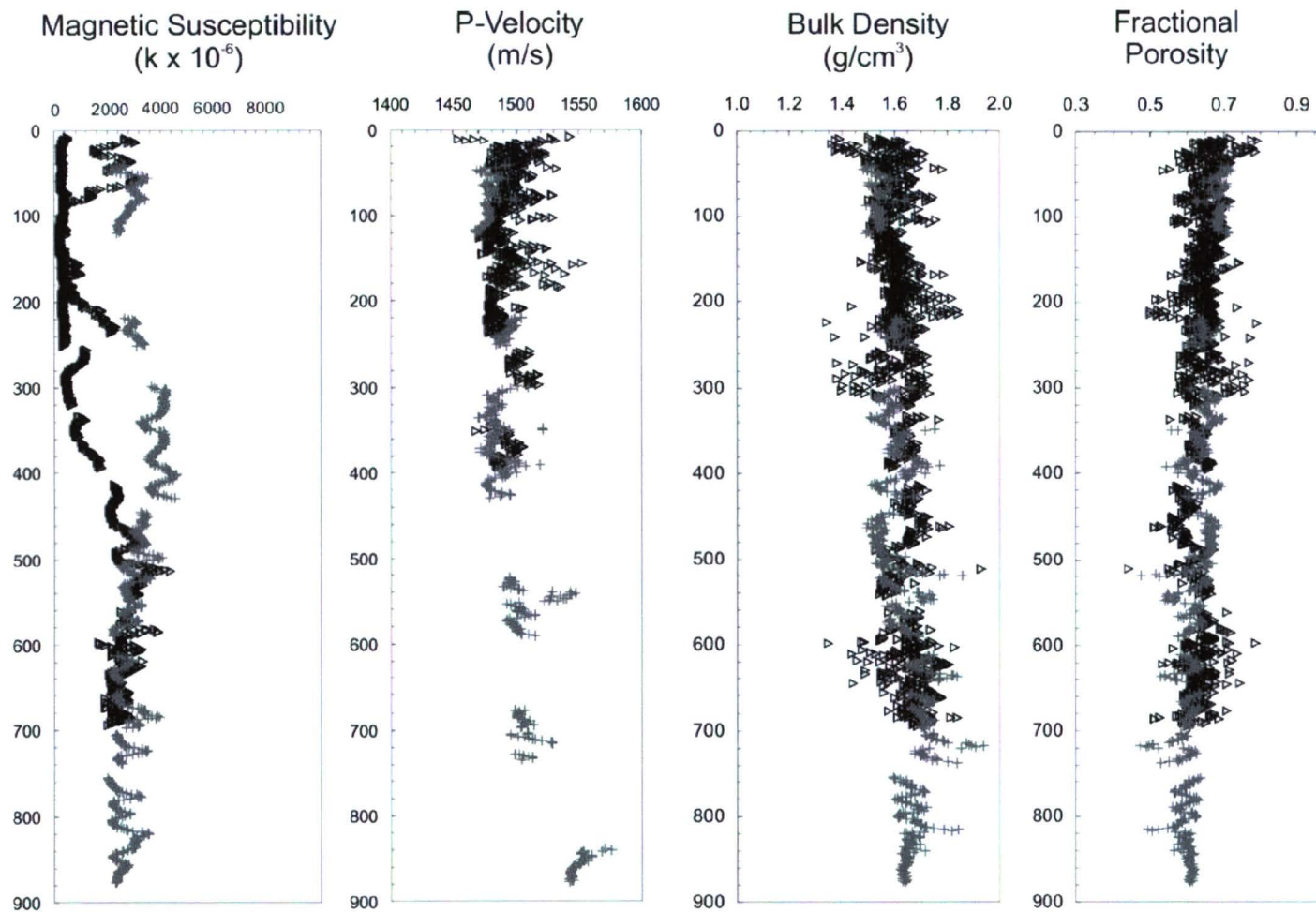


Figure 3.3. Magnetic susceptibility, P-velocity, bulk density, and fractional porosity measured using MSCL for the region of Blank Zone 1. Triangles indicate measurements for cores within the observed seismic blanking area (C18-21), and pluses indicate measurements for cores located outside the seismic blanking area (C22).

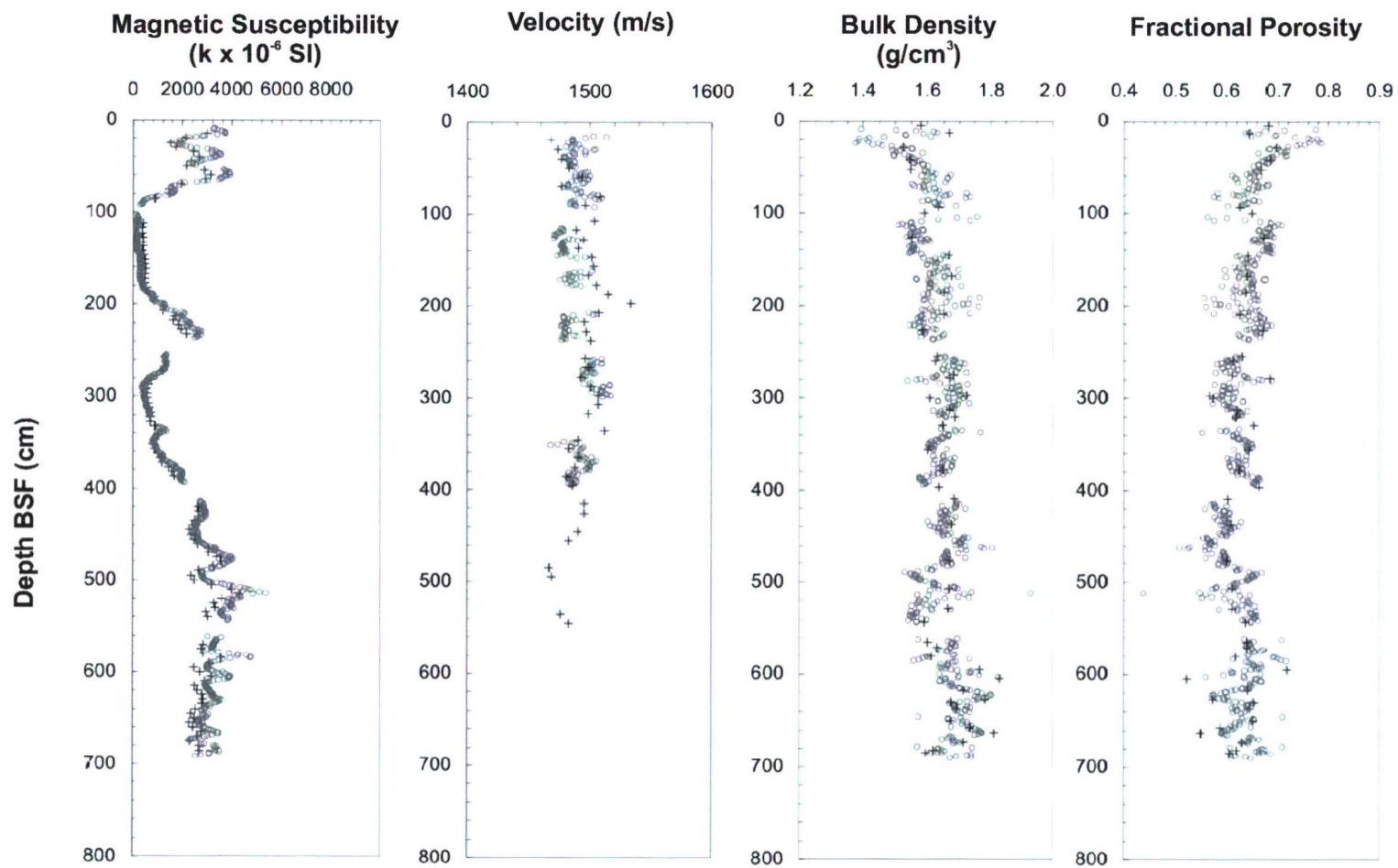


Figure 3.4. Physical properties for core 19. Circles indicate data acquired Multi-Sensor Core Logger (MSCL) and pluses indicated data acquired manually.

3.4. SEDIMENTOLOGY

Cores 9, 11, 19, 20, and 22 were chosen for sedimentological analysis with the guidance of Dr. T. S. Hamilton. Core 19 is located within the blanking area. Core 20, also located within the area of blanking, contained massive hydrate. Cores 9 and 11 are located on the perimeter of the blanking, and core 22 is located outside the vent area away from any vent-related interactions. General descriptions of most cores are given in Appendix B, while detailed descriptions and photographs cores chosen for sedimentological analysis are given in Appendix C and the supplementary CD-ROM, respectively.

Several important observations are noted. There is authigenic pyrite within the sediments of the cores located within the blank zone (Figure 3.5). Pyrite was seen to occur at various intervals starting from ~80 cm. The pyrite is present as euhedral granules, infilling of small burrows, partial or complete foraminifera tests replacements, etc. Often, within the same interval, there is an appearance of pink and/or orange organic slime, possibly of bacterial origin, within sub-vertical cracks and vugs (Figure 3.5). The organic slime changed its colour to clear-white after being exposed to air. Pyrite is completely absent in Core 22 located outside the vent. This latter core, on the other hand, has minor amounts of magnetite present in the top 2 m of the sediment. The hydrate core differed from the other cores in that it contained small amounts of beige carbonate crusts. The crusts were soft and internally of very fine grain size. In most cores, charcoal coloured bands and sand sized dull black, soft, earthy carbonaceous spherules were found at depths > 340 cm BSF (Figure 3.5). This dark material whose origin and composition has not yet been determined was less abundant in the core located outside the vent area.

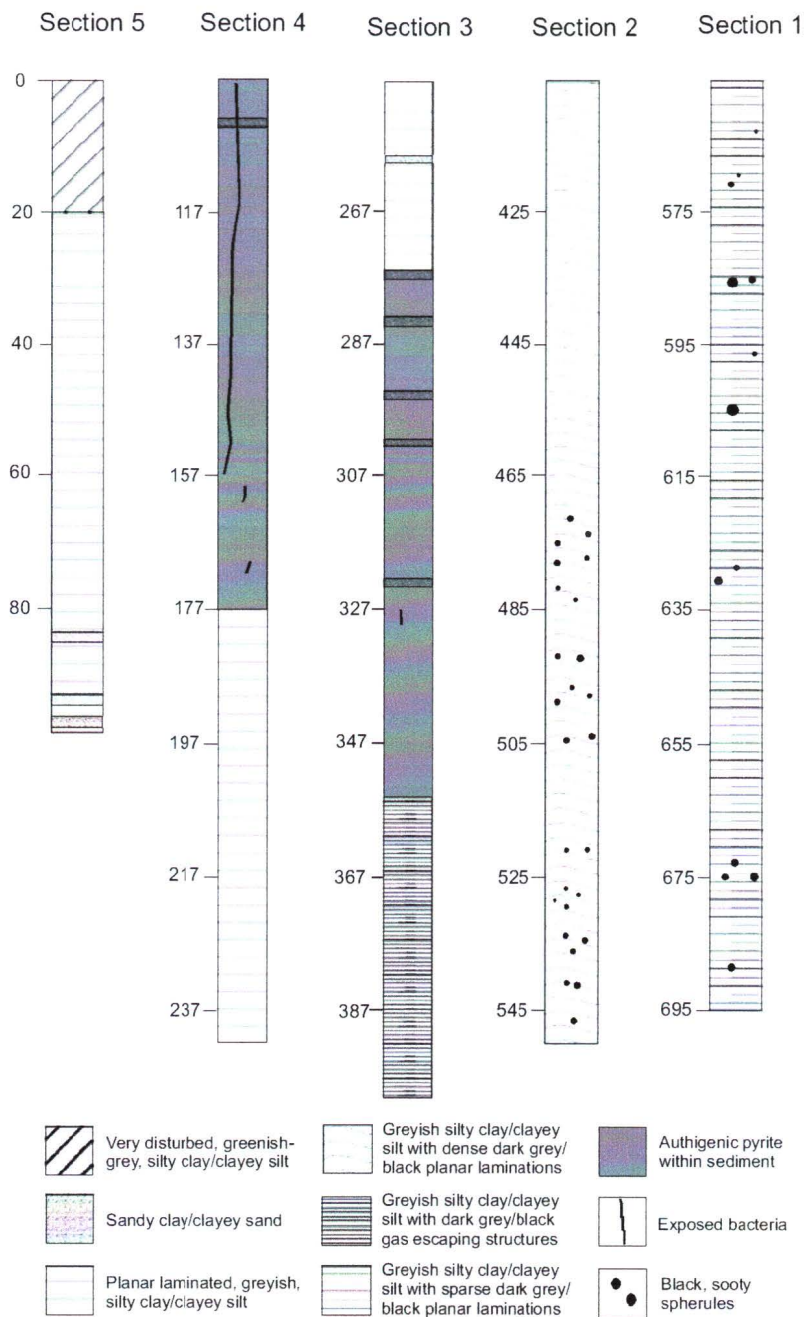


Figure 3.5. Detailed sedimentological description of core 19.

CHAPTER 4

DATA SYNTHESIS – DISCUSSION

4.1. POROSITY PREDICTION VIA ARCHIE'S LAW

In this section the relationships among the physical properties and index values are examined, along with comparison to various theoretical relations. During PGC00-02 scientific cruise, several different physical properties were measured including electrical resistivity and density (see Data Acquisition section). No corrections were applied to the resistivity data; formation factor, or the ratio of the sediment electrical resistivity and the pore water resistivity (Archie, 1947), was calculated directly from the measured voltages (see Data Acquisition section). The sections of the cores that contained hydrate were quite disturbed and often lost so measurements on these sections were omitted. Thus changes in pore fluid salinity resulting from gas hydrate dissociation were not recorded and it was assumed that no other major pore fluid salinity variations were present. Boyce (1968) states that formation factor is insensitive to minor salinity changes, and thus the changes in resistivity can be attributed to sedimentological differences, i.e., variations in porosity microstructure.

Archie's Law provides an empirical relationship between the formation factor, F , and porosity, ϕ , for water saturated rocks:

$$F = a\phi^{-m}$$

where a is the tortuosity coefficient which is affected by the pore space connectivity and thus diagenetic history of the rock and, and m , the cementation coefficient, is assumed to be constant for a given rock type. Archie's Law is thus a helpful tool in determining the amount of fluid present within the sediment when only electrical resistivity measurements are available.

Corrected porosity values for Blank Zone 1 were plotted against depth-equivalent formation factor values (Figure 4.1). Due to the proximity of the ODP site 889/890, it was reasonable to assume that the type of sediments in both sites were similar and had similar cementation coefficients. Thus, assuming the same m value of 1.76 as was used during ODP Leg 146, the average a value for all cores in Blank Zone 1 was calculated to be 1.11. This value of a is significantly less than the a value of 1.41 calculated during

ODP Leg 146 and is very similar to the results of Mi (1998) whose survey area was also in the vicinity of PGC00-02. However, Mi (1998) concluded that his a values are small due to dehydration of the cores which experienced a long period wait of up to 1 year, before any core measurement. The same reasoning cannot apply in this new data set. The majority of core measurements and density sampling were done only a day or two after the core recovery. Following that, special care was taken to minimize any evaporation during the two-week long density sample storage. The samples were kept in a cold room in tightly sealed glass vials.

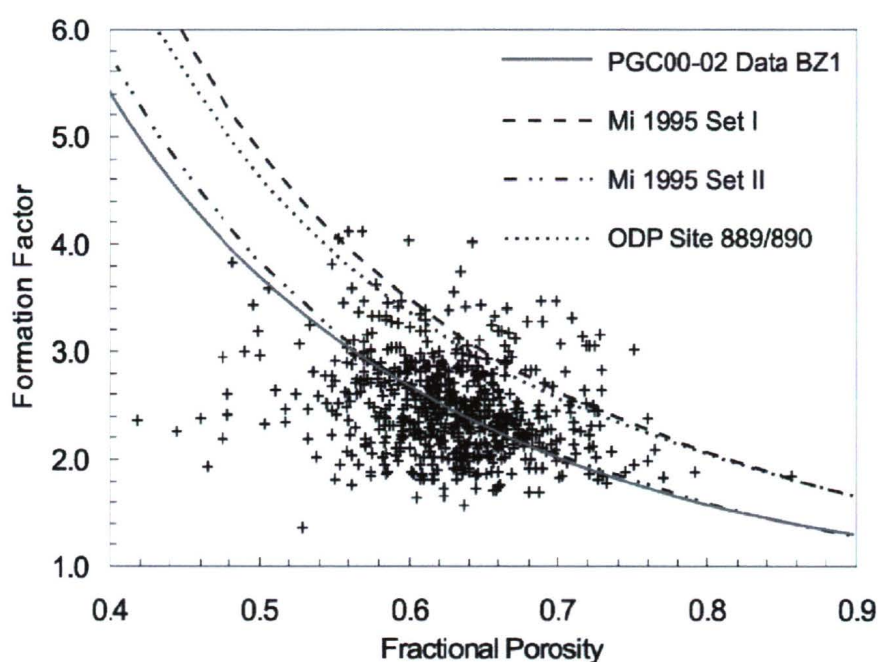


Figure 4.1. Formation Factor vs. Fractional Porosity for Blank Zone (BZ) 1. Archie's Law fit for PGC00-02 data set ($a=1.11$, $m=1.76$) is consistent with Mi 1995 Set II ($a=1.10$, $m=1.84$), but different from Mi 1995 Set I ($a=1.40$, $m=1.84$) and ODP Site 889/890 ($a=1.41$, $m=1.76$).

Tortuosity coefficient values of the sediment are strictly dependent on the post-depositional, diagenetic history of the sediments (Gueguen and Palciauskas, 1994). Thus, the discrepancy between the tortuosity coefficients could be caused by the presence of gas hydrates and/or elevated concentrations of methane flux. Post-depositional alteration of the sediments is clearly indicated by the presence of authigenic carbonates on the sea

floor. Other indications of unique diagenetic processes will be discussed in the following sections.

The calculated a and m values of 1.76 and 1.1, respectively, were then used to predict porosity using formation factor. Figure 4.2 shows the graph of measured and predicted porosity with depth for core 19. The overall trend between the two data sets is very similar; however, there is disagreement in the smaller scale features. For example, at 350 cm depth, the measured porosity increases with respect to the previous measurement, whereas the predicted porosity value decreases.

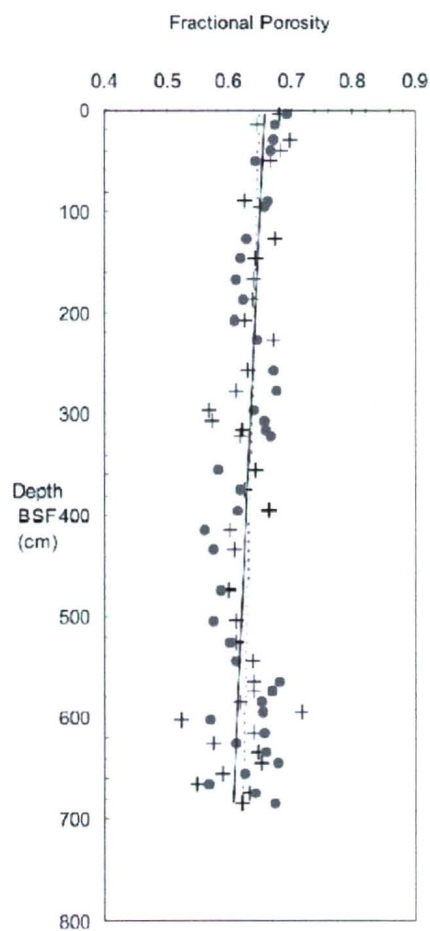


Figure 4.2. Measured (pluses) and predicted (filled circles) fractional porosities for core 19. Solid line and stippled lines represent measured and predicted data trendlines, respectively.

In order to examine the possible causes of this relatively poor detailed relationship between the formation factor and porosity, the porosity data collected using a Multi-Sensor Core Logger (MSCL) were examined. Figure 4.3 shows a plot of MSCL porosity and plug porosity data against formation factor for core 19. There is very little difference in the scatter of the two data sets. Following the independent analysis of MSCL porosity data, it is believed that the reasons for the scatter are due to significant small-scale variations in both porosity and resistivity. A portion of these variations could be related to the measuring procedure, since it was often impossible to measure both density and resistivity of the same sediment volume (see Figure 2.5), whereas the other portion of the scatter in these measurements is likely due to real variations in the sediment. Thus, precise correlation of the data sets was unattainable, causing scatter in the small-scale formation factor-porosity relationship.

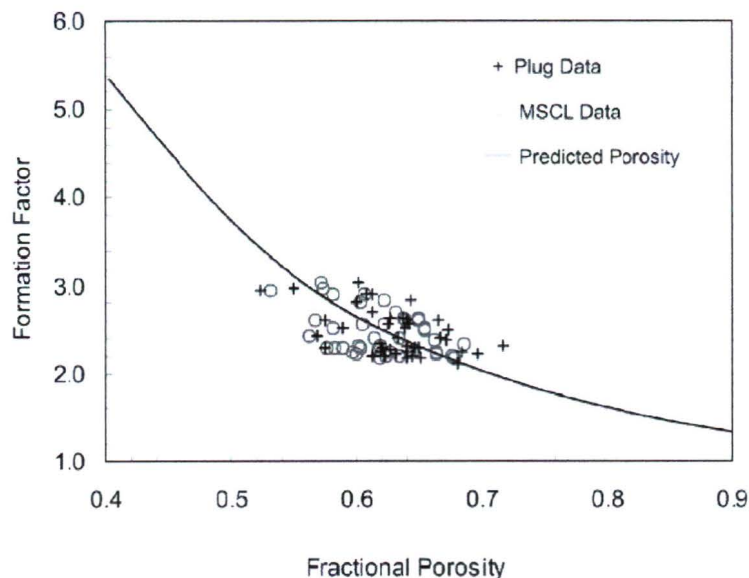


Figure 4.3. Fractional Porosity-Formation Factor plot for core 19. Shown on the diagram are two data sets. The MSCL data set consists of porosity values which were measured using Multi-Sensor Core Logger and manually measured formation factors, whereas the Plug data set consists of porosity and formation factor values that were both manually measured. The solid line indicates the predicted porosity-formation factor relationship using Archie's Law fit for Plug data set ($a=1.11$, $m=1.76$) (see figure 4.1).

4.2. VELOCITY-POROSITY DATA ANALYSIS

The velocity-porosity relationship was examined using: 1) individually measured porosity and velocity, 2) porosity predicted from resistivity (see Porosity Prediction via Archie's Law section) and individually measured velocity, and 3) velocity and porosity measured using Multi-Sensor Core Logger (MSCL). The three data sets were plotted for core 19 (Figure 4.4). The individually measured and predicted data sets show very large scatter about the center (i.e. velocity of 1490 m/s and fractional porosity of 0.62). No clear correlation between velocity and porosity can be observed from these two data sets. The MSCL data set, in contrast, shows a clear trend of decreasing velocity with increasing porosity.

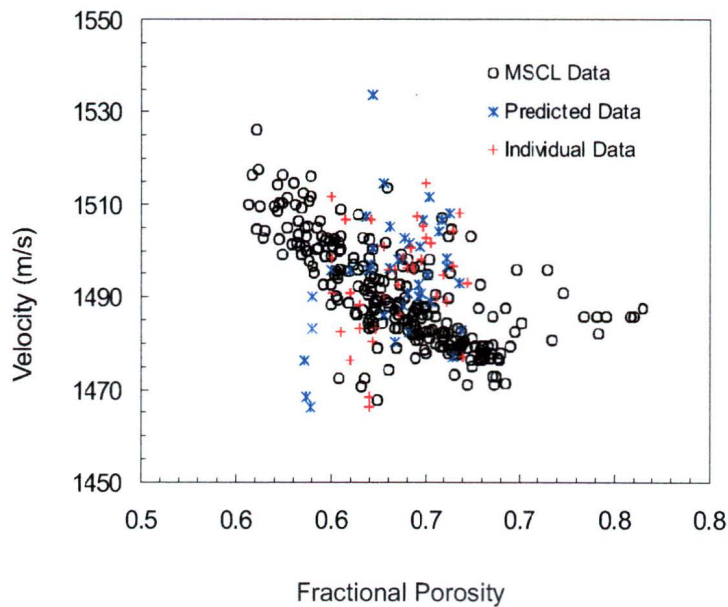


Figure 4.4. Velocity-porosity plots for core 19. Shown on the diagram are three data sets acquired using different techniques: 1) velocity and porosity measured using Multi-Sensor Core Logger (MSCL); 2) predicted porosity via Archie's fit using individually measured resistivity and individually measured velocity; and 3) individually measured porosity and velocity.

The existence of a clear correlation in MSCL data set, and lack thereof in the manually measured data sets, might imply that the latter are inconsistent and noisy. However, it is the author's opinion that the reason for such scatter may not be entirely

due to noisiness in the porosity data sets, but may also be due to the nature of the velocity measuring procedure. The sedimentation rate in the study area is relatively low and abundant thin sedimentary layers (i.e. 2-5 cm thick) were observed during sedimentological analysis. As explained in the methods section, the velocity transducers were oriented parallel to the liner and approximately orthogonal to the sedimentary layering (Figure 2.7). Because the transducers were about 7 cm apart, this would imply that in some cases the P-wave passed through several sedimentary layers, and the value measured for that interval is an average P-wave velocity. The sampling plug and the resistivity probe covered less than 2 cm of sediment, and thus did not sample the same sediment as the velocity measurements. Moreover, the location of the resistivity and density samplings were not always exactly the same, causing discrepancies between those values as well. The velocity transducers of the MSCL are oriented orthogonal to the core liner and thus almost parallel to the sedimentary layers within the core. Thus, both velocity and porosity measurements appear to more closely sample the same sedimentary material.

Figure 4.5 shows the comparison of MSCL velocity-porosity data for Blank Zone 1 with data collected during ODP Leg 146 from the Cascadia accretionary prism (Jarrard *et al.*, 1995), and data collected during ODP Leg 131 from the Nankai accretionary prism (Hyndman *et al.*, 1993). An empirical polynomial relationship based on porosity and velocity measurements from the Nankai prism was proposed by Hyndman *et al.* (1993):

$$\phi = -1.180 + (8.607V^{-1}) - (17.89V^{-2}) + (13.94V^{-3})$$

where V is velocity in km/s. Although, the empirical relationship was originally based on the measurements on deeply penetrating drill cores from Nankai prism, it has since been used by Jarrard *et al.* (1995) and Yuan *et al.* (1994) in predicting porosities of sediments at the Cascadia margin. There is a definite difference in data coverage between the three data sets. In the present study, porosities were relatively high, ranging from about 0.55 to 0.75, while velocities were very low and showed little variation, with most values between 1470 and 1520 m/s. The ODP data sets cover much greater range of both porosities and velocities (0.35 to 0.80 and 1500 m/s to >2000 m/s). This discrepancy is likely due to the depth range sampled. The sediment examined in this study represents

the top several metres of the sea floor, while the other two studies examined much deeper sediments at depths of several hundred meters.

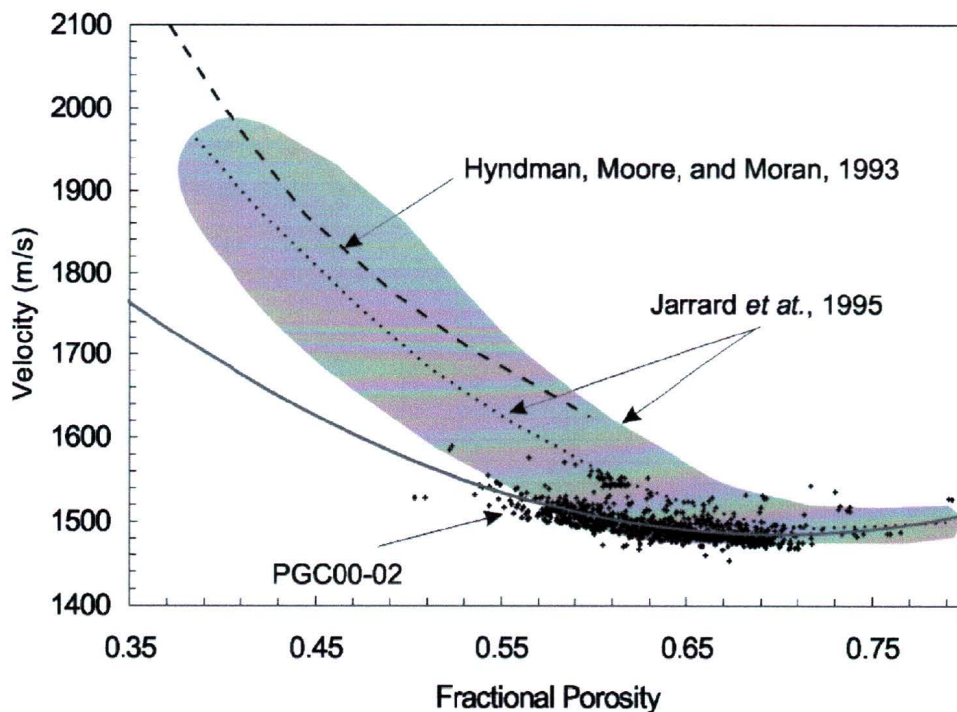


Figure 4.5. The velocity-porosity graph for Blank Zone 1 using Multi-Sensor Core Logger (MSCL) data set. The best-fit relationship for this data set is represented by the solid curve. Also shown are the best-fit curve by Hyndman, Moore, and Moran (1993) from Nankai accretionary prism (stippled curve), and the best-fit curve by Jarrard et al (1995) for unfractured, unconsolidated ODP 146 sediments (dotted line). The shaded area represents ODP 146 data coverage and shows its partial overlap with values from this study.

Moreover, there is much greater porosity variation than would be predicted from the standard Athy's Law relation based on normal compaction of sediments due to loading:

$$\phi = \phi_0 e^{-Z/L}$$

where ϕ_0 is the surface sediment porosity, Z is the depth, and L is the characteristic decay constant. The measured values from this study range from approximately 1470 m/s to 1520 m/s for velocity, and from 0.55 to 0.75 for porosity. The surface porosity for these

sediments was assumed to be 0.70 and the best fitting decay constant was found to be 8 m (Figure 4.6). ODP Leg 146 results, based on deep sediment porosity trends yielded a surface porosity value of 0.60 and a decay constant of 4000 m (Westbrook *et al.*, 1994). As seen on Figure 4.6 their results underestimate measured change in porosities over this depth interval. For the near surface sediments, the observed decay constant is a factor of 500 smaller than that predicted from the deeper trends. Mi (1998) also observes this discrepancy in the porosity-depth function of the shallow sediments. This may indicate a the threshold for “permanent” onset of diagenetic changes through sediment compaction and thus fundamental difference in the nature of sediment compaction in the upper several metres below the seafloor relative to the deeper sediments.

The unique nature of deep-marine seafloor sediments has been reported by many authors over the last few decades (e.g., Bennett *et al.*, 1970; Booth and Dahl, 1986; Boudreau, 1998). Since then, it has been found that depositional activities of sediment are not just affected by the overburden stress, but are also a function of the nature of microfabric, amount of organic matter, mineralogy, and grain size, shape, etc. (Bennett *et al.*, 1999). For example, presence of clays, especially the mineral smectite, can significantly increase the expected porosity and water content within the top few metres of the sediment (e.g., Velde, 1996; Bennett *et al.*, 1999). This phenomenon, often referred to as flocculation, is attributed to the clay’s active electrostatic forces that allow ‘edge-edge’ assemblage of the clay platelets and thus increased water content filling the voids (Velde, 1996).

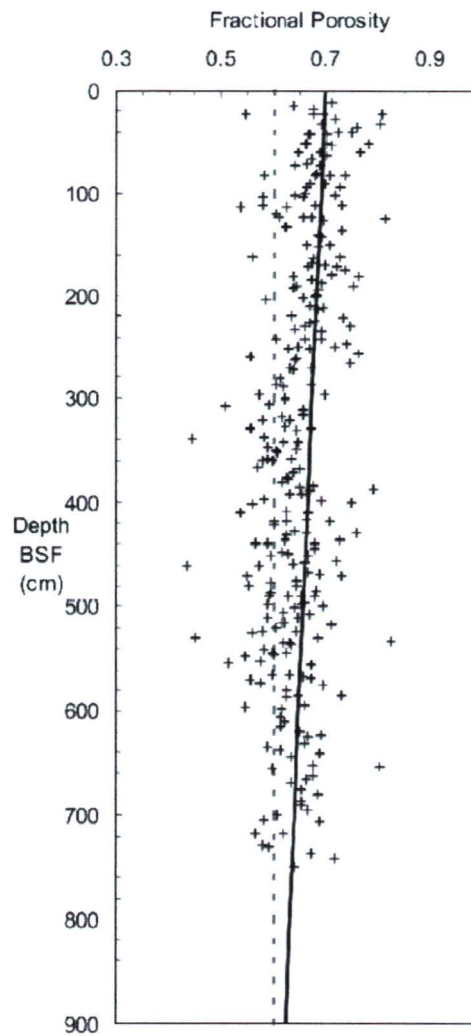


Figure 4.6. Fractional porosity with depth for Blank Zone 1. The dashed line indicates Athy's law using ODP Leg 146 parameters (surface porosity value of 0.60 and a decay constant of 4000 m), whereas the solid line indicates Athy's law using parameters from the present study determined from near-surface sediments only (surface porosity value on 0.70 and a decay constant of 8 m).

4.3. THERMAL CONDUCTIVITY HIGH – PRESENCE OF AUTHIGENIC CARBONATE

Thermal conductivity data for this study were acquired using a pulsed needle probe measuring apparatus as described above. They were compared to the data acquired at the same location, ± 20 m, in-situ during heat flow surveying and compiled by T. Lewis of GSC-PGC, Sidney, BC (Figure 4.7). There is good agreement between the two data sets, suggesting the validity of both methods.

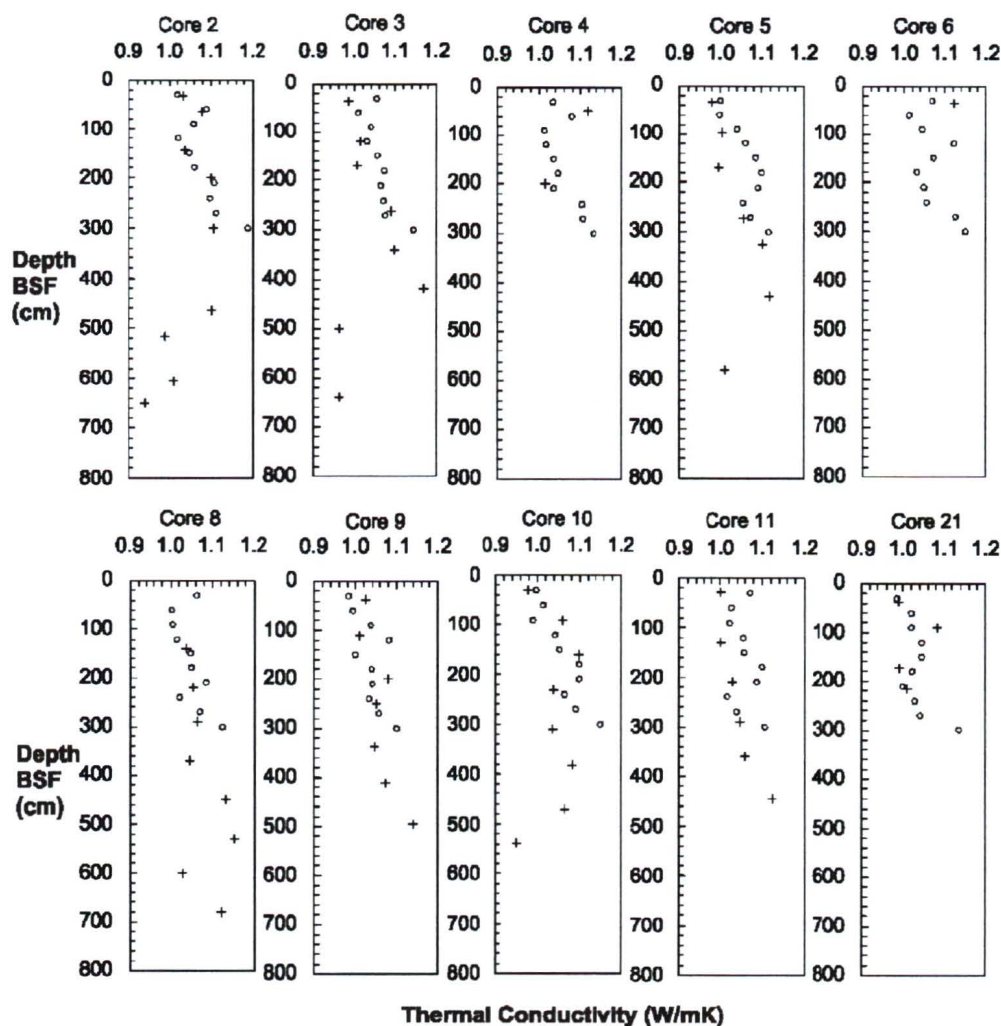


Figure 4.7. Thermal conductivity with depth for Blank Zone 1. Crosses represent measurements conducted on cores using needle-probe measuring apparatus. Circles represent measurements done in-situ at core sites using a 3m-long Lister-type probe during heat flow surveying.

Thermal conductivity of sediments is mainly influenced by the water content of the sediments and can be described well with a weighted geometric mean relationship between water and sediment porosity (Davis *et al.*, 1990):

$$\kappa = \kappa_f^\phi \kappa_s^{1-\phi}$$

where κ_f is the conductivity of fluid, κ_s is the mean grain conductivity or the conductivity of the sediment, and ϕ is porosity. To examine the nature of thermal conductivity, the measured results were compared to the thermal conductivity results predicted from a formula suggested by Davis *et al.* (1990) which uses the geometric mean model and a mean grain conductivity of 2.4 W/mK which is a reasonable value for clay mineral smectite-rich sediment:

$$\kappa = 1.07 + 5.86 \times 10^{-4} z - 3.24 \times 10^{-7} z^2$$

where z is the depth below the seafloor in m. As shown in Figure 4.8, it is evident that the predicted and measured thermal conductivities agree fairly well. The only obvious divergence from this observation is the increased thermal conductivity of cores that had contained gas hydrate. The measurements on these cores were only conducted on sections that were above gas hydrate and were thus not affected by the post-extraction dissociation of hydrate.

An increase in thermal conductivity can be due to physical and/or mineralogical changes. Brigaud and Vasseur (1989) showed that clay and carbonate content have a significant influence on thermal conductivity. Because all cores within the Blank Zone 1 are closely spaced, it is assumed that clay content does not differ substantially for cores with and without hydrate. Thus, a thermal conductivity increase observed in gas hydrate sediments can possibly be attributed to the changes in carbonate content.

An increase in carbonate content of gas hydrate cores is very likely. If there is an upward flux of methane going through these sediments, in the presence of bacteria, the methane will be oxidized possibly near the depth to no sulfate by the following reaction (Ritger *et al.*, 1987):



This will allow the newly released carbon to form authigenic carbonate and provide HS^- for the diagenetic formation of pyrite (see following section).

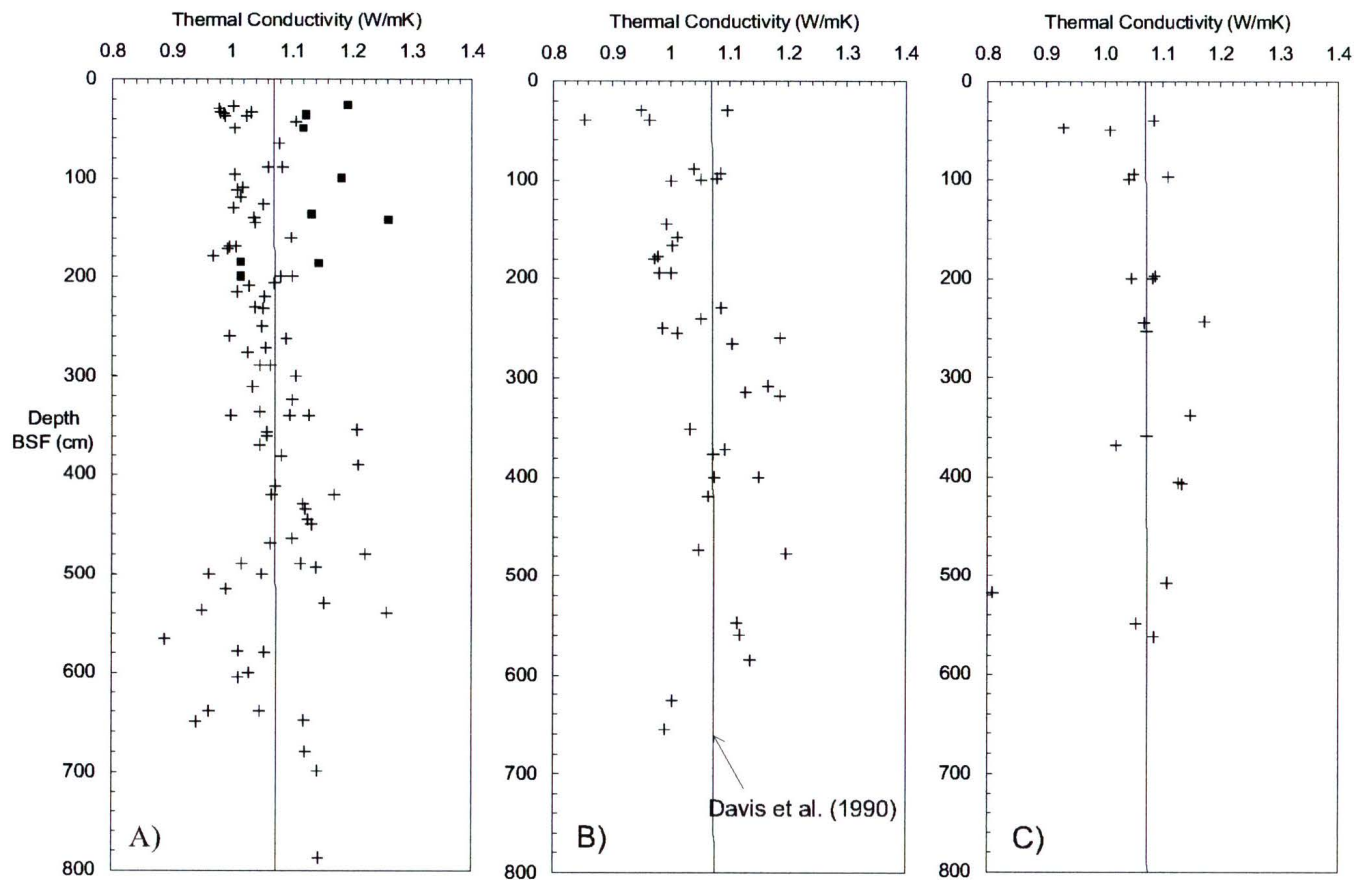


Figure 4.8. Needle-probe thermal conductivities for cores located within Blank Zone 1 (a), Blank Zone 4 (b), and for cores located outside the vent field (c). Filled Squares represent cores containing gas hydrate. Solid line indicates the predicted thermal conductivities using average grain and fluid conductivities (Davis et al., 1990).

Thermal conductivity and porosity values of these sediments were combined and compared to the ODP Leg 146 results (Figure 4.9). The expected relationship of thermal conductivity increase with porosity decrease can be observed. However, the trend for this study is substantially higher in porosity than the ODP Leg 146 values, thus resulting in a much higher mean sediment conductivity of 3.4 W/mK. This discrepancy could be attributed to mineralogical differences between the studied sediments (i.e. higher clay mineral kaolinite content can increase thermal conductivity value). However, when comparing this study's data to only the top 10 m of ODP data, it appears that the results do agree. Thus, one can conclude that the surface few metres of sediments generally do not follow the same trend as deeper sediments.

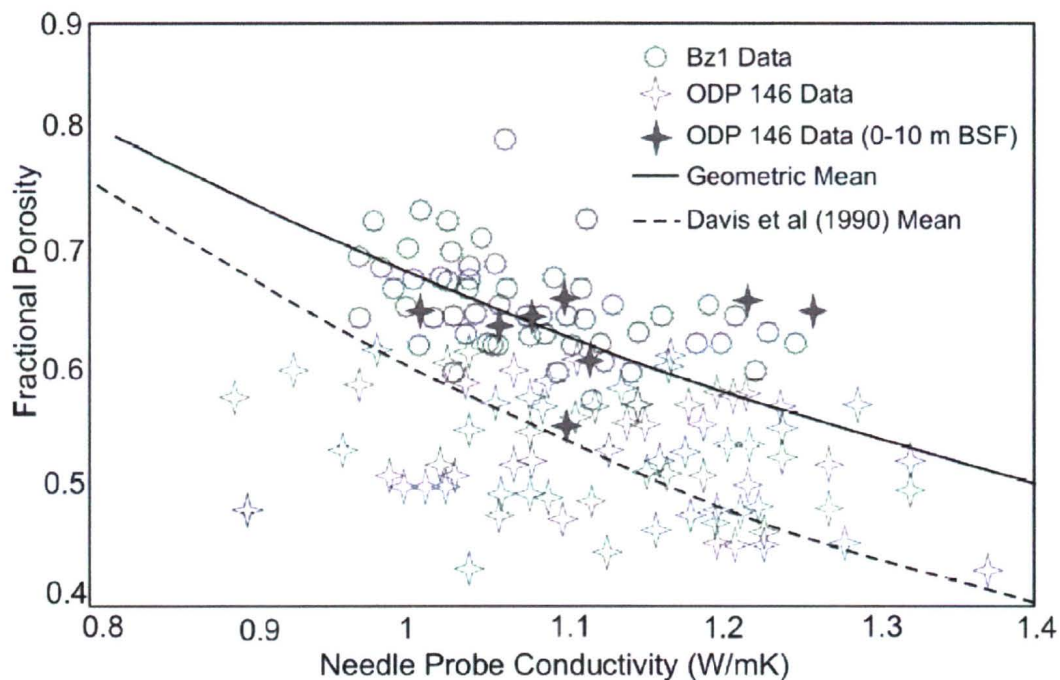


Figure 4.9. Needle-probe thermal conductivities versus depth equivalent fractional porosity for Blank Zone 1. Circles indicate this study's data sets, whereas stars indicate ODP Leg 146 data sets. Filled stars indicate ODP data for depths up to 10 m BSF. Solid line represents geometric mean with grain conductivity (k_g) of 3.4 W/mK. Dashed line represents geometric mean for Cascadia margin sediments with grain conductivity of 2.4 W/mK (Davis et al., 1990).

4.4. HIGH REFLECTION COEFFICIENT ZONE – DISSEMINATED CARBONATE HYPOTHESIS

In seismic reflection data, some areas exhibited unusually high seafloor reflection coefficient. In this section correlations with carbonate and thus upward methane flux are examined.

Reflection coefficient, RC, was calculated using the following formula:

$$RC = (\theta_1 v_1 + \theta_2 v_2) / (\theta_1 v_1 - \theta_2 v_2)$$

where θ_1 is density of sea water, assumed to be 1.024 g/cm^3 , v_1 is velocity of sea water, measured to be 1486 m/s , and θ_2 and v_2 are average density and velocity. Reflection coefficients were calculated using the average velocity and density values from the seafloor to a maximum depth increasing in intervals of 1 m , thus giving the same resolution as with 4 m seismic wavelength or $\sim 375 \text{ Hz}$ seismic data. These interval reflection coefficients were plotted along the two transects crossing Blank Zone 1 (Figure 2.2). The reflection coefficients were calculated for a maximum depth of 7 m for core 7 and 8, and a maximum average depth of 4 m , approximately equaling to 16 m seismic wavelength or $\sim 100 \text{ Hz}$ seismic data (Figure 4.10).

The calculation of interval reflection coefficients for gas hydrate core 4 were omitted due to a lack of complete and reliable measurements of velocity and density. For gas hydrate cores 6 and 20, average reflection coefficients with respect to seawater were calculated only to depths of 1 and 2 meters, respectively, also due to the same problem. However, it is evident that these two cores have noticeably higher reflection coefficient at given intervals than the rest of the surrounding cores. Furthermore, the reflection coefficient for core 20 unexpectedly decreases with depth. The individual measurements of density and velocity were examined for the higher reflection coefficient cores (C6 and C20) and the lower reflection coefficient cores (C3, C5, C11, and C21) (Figure 4.11). Both density and velocity values within gas hydrate cores are higher by approximately 0.1 g/cm^3 and 20 m/s , respectively. Although these differences are minor, they are nevertheless consistently observed features.

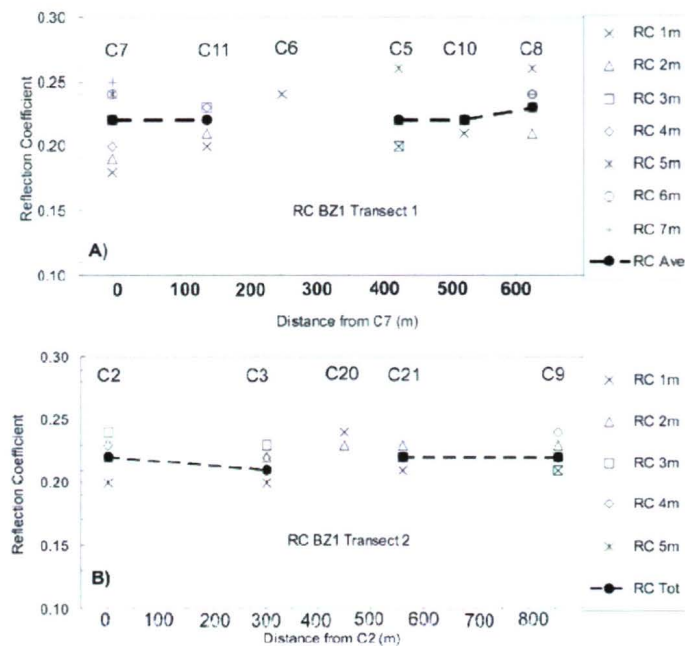


Figure 4.10. Reflection coefficients (RC) determined by averaging velocities and densities over core lengths of 1, 2, 3, and 4m, as well as the entire core length. Transect 1 (A) and Transect 2 (B) are perpendicular transects which cross within Blank Zone 1 (see figure 2.2).

The reflection coefficient values were compared with those calculated by Riedel (2001) for the same area (Figure 4.12). Riedel (2001) analyzed seafloor amplitudes of surface seismic data, and found a reflection coefficient low in the same area of this study's reflection coefficient high. However, for his data set, he used Teledyne single channel streamer which recorded a single 40 in³ airgun with a dominant frequency of about 150 Hz. The seismic data cannot resolve features less than one-quarter of a wavelength, so for a dominant wavelength of 10 m this resolution limit is 2.5 m. Thus, the seismic data cannot resolve the high-reflectivity layer inferred for the upper 2 m of cores C6 and C20. In fact, where velocity/density gradients are involved, the seismic data may be most sensitive to the reflection coefficient averaged over the top 5 to 10 m. Furthermore, the reflection coefficient change calculated with depth does not conflict with the interpretation of a high-velocity hydrate lens in Blank Zone 1 observed on deep-tow seismic profile data (Figure 4.13) and also on single channel Teledyne data. This

reflector is lost in the core data because the cores penetrate only the top 8 m at most, and the high reflectivity lens tapers off away from the centre.

During the 2000 piston coring scientific cruise, no seafloor carbonate pavement was recovered. All cores were able to penetrate through the sediment. Thus, the elevated reflection coefficient of the two cores is most likely not due to the presence of seafloor carbonate pavement, but could be due to the presence of disseminated carbonate within the sediment matrix. This would also be in the agreement with the thermal conductivity high found for the top sediments of these cores.

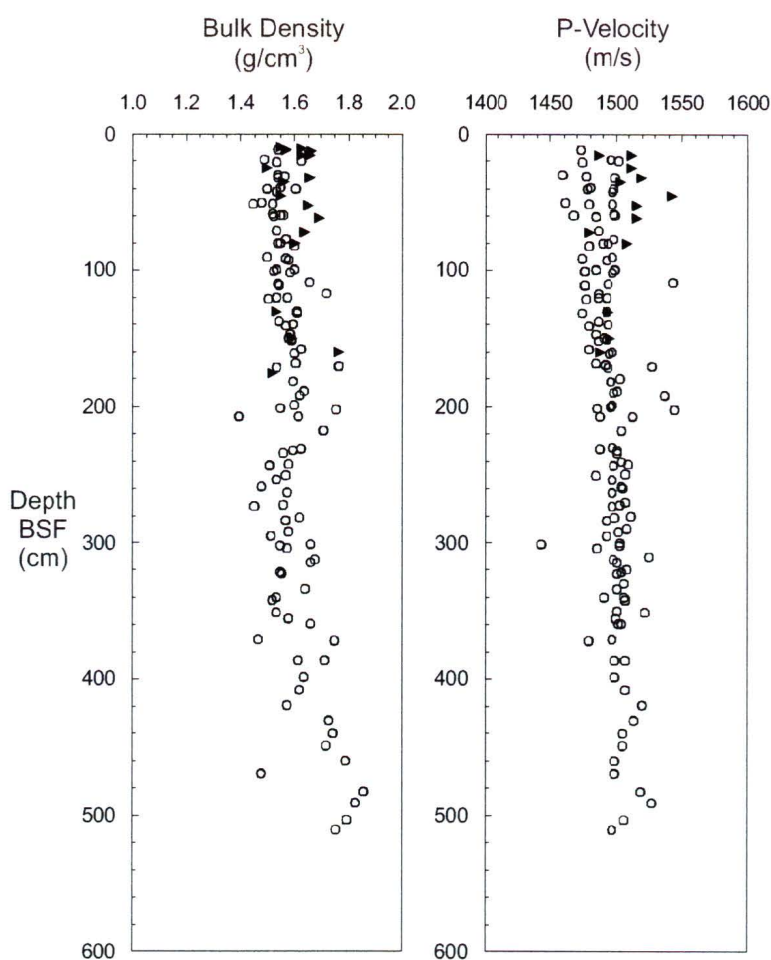


Figure 4.11. Graphs illustrating the differences in bulk density and P-velocity for cores with different reflection coefficients (see figure 4.5). Cores with high reflection coefficient of 0.24 (C6 and C20) are represented by triangles, and cores adjacent to them with low reflection coefficient of 0.19 (C3, C5, C11, and C21) are represented by circles.

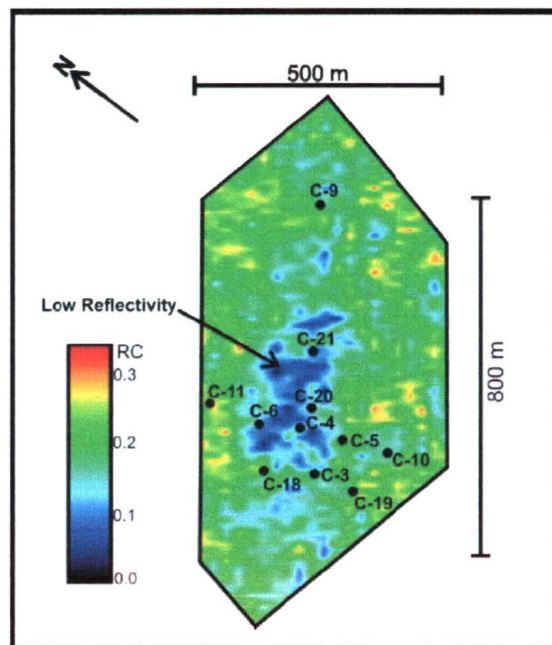


Figure 4.12. Seafloor reflection coefficient within Blank Zone 1 calculated by using single channel seismic data (after Riedel, 2001).

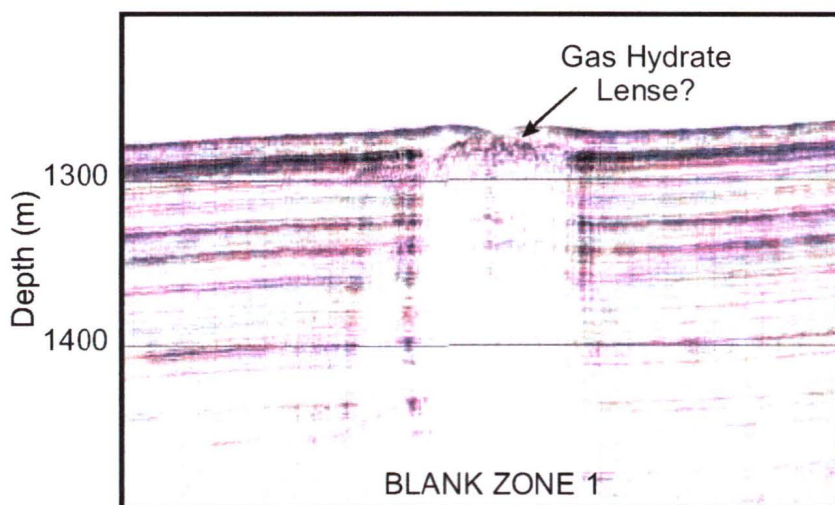


Figure 4.13. Deep-tow seismic profile above Blank Zone 1, showing a strong gas hydrate reflector just below the sea floor (Wood, 2001, pers.com.).

4.5. MAGNETIC SUSCEPTIBILITY ZONATION

4.5.1. Association of Low Magnetic Susceptibility with Presence of Pyrite

The magnetic susceptibility results with depth for all cores (Figure 3.1) exhibit a pattern for the cores located within the extent of actual seismic blanking relative to those outside. The cores from within the area of blanking had an anomalously low magnetic susceptibility mostly between 50 and 500×10^{-6} SI. The cores that were located outside of the blanking had much higher magnetic susceptibilities, ranging from 2000 to 4000×10^{-6} SI. Cores that were located outside, but very close to the seismic blanking, had a combination of higher and lower magnetic susceptibilities that varied with depth. This pattern is shown for two perpendicular transects in Figure 4.14 (a) and (b). A 3-D representation of this zonation is shown in Figure 4.15. The same pattern was also observed for Blank Zone 4 (Figure 3.1b). Outside the vent field region (Figure 3.1c), magnetic susceptibility values were similar to those for cores located within the vent field but outside the seismic blanking (i.e. 2000 to 4000×10^{-6} SI).

Magnetite, a highly magnetic mineral, is part of the primary detrital mineralogy of the marine sediments (e.g. Kobayashi and Nomura, 1972). Unlike pyrite, the mineral is chemically and physically stable. It can be derived from weathering of continental rocks or through volcanism, and transported long distances before its deposition (Lovlie *et al.*, 1972). It is believed that the high magnetic susceptibility sections found in most cores can be attributed to the presence of detrital magnetite. Conversely, the low magnetic susceptibility sections would imply partial or complete absence of this highly magnetic mineral. Thus, the magnetite must have been altered to some less magnetic iron mineral or have been lost.

During sedimentological analysis of several cores located within the Bank Zone 1, sections with abundant pyrite concentrations were found. Pyrite was present in the form of separate grains of various sizes, as framboidal fillings of small sediment cavities and various kinds of foraminifera, as well as in the form of a complete replacement of foraminifer tests (Figure 4.16). The chemical replacement of foraminifera tests immediately implies that it occurred post-mortem and thus post-deposition. Because pyrite is a chemically and physically unstable mineral (Berner, 1967), it is very unlikely

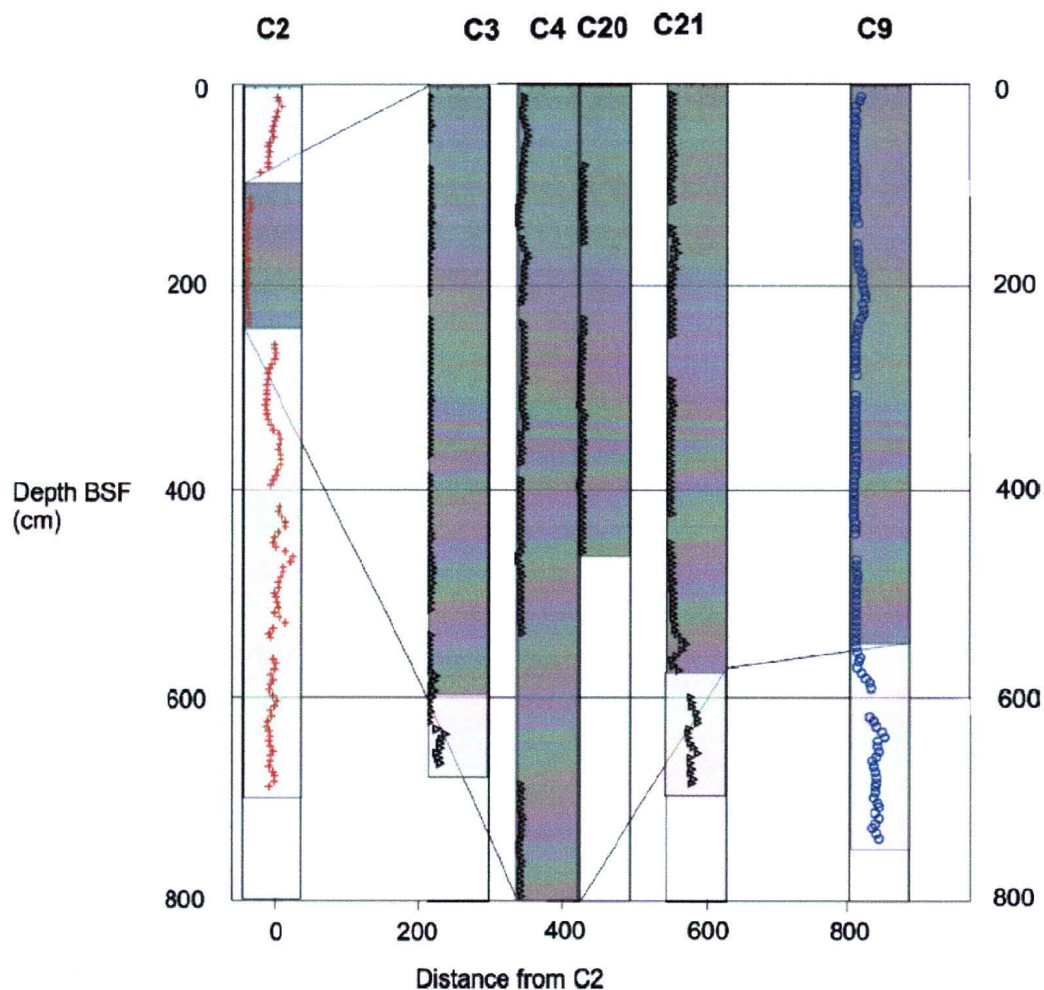


Figure 4.14. b) Magnetic Susceptibility (MS) over Blank Zone 1, Transect 2. The MS scale of each column spans from 0 to 5000. High MS values range from around 2500 to 3000 $\times 10^{-6}$ SI volume units, whereas Low MS values range from 300 to 800 $\times 10^{-6}$ SI volume units. Triangles represent cores located within the seismic blanking zone, circles represent cores located near the boundary of seismic blanking, and crosses represent cores located outside the blanking zone.

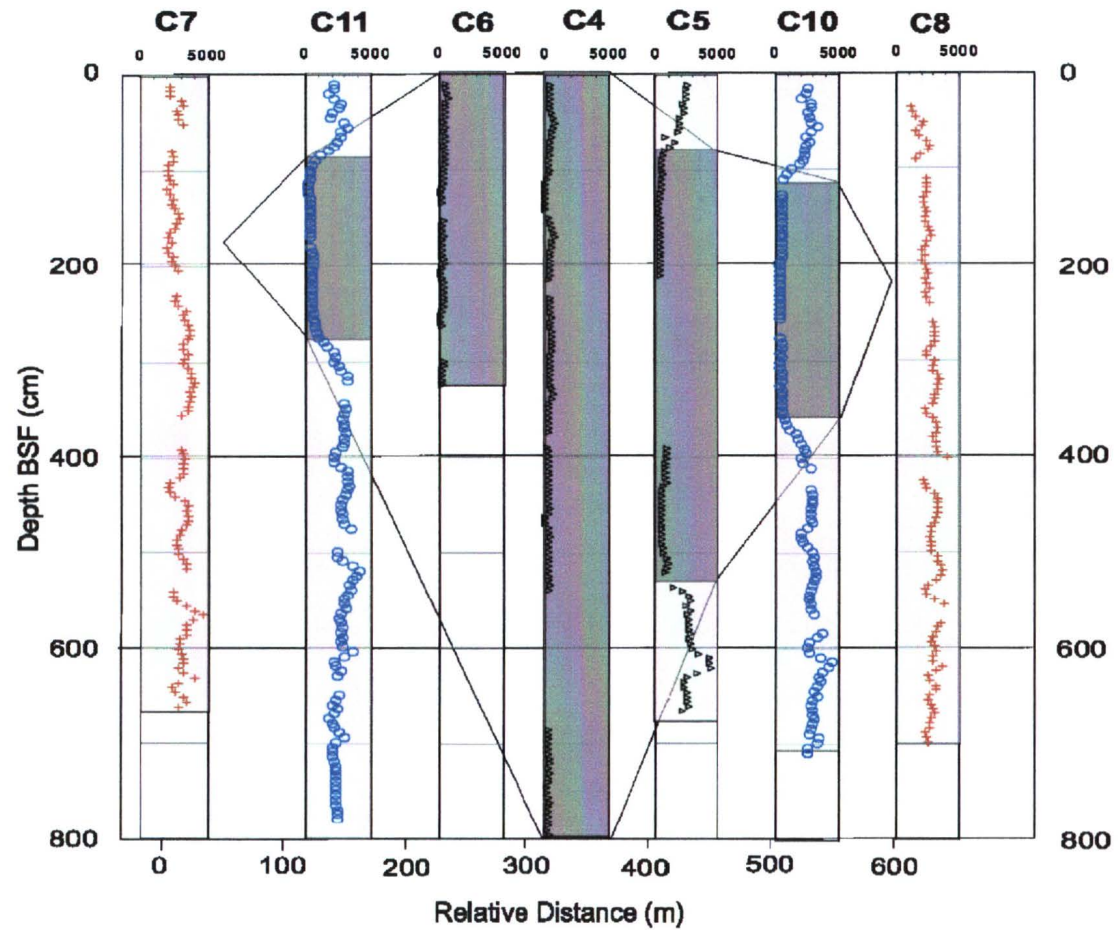


Figure 4.14. a) Magnetic susceptibility (MS) over Blank Zone 1, Transect 1. High MS values range from around 2500 to 3000×10^{-6} SI volume units, whereas Low MS values range from 300 to 800×10^{-6} SI volume units. Triangles represent cores located within the seismic blanking zone, circles represent cores located near the boundary of seismic blanking, and crosses represent cores located outside the blanking zone.

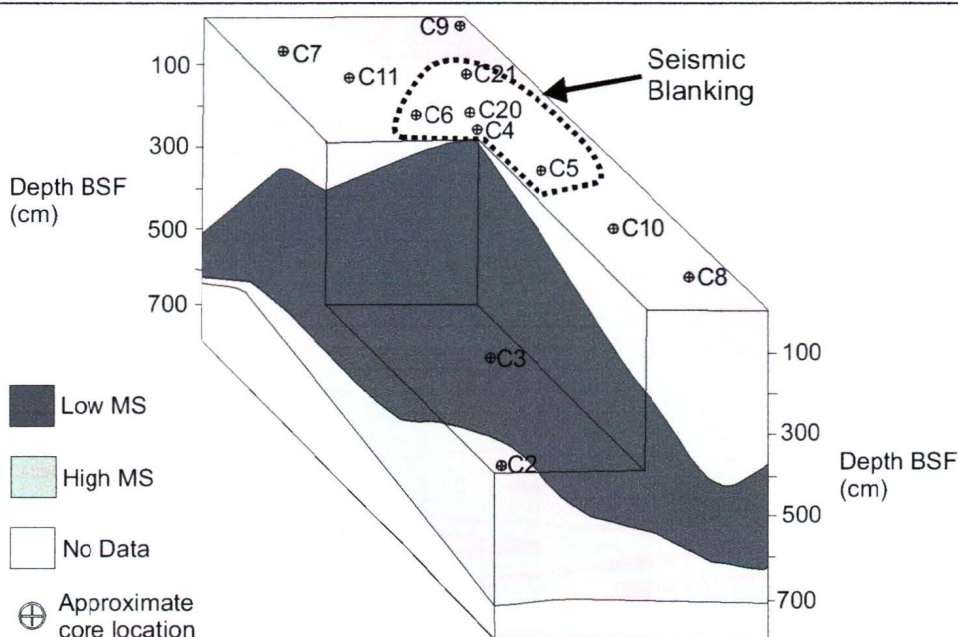


Figure 4.15. 3-D representation of the magnetic susceptibility zonation within the Blank Zone 1.

that it was transported and deposited in situ with the rest of the sediments. Furthermore, the delicate pyritized burrow casts and fragile nature of some pyrite definitely indicates lack of disturbance since its formation. Thus, we can assume that the pyrite found within these cores was formed as a result of diagenesis.

It has been suggested that dissolution of magnetite (Fe_3O_4) and formation of pyrite (FeS_2) can occur in anoxic marine sediments and is assisted by sulfate-reducing bacteria (Canfield and Berner, 1987). Sulfate is a common constituent of marine surface sediments. It is used by bacteria as a metabolic source for energy ($\text{SO}_4^{2-} + 2\text{CH}_2\text{O}$ (carbohydrate) $\rightarrow \text{H}_2\text{S} + 2\text{HCO}_3^-$). It is suggested that, in methane-rich environments, this reaction may be accompanied by also the microbially driven anaerobic methane oxidation reaction ($\text{SO}_4^{2-} + \text{CH}_4 \rightarrow \text{HS}^- + \text{HCO}_3^- + \text{H}_2\text{O}$) (Ritger *et al.*, 1987). In either case, dissolved sulfide will result. The iron ions from magnetite will then react with H_2S to produce initial iron sulfide, troilite (FeS), found in anoxic marine and lacustrine environments. Pyrite formation can be described through the following half-reaction (Berner, 1970):



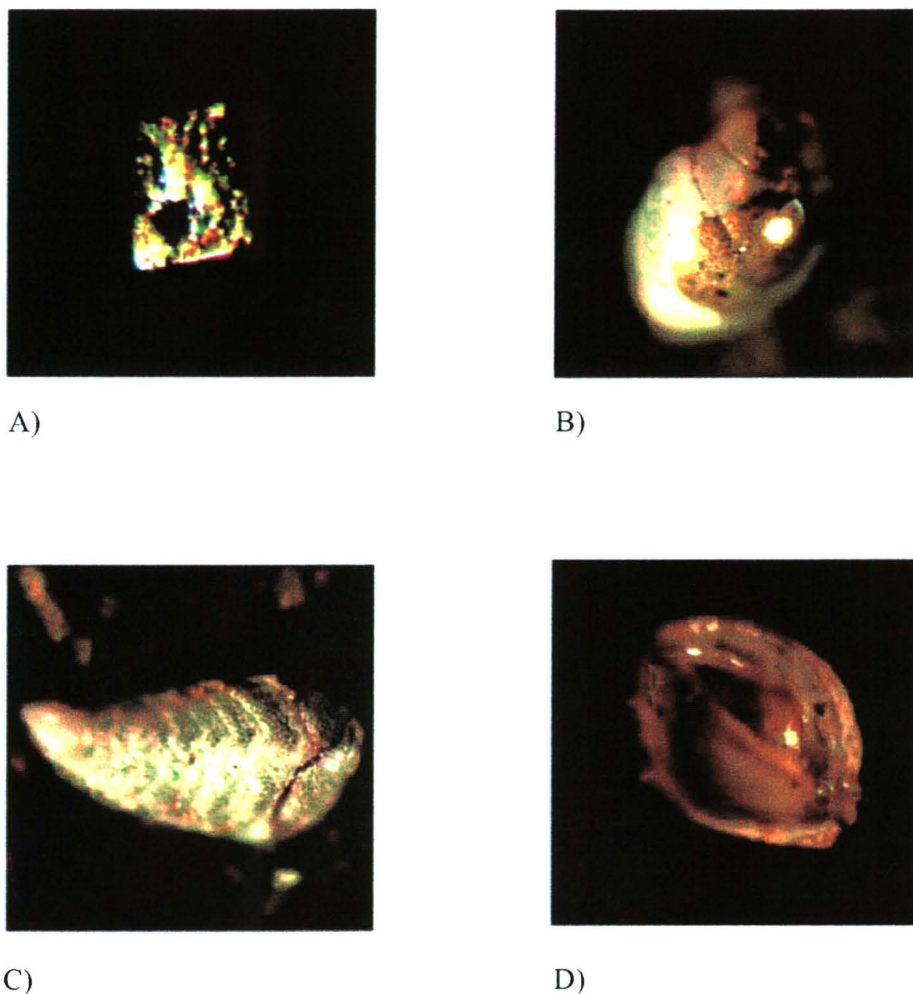


Figure 4.16. Evidence for detrital magnetite reduction. A) Euhedral authigenic pyrite grain. (B), (C), and (D) Pyritized benthic foraminifera (each photo spans 500 microns).

If not enough H_2S is present within the sediments, the reaction may terminate sooner, and the production of the intermediate mineral greigite (Fe_3S_4) may occur ($3\text{FeS} + \text{S}^0 \rightarrow \text{Fe}_3\text{S}_4$) (Berner, 1967). Thus, providing that magnetite is present within the sediment, the complete reduction of iron minerals into pyrite will occur only if there is a sufficient supply of sulfate and organic matter for the bacterial production of H_2S .

Sulfate is found in normal marine water in relatively high concentrations (Claypool and Kaplan, 1974). As it is being consumed by the sulfate-reducing bacteria, it is continuously being replenished by downward diffusion through the surface sediments. Thus, its concentration should not substantially vary laterally under normal conditions. The sulfate-reducing layer of most marine sediments begins tens of centimetres below the sea surface, just below the aerobic zone, and it extends a few metres below that. At this lower boundary, all the sulfate has been reduced by the bacteria, and it is thus termed 'depth to no sulfate'. The amount of sulfate reduction and the depth at which it terminates depends primarily on two factors: the amount of sulfate and the amount of organic matter within the sediment. Under normal marine conditions, organic matter, in form of various animals and plants, is continuously being deposited and buried with sediments. If the local conditions are stable, the amount of organic matter will not significantly change. Also, this supply will be laterally relatively uniform. Organic matter required for sulfate-reducing bacteria can also be supplied through addition of methane into the environment (see Thermal Conductivity Increase – Presence of Authigenic Carbonates section). In short, the more methane that is supplied, the more sulfate will be reduced (Berner, 1970). In situ bacterially-produced methane is limited and will easily be consumed and the depth to no sulfate will not change significantly (Kastner *et al.*, 1998). However, if the methane is being transported into the system from below, the depth to no sulfate will directly depend on the upward methane flux and its concentration. If the methane supply is great, the sulfate-reducing bacteria will not be able to oxidize all of it, and methane will migrate farther upwards, while shifting the depth to no sulfate with it. With upward methane flux, sulfate concentrations in seafloor sediments decrease linearly with depth, and the gradient becomes a measure of the upward methane flow rates (Borowski *et al.*, 1996). In addition, the methane supply will also reduce the seafloor aerobic layer, and allow sulfate reduction to extend upward to very close to the sediment-water interface (Musgrave and Hiroki, 2000).

In this study, the hydrate cores located in the centre of the seismic blanking have low magnetic susceptibility values throughout almost their entire length. This implies that the magnetite reduction to pyrite was complete even within the top sediments. In turn, this suggests that the seismic blanking area has been exposed to the greatest upward

methane supply. As the upward methane supply decreases away from the centre of the blanking, the top magnetite layer thickens, as indicated by the high magnetic susceptibility values. In an independent geochemical study using the same cores, Solem *et al.* (2002) conclude that in the area where gas hydrate was recovered, i.e., area of magnetic susceptibility low, the methane flux was significantly greater and the sulfate reduction zone was much shallower than farther away. In cores located even farther away from the centre, the methane supply is insufficient to produce pyrite in any part of the cored sediment section. This indicates a complete absence of magnetite reduction, or perhaps only a partial reduction into greigite which also has high magnetic susceptibility.

4.5.2. Magnetic Anomaly Expected From Low Magnetic Susceptibility Zone

The magnetic anomaly on a seafloor profile produced by the magnetic susceptibility low was examined using a geophysical forward modeling software GeoTutor. The magnetic susceptibility contrast between the susceptibility-low and the susceptibility-high zones was assumed to be 2000×10^{-6} SI volume units. Two scenarios were examined, one where the low-susceptibility body extends through 10 m of high-susceptibility sediment, and the other where the body extends downward for as much as 100 m of the sediment. In both cases, for the simplicity of the procedure, the body was assumed to be a prism. The body was chosen to extend 100 m in both x and y directions, or the approximate size of the actual zone, and to be buried by 5 m of high-susceptibility sediment, as it would be away from the immediate centre of the zone, with a total model width of ± 1000 m. The modeling results are seen in Figure 4.17.

Figure 4.17 (a) shows the expected magnetic anomaly produced by the shallower 10 m body. The negative anomaly is approximately 10nT, which is close to the resolution limit of the marine measuring equipment. The anomaly produced by the deeper-extending body is about 40nT, implying a large difference in magnetic strength of the two bodies. Although our data covers only the upper 8 m of sediment, the depth of the body could indeed extend to depth of 10s of metres below seafloor, and thus it may be possible to detect its magnetic signature, if the normal surrounding susceptibility is quite

uniform. Very high resolution seafloor magnetic mapping could thus be a tool for locating regions of high upward methane flux within sediments.

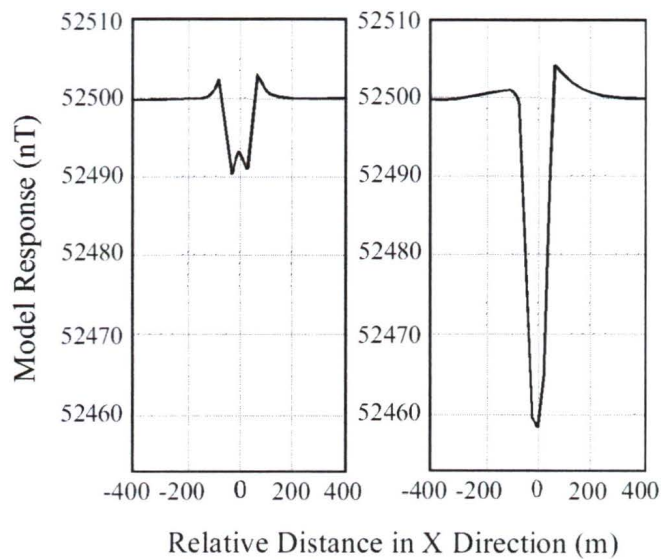


Figure 4.17. Model seafloor magnetic anomalies caused by a low-magnetic susceptibility object buried within the sediment 5 m below the seafloor. In both cases the object extends 100 m in X and Y directions and it differs from the surrounding sediment by -2000×10^{-6} SI volume units. (A) the object extends 10 m in Z direction and (B) the objects extends 100 m in Z direction.

CHAPTER 5

CONCLUSIONS AND FUTURE RECOMMENDATIONS

5.1. GAS HYDRATE SURFICIAL ENVIRONMENTS

Measurements on sediment cores have shown that seismic blank zones in the upper several 100 m of sediments are associated with high upward methane fluxes and concentrations. Gas hydrate was recovered in 4 cores located within the most prominent seismic blank zone (Blank Zone 1), a location associated with a seafloor mound that is believed to be the surface expression of a gas hydrate cap a few metres thick. Massive gas hydrate occurred at depths of 3-6 m, usually at the base of the core where the hydrate normally prevented further penetration. In most cores, sediments were highly gas-charged at depths greater than approximately 4 m and sediment displacement occurred due to gas expansion.

Cores that were located within blank zones contained authigenic pyrite that replaced magnetite and created a prominent low magnetic susceptibility zone within the vent. The remotely-operated submersible ROPOS was deployed at this vent site. Although no seafloor hydrate was observed, several areas of the vent field were found to be colonized by clams, tube worms, and bacterial mats, and composed of very hard carbonate pavement. Increased reflection coefficients and thermal conductivity values within the topmost sediments of Blank Zone 1 were consistent with the presence of authigenic carbonate. All observations are thus consistent with high methane concentrations and upward transport at a cold seep environment. A schematic representation of this environment can be seen in Figure 5.1.

The comparison of measured porosity, thermal conductivity, and velocity with deeper values from the Ocean Drilling Program (ODP) clearly indicates that within ~10 m of the seafloor the nature of sediment compaction is significantly different. Within these sediments porosity decreases from as much as 75% at the seafloor to 55% at 8 m below; in contrast, the inferred porosities using ODP values for the same depth extent (sections that were often disturbed) are consistently 60%. Moreover, thermal conductivity, being highly dependent on density and porosity, also increases with depth dramatically within the top few metres of the sediment. However, no significant decrease

in seismic velocity is observed over the same depth range. This particular behaviour of shallow sediments may be significant for: 1) various heat flow studies which use in situ thermal conductivity values, and 2) seafloor seismic impedance studies which depend on both velocity and density results, especially for higher frequency data which are more significantly affected by the properties of shallow sediments.

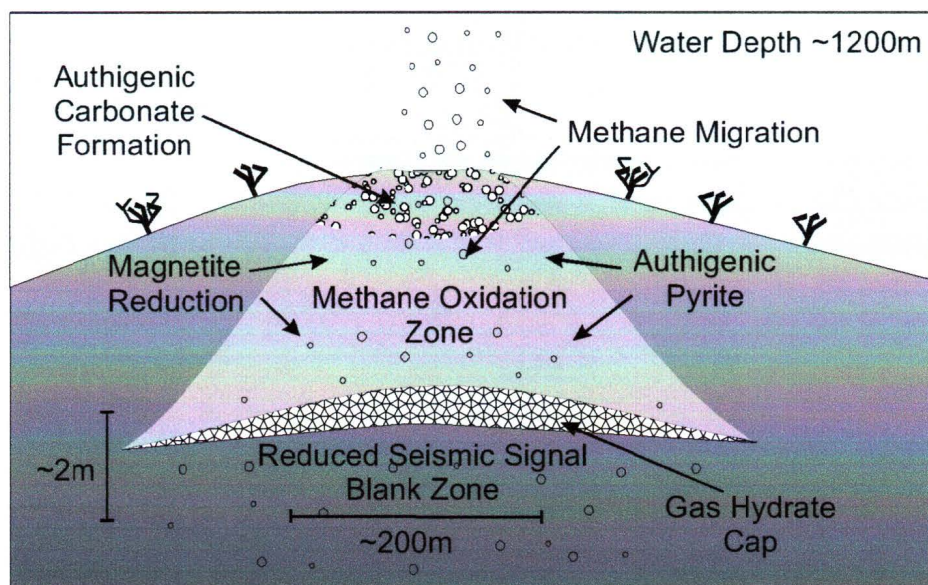


Figure 5.1. Possible cold vent environment at Blank Zone 1.

5.2. RECOMMENDATIONS FOR FUTURE WORK

5.2.1. Physical Properties

Proper sample collection and measurement is essential for high quality data. Correction or reduction of errors that occur during this step are costly and time consuming, and sometimes even uncorrectable. It is for this reason that a novice to a specific research should be introduced and prepared for data collection well in advance. However, this may not be always obtainable and thus other methods of precaution should exist. The following is a set of recommendations for physical property measuring procedure based on the work conducted and outlined in this study:

- 1) Magnetic susceptibility can potentially be highly diagnostic of sedimentological and mineralogical changes, and should thus be a part of any sediment analysis. The actual measurements are quick, non-destructive, and can be done on whole or split core. In this study, the magnetic susceptibility results allowed us to recognize high upward methane flux within the vent through geochemical/mineralogical changes within the sediment.
- 2) The upper approximately 10 m of the sediments likely experience different compaction levels than deeper sediments, and should thus be treated as a unique and separate unit. No significant compositional changes were observed down the length of the cores, and thus these differences are believed to be compactional and not compositional in nature. The large changes in porosity and density values over the top 10 m of sediment are not observed within the deeper sediments, and this can bring strong implications to other sediment properties such as thermal conductivity.
- 3) The Multi-Sensor Core Logger is a fast and efficient way of getting physical property data. Also the MSCL method is non-destructive and thus all the measurements can be conducted on the same sediment depth interval. This allows confident integration of different sediment properties. However, such equipment is very expensive, difficult to calibrate, fairly sensitive and delicate, and simple individual measurement devices may in the end be more reliable and more compatible for onboard research.

-
- 4) A major problem was encountered when taking sediment samples for density analysis using small metal plugs. The diameter of around 20 mm proved to be too small and produced unfilled plugs of varying sediment volume. The plugs were unfilled mostly due to the cohesion of clayey sediments to the rough stainless steel walls of the plugs. Larger ~30 mm plugs were completely filled with sediment most of the time. Thus, the walls of the density plugs should be smooth, possibly Teflon coated and at least 30 mm in diameter. Also, different methods, such as directly measuring weight and volume of the sample by water displacement, could also be used.

5.2.2. Marine Magnetic Anomaly

A new direction in gas hydrate research could be deep marine magnetic surveying. The low magnetic susceptibility zones, created due to high methane flux, could possibly be detected using high-resolution deep-towed or submersible-mounted magnetometers and thus be a new way of locating zones of venting and potential surficial gas hydrate deposits. The size and the depth of the magnetic anomaly could indicate the amount of the methane flux, assuming that large methane flux will reduce even newly deposited magnetite and thus produce a magnetic low at the seafloor.

REFERENCES

- Archie, G.E., 1947, Electrical resistivity- an aid in core analysis interpretation. *Bulletin AAPG*, v. 31, p. 350-360.
- Beaudet, F., Riedel, M., and Chapman, R., 2001, ROPOS Gas Hydrates, A seafloor survey at methane cold seeps offshore Vancouver Island, University of Victoria CEOR Report 2001-2.
- Bennett, R.H., Keller, G.H., and Busby, R.F., 1970, Mass property variability in three closely-spaced deep-sea sediment cores, *Journal of Sedimentary Petrology*, v. 40, no. 3, p. 1038-1043.
- Bennett, R.H., Ransom, B., Kastner, M., Baerwald, R.J., Hulbert, M.H., Sawyer, W.B., Olsen, H., Lambert, M.W., 1999, Early diagenesis: impact of organic matter on mass physical properties and processes, California continental margin, *Marine Geology*, v. 159, p. 7-34.
- Berner, R.A., 1967, Thermodynamic stability of sedimentary iron sulfides, *American Journal of Science*, v. 265, p. 773-785.
- Berner, R.A., 1970, Sedimentary pyrite formation, *American Journal of Science*, v. 268, p. 1-23.
- Berner, R.A., 1978, Sulfate reduction and the rate of deposition of marine sediments: *Earth and Planetary Science Letters*, v. 37, p. 492-498.
- Blunier, T., 2000, Frozen methane escapes from the sea floor, *Science*, v. 288, p. 68-69.
- Bohrmann, G., Greinert, J., Suess, E., and Torres, M., 1998, Authigenic carbonates from the Cascadia subduction zone and their relation to gas hydrate stability. *Geology*, v. 26, p. 647-650.
- Booth, J.S., and Dahl, A.G., 1986, A note on the relationship between organic matter and some geotechnical properties of a marine sediment, *Marine Geotechnology*, v. 6, no. 3, p. 281-297.
- Borowski, W.S. and Paull, C.K., Ussler III, W., 1996, Marine pore-water sulfate profiles indicate in situ methane flux from underlying gas hydrate, *Geology*, v. 24, n. 7, p. 655-658.
- Boudreau, B.P., 1998, Mean mixed depth of sediments: the wherefore and the why, *Limnology and Oceanography*, v. 43, no. 3, p. 524-526.

-
- Boyce, R.E., 1968, Electrical resistivity of modern marine sediments from the Bering Sea, *Journal of Geophysical Research*, v. 73, no. 14., p. 4759-4767.
- Brigaud, F. and Vasseur, G., 1989, Mineralogy, porosity and fluid control on thermal conductivity of sedimentary rocks, *Geophysical Journal*, v. 98, p. 525-542.
- Buffet, B.A. and Zatsepina, O.Y., 2000, Formation of gas hydrate from dissolved gas in natural porous media. *Marine Geology*, v. 164, p. 69-77.
- Canfield, D.E. and Berner, R.A., 1987, Dissolution and pyritization of magnetite in anoxic marine sediments, *Geochimica et Cosmochimica Acta*, v. 51, p. 645-659.
- Carcione, J.M. and Tinivella, U., 2000, Bottom simulating reflectors: seismic velocities and AVO effects, *Geophysics*, v. 65, p. 54-67.
- Carson, B., Wetstbrook, G.K., Mustgrave, J.R., Suess, E., eds., 1995, *Proceedings of the Ocean Drilling Program, Scientific Results 146 (pt. 1)*, College Station, TX, (Ocean Drilling Program).
- Chamov, N.P., and Murdamaa, I.O., 1995, Coarse fraction minerals of sands in Cascadia margin sediments, *in* Carson, B., Wetstbrook, G.K., Mustgrave, J.R., Suess, E., eds., *Proceedings of the Ocean Drilling Program, Scientific Results 146 (pt. 1)*, College Station, TX, (Ocean Drilling Program), p. 33-43.
- Chapman, R.N., Gettrust, J.F., Walia, R., Hannay, D., Spence, G.D., Wood, W.T., and Hyndman, R.D., 2002, High resolution deep towed multichannel seismic survey of deep sea gas hydrates off western Canada, *Geophysics*, v. 67, no. 4, p. 1038-1047.
- Claypool, G., and Kaplan, I.R., 1974, The origin and distribution of methane in marine sediments, *in* Kaplan, I.R., *Natural gases in marine sediments*, Plenum Publishing Corp., New York.
- Collett, T.C., 1998, Well log evaluation of gas hydrate saturations, *Transactions Society of Professional Well Log Analysts, Thirty-Ninth Annual Logging Symposium*.
- Collett, T.C., 1983, Detection and evaluation of natural gas hydrates from well logs, Prudhoe Bay, Alaska, *Proceedings of Forth International Conference on Permafrost*, p. 169-174.
- Collett, T.C. and Ladd, J., 2000, Detection of gas hydrate with downhole logs and assessment of gas hydrate concentrations (saturations) and gas volumes of the

-
- Blake Ridge with electrical resistivity log data, *in* Paull, C.K., Matsumoto, R., Wallace, P.J., and Dillon, W.P., eds., *Proceedings of the Ocean Drilling Program, Scientific Results 164*, College Station, TX, (Ocean Drilling Program), p. 179-192.
- Davis, E.E., Hyndman, R.D., Villinger, H., 1990, Rates of fluid expulsion across the northern Cascadia accretionary prism: constraints from new heat flow and multichannel seismic reflection data, *Journal of Geophysical Research*, v. 95, p. 8869-8889.
- Dickens, G., 2001, On the fate of the past gas: What happens to methane released from a bacterially mediated gas hydrate capacitor?, *Geochemistry, Geophysics, Geosystems, An Electronic Journal of Earth Sciences*, v. 2, 2000GC000131, (available at <http://www.g-cubed.org>)
- Dillon, W.P. and Max, M.D., 2000, Oceanic gas hydrate, *in* Max, M. D., ed., *Natural Gas Hydrate in Oceanic and Permafrost Environments*: Kluwer Academic Publishers [London], p. 61-76.
- Fink, C.R. and Spence, G.D., 1999, Hydrate distribution off Vancouver Island from multi-frequency single-channel seismic reflection data, *Journal of Geophysical Research*, v. 104, 2909-2922.
- Ganguly, N., Spence, G.D., Chapman, N.R., and Hyndman, R.D., 2000, Heat flow variations from bottom simulating reflectors on the Cascadia margin, *Marine Geology*, v. 164, p. 53-68.
- Gueguen, Y. and Palciauskas, V., 1994, *Electrical Conductivity-Conductivity of rocks*, *in* *Introduction to the Physics of Rocks*, Princeton University Press: Princeton, New Jersey.
- Guerin, G., Goldberg, D., Meltser, A., 1999, Characterization of in situ elastic properties of gas hydrate-bearing sediments on Blake Ridge, *Journal of Geophysical Research*, v. 104, p. 17781-17795.
- Haq, B.U., 2000, Climate impact of natural gas hydrate, *in* Max, M. D., ed., *Natural Gas Hydrate in Oceanic and Permafrost Environments*: Kluwer Academic Publishers [London], p. 137-148.

-
- Jarrard, R.D., MacKay, M.E., Westbrook, G.K., and Screaton, E.J., 1995, Log-based porosity of ODP sites on the Cascadia accretionary prism, *in* Carson, B., Westbrook, G.K., Mustgrave, J.R., Suess, E., eds., *Proceedings of the Ocean Drilling Program, Scientific Results 146 (pt. 1)*, College Station, TX, (Ocean Drilling Program), p. 313-335.
- Kastner, M., Sample, J.C., Whiticar, M.J., Hovland, M., Cragg, B.A., Parkes, J.R., 1995, Geochemical evidence for fluid flow and diagenesis at the Cascadia convergent margin, *in* Carson, B., Westbrook, G.K., Mustgrave, J.R., Suess, E., eds., *Proceedings of the Ocean Drilling Program, Scientific Results 146 (pt. 1)*, College Station, TX, (Ocean Drilling Program), p. 375-384.
- Kastner, M., Kvenvolden, K.A., and Lorenson, T.D., 1998, Chemistry, isotopic composition, and origin of a methane-hydrogen sulfide hydrate at the Cascadia subduction zone, *Earth and Planetary Science Letters*, v. 156, p. 173-183.
- Kennett, J.P., Cannariato, K.G., Hendy, I.L., and Behl, R.J., 2000, Carbon isotopic evidence for methane hydrate instability during Quaternary interstadials, *Science*, v. 288, p. 128-133.
- Kobayashi, K., and Nomura, M., 1972, Iron sulphides in the sediment cores from the Sea of Japan and their geophysical implications, *Earth and Planetary Science Letters*, v. 16, p. 200-208.
- Kvenvolden, K.A., 2000, Natural gas hydrate: Introduction and history of discovery, *in* Max, M. D., ed., *Natural Gas Hydrate in Oceanic and Permafrost Environments*: Kluwer Academic Publishers [London], p. 9-16.
- Kvenvolden, K.A., 1998, A primer on the geological occurrence of gas hydrate, *in* Henriot, J.-P., Mienert, J., eds., *Gas Hydrates: Relevance to World Margin Stability and Climatic Change*, Geological Society Special Publication No. 137, p. 9-30.
- Lewis, B.T.R. and Cochrane, G.C., 1990, Relationship between the location of chemosynthetic benthic communities and geologic structure on the Cascadia Subduction zone, *Journal of Geophysical Research*, v. 95, p. 8783-8793.

-
- Lewis, T.J., Villinger, H., and Davis, E.E., 1993, Thermal conductivity measurement of rock fragments using a pulsed needle probe, *Canadian Journal of Earth Sciences*, v. 30, no. 3, p. 480-485.
- Lister, C.R.B., 1979, The pulse-probe method of conductivity measurement. *Geophysical Journal*, v. 57, p. 451-461.
- Lovlie, R., Lowrie, W., and Jacobs, M., 1972, Magnetic properties and mineralogy of four deep-sea cores, *Earth and Planetary Science Letters*, v. 15, p. 157-168.
- MacDonald, I. R., Guinasso, N.L. Jr., Sassen, R., Brooks, L., Lee, J.M., and Scott, K.T., 1994, Gas hydrate that breaches the sea floor on the continental slope of Gulf of Mexico, *Geology*, v. 22., p. 699-704.
- MacKay, M.E., Jarrard, R.D., Westbrook, G.K., Hyndman, R.D., and the Shipboard Scientific Party of ODP Leg 164, 1994, Origin of the bottom simulating reflectors: Geophysical evidence from the Cascadia accretionary prism, *Geology*, v.22, p. 459-462.
- Makogon, Yu. F., Tsarev, V.I., and Cherskiy, V.V., 1972. Formation of large natural gas fields in zones of permanently low temperatures (in English): *Doklady Akademii Nauk SSSR*, v. 205, p. 700-703; *Doklady-Earth Science Section*, v. 205, p. 215-218.
- Markl, R.G., Bryan, G.M., Ewing, J.L., 1970, Structure of the Blake Bahama outer ridge, *Journal of Geophysical Research*, v. 75, p. 4539-4555.
- Matsumoto, R., Borowski, W.S., 2000, Gas hydrate estimates from newly determined oxygen isotopic fractionations (α_{GH-IW}) and $\delta^{18}O$ anomalies of the interstitial waters: Leg 164, Blake Ridge, *in* Paull, C.K., Matsumoto, R., Wallace, P.J., and Dillon, W.P., eds., *Proceedings of the Ocean Drilling Program, Scientific Results 164*, College Station, TX, (Ocean Drilling Program), p. 59-66.
- Matsumoto, R., Uchida, T., Waseda, A., Uchida, T., Takeya, S., Hirano, T., Yamada, K., Maeda, Y., and Okui, T., 2000, Occurrence, structure, and composition of natural gas hydrate recovered from the Blake Ridge, Northwest Atlantic, *in* Paull, C.K., Matsumoto, R., Wallace, P.J., and Dillon, W.P., eds., *Proceedings of the Ocean Drilling Program, Scientific Results 164*, College Station, TX, (Ocean Drilling Program), p. 13-28.

-
- Mi, Yanpeng, 1998, Seafloor sediment coring and multichannel seismic studies of gas hydrate, offshore Vancouver Island, M.Sc. Thesis, School of Earth and Ocean Science, University of Victoria, Victoria, BC, Canada.
- Minshull, T.A., Singh, S.C., and Westbrook, G.K., 1994, Seismic velocity structure at a gas hydrate reflector, offshore western Colombia, from full waveform inversion, *Journal of Geophysical Research*, v. 99, p. 4715-4734.
- Musgrave, R.J., and Hiroki, Y., 2000, Rock magnetism of the diapir sites (sites 991, 992, and 996), Caroline Rise and Blake Ridge, *in* Paull, C.K., Matsumoto, R., Wallace, P.J., and Dillon, W.P., eds., *Proceedings of the Ocean Drilling Program, Scientific Results 164*, College Station, TX, (Ocean Drilling Program), p. 401-409.
- Paull, C.K., Ussler, W., Dillon, W.P., 2000, Potential role of gas hydrate decomposition in generating submarine slope failures, *in* Max, M. D., ed., *Natural Gas Hydrate in Oceanic and Permafrost Environments: Kluwer Academic Publishers [London]*, p. 149-156.
- Paull, C.K., Ussler, W., Dillon, W.P., 1991, Is the extent of glaciation limited by marine gas hydrates, *Geophysical Research Letters*, v.18, p.432-434.
- Pellenbarg, R.E. and Max, M.D., 2000, Introduction, physical properties, and natural occurrences of hydrate, *in* Max, M. D., ed., *Natural Gas Hydrate in Oceanic and Permafrost Environments: Kluwer Academic Publishers [London]*, p. 1-8.
- Powell, R.W., Ho, C.Y., and Lilley, P.E., 1983, Thermal conductivity of certain liquids, *in* Weast, R.C., ed., *CRC handbook of chemistry and physics (64th edition): CRC Press, Boca Raton, Florida*, p. E-10.
- Riddihough, R.P., 1984, Recent movements of the Juan de Fuca plate system, *Journal of Geophysical Research*, v. 89, p. 6980-6994.
- Riedel, M., 2001, 3-D Seismic investigations of northern Cascadia marine gas hydrates, Ph.D. Thesis, School of Earth and Ocean Sciences, University of Victoria, Victoria, BC, Canada.
- Ritger, S., Carson, B., and Suess, E., 1987, Methane-derived authigenic carbonates formed by subduction-induced pore-water expulsion along the Oregon/Washington margin, *Geological Society of America Bulletin*, v. 98, p. 147-156.

-
- Sassen, R., Sweet, S.T., Milkov, A.V., DeFreitas, D.A., and Kennicutt II, M.C., 2001, Thermogenic vent gas and gas hydrate in the Gulf of Mexico slope: Is gas hydrate decomposition significant? *Geology*, v. 29, p. 107-110.
- Shipley, T.H., Houston, M.H., Buffler, R.T., Shaub, F.J., McMillen, K.J., Ladd, J.W., Worzel, J.L., 1979, Seismic evidence for widespread possible gas hydrate horizons on continental slopes and rises, *A.A.P.G. Bulletin*, v. 63, p. 2204-2213.
- Sibuet, M. and Olu, K., 1998, Biogeography, biodiversity and fluid dependence of deep-sea cold-seep communities at active and passive margins, *Deep-Sea Research Part II*, v. 45, p. 517-567.
- Sloan, Jr. E.D., 1998, Physical/chemical properties of gas hydrates and application to world margin stability and climatic change, *in* Henriot, J.-P., Mienert, J., eds., *Gas Hydrates: Relevance to World Margin Stability and Climatic Change*, Geological Society Special Publication No. 137, p. 31-50.
- Solem, R.C., Spence, G., Vukajlovich, D., Hyndman, R., Riedel, M., Novosel, I., and Kastner, M., 2002, Methane advection and gas hydrate formation within an active vent field offshore Vancouver Island, *Proceedings of the Fourth International Conference on Gas Hydrates*, Yokohama, May 19-23, 2002.
- Spence, G., Riedel, M., and Novosel, I., 2000, VENTFLUX: Piston coring and heat flow near vent sites associated with marine gas hydrates offshore Vancouver Island, Cruise PGC00-02: 10-24 July 2000, CGC John P. Tully, University of Victoria CEOR Report 2000-4.
- Suess, E., Bohrmann, G., Greinert, J., Lausch, E., 1999, Flammable ice, *Scientific American*, v. 281, n.5, p. 76-83.
- Stoll, R.D. and Bryan, G.M., 1979, Physical properties of sediments containing gas hydrates, *Journal of Geophysical Research*, v. 84, p. 1692-1634.
- Tinivella, U. and Accaino, F., 2000, Compressional velocity structure and Poisson's ratio in marine sediments with gas hydrate and free gas by inversion of reflected and refracted seismic data (South Shetland Islands, Antarctica), *Marine Geology*, v. 164, p. 13-27.
- Velde, B., 1996, Compaction trends of clay-rich deep sea sediments, *Marine Geology*, v. 133, p. 193-201.

-
- Wellsbury, P. and Parkes, J.R., 2000, Deep biosphere: Source of methane for oceanic hydrate, *in* Max, M. D., ed., *Natural Gas Hydrate in Oceanic and Permafrost Environments*: Kluwer Academic Publishers [London], p. 91-104.
- Westbrook, G., Carson, B., Musgrave, R., 1994, Shipboard Scientific Party, Initial Reports of the Ocean Drilling Program 146A, College Station, Texas.
- Whiticar, M., 1999, Carbon and hydrogen isotope systematics of bacterial formation and oxidation of methane, *Chemical Geology*, v. 161, p. 291-314.
- Xu, W. and Ruppel, C., 1999, Predicting the occurrence, distribution, and evolution of methane gas hydrate in porous marine sediments, *Journal of Geophysical Research*, v. 104, p. 5081-5095.
- Yuan, T., Spence, G.D., Hyndman, R.D., Minshull, T.A., and Singh, S.C., 1999, Seismic velocity studies of a gas hydrate bottom-simulating reflector on the northern Cascadia continental margin: Amplitude modeling and full waveform inversion, *Journal of Geophysical Research*, v. 104, p. 1179-1191.
- Yuan, T., Hyndman, R.D., Spence, G.D., and Desmons, B., 1996, Seismic velocity increase and deep-sea gas hydrate concentration above a bottom simulating reflector on the northern Cascadia continental slope, *Journal of Geophysical Research*, v. 101, p. 13655-13671.
- Yuan, T., Spence, G.D., and Hyndman, R.D., 1994, Seismic velocities and inferred porosities in the accretionary wedge sediments at the Cascadia margin, *Journal of Geophysical Research*, v. 99, no. B3, p. 4413-4427.
- Zatsepina, O.Y. and Buffett, B.A., 1998, Thermodynamic conditions for the stability of gas hydrate in the sea floor, *Journal of Geophysical Research*, v.103, p. 24127-24139.

APPENDIX A

Core Log

Core #	Latitude	Longitude	Day	Hour (GMT)	Water Depth (m)	Core Length (cm)	Section #	Depth of Section Top (cm)	Section Length (cm)	Comments	
<i>Test 1</i>	48 24.8472	123 25.3667	194	18:29:25	44.8	407	1	5	97		
							2	107	145		
							3	257	145		
<i>I</i>	48 38.9993	126 51.0106	196	17:56:55	1362	689	5	0	46	30 cm of sediment was lost	
							4	76	154		
							3	237	150		
							2	393	150		
							1	543	126		
							GRAVITY 1	1	56	20	
							2	76	39		
<i>2</i>	48 39.8699	126 51.2643	196	21:16:40	1280.2	692	5	0	100		
							4	100	145	presence of gas	
							3	250	155		
							2	410	145		
							1	560	132		
							GRAVITY 2	1	87	30	
<i>3</i>	48 39.39824	126 51.0874	197	15:38:18	1269.6	680	5	0	70		
							4	70	145		
							3	220	*155	*large quantities of gas	
							2	380	*145		
							1	530	*140		
							GRAVITY 3	1	60	55	
<i>4</i>	48 40.0317	126 51.0538	197	18:20:44	1272	834	6	0	145		
							5	150	84		
							4	234	150		
							3	389	157		
							2	541	145	empty	
							1	686	113	HYDRATE!!! b/w 804 and 829cm	
							GRAVITY 4	1	60	76	
<i>5</i>	48 39.9910	126 51.0150	197	22:17:35	1272	676	5	0	70		
							4	70	150		
							3	220	161		
							2	381	150		
							1	531	145		
							GRAVITY 5	1	0	75	

Core #	Latitude	Longitude	Day	Hour (GMT)	Water Depth (m)	Core Length (cm)	Section #	Depth of Section Top (cm)	Section Length (cm)	Comments
6	48 60.0637	126 51.1026	198	15:43:00	1266	893	6	0	144	
							5	149	126	
							4	260	44	
							3	334	258	empty
							2d	592	51	empty
							2c	643	48	Unconsolidated Sediment with HYDRATE chunks
6							2b	691	*42	
							2a	733	*40	
							1b	773	*52	*Carbonate
							1a	835	*58	
7	48 40.1771	126 51.1997	198	18:35:15	1269	676	5	0	69	Top ten cm are soupy green
							4	74	147	Gravity core 7 has ~15cm of liquidy green sediment on top of grey consolidated sediment
							3	226	154	
							2	386	145	
							1	536	140	
							GRAVITY 7	1	0	123
8	48 39.8872	126 51.9159	198	21:49:57	1279	712	6	0	3	empty
							5	3	70	
							4	105	150	
							3	255	159	
							2	414	150	
							1	564	148	
GRAVITY 8	1	0	126							
9	48 40.1999	126 50.7913	199	15:42:03	1262	759	5	0	87	
							4	150	150	
							3	300	145	
							2	457	152	
							1	609	147	
GRAVITY 9	1	88	140							
10	48 39.9477	126 50.9728	199	19:07:47	1274	718	5	0	121	
							4	121	145	
							3	271	153	
							2	429	145	
							1	579	139	
GRAVITY 10	1	60	75							
11	48 40.1181	126 51.1405	199	22:01	1269	790	5	0	180	
							4	180	150	
							3	330	159	

Core #	Latitude	Longitude	Day	Hour (GMT)	Water Depth (m)	Core Length (cm)	Section Number	Depth of Section Top (cm)	Section Length (cm)	Comments
							2	489	150	
							1	639	151	
						GRAVITY 11	1	0	108	
12	48 41.1996	126 52.1214	200	15:37:45	1259	710	5	0	123	
							4	128	130	top 10cm empty
							3	352	53	missing 94cm between S4 and S3
							2	410	145	
							1	360	140	
12						GRAVITY 12	1	50	68	
13	48 41.1739	126 52.3911	200	19:16:50	1267	575	4	0	145	
							3	150	123	
							2	278	145	
							1	428	147	
						GRAVITY 13	1	50	60	
14	48 41.1421	126 52.5725	200	22:14:50	1276	740	5	0	130	top 10cm empty
							4	130	150	
							3	280	158	
							2	438	150	
							1	588	152	bottom 7cm empty
14						GRAVITY 14	1	0	107	total length of core was 122, but 15cm were empty
15	48 41.0247	126 52.2261	201	16:01:28	1262	771	6	0	50	
							5	50	110	
							4	160	145	
							3	310	152	
							2	467	145	
							1	617	144	
						GRAVITY 15	1	50	53	
16	48 41.092	126 52.3042	201	19:10:31	1264	765	5	0	150	
							4	155	145	
							3	305	153	
							2	463	145	
							1	613	142	
						GRAVITY 16	1	50	75	
17	48 41.2686	126 52.4847	201	22:14:20	1275	669	5	0	58	
							4	58	150	
							3	208	159	
							2	367	150	
							1	517	151	
						GRAVITY 17	1	0	98	

Core #	Latitude	Longitude	Day	Hour (GMT)	Water Depth (m)	Core Length (cm)	Section Number	Depth of Section Top (cm)	Section Length (cm)	Comments
18	48 40.0228	126 51.1465	202	15:47:15	1267	257	1	5	102	HYDRATE in core catcher! NOTE: it is believed that the hydrate blocked the tube, thus only 2 sections were recovered
							2	112	100	
						GRAVITY 18	1	41	20	clam, tube worm holes, sea star, and carbonate
19	48 39.9409	126 51.0576	202	17:02:17	1271.8	705	5	0	97	
							4	97	145	
							3	247	153	
							2	405	145	
							1	555	140	
						GRAVITY 19	1	50	70	
20	48 40.0407	126 51.0174	202	21:46:35	1269	776	6	0	50	HYDRATE!!!
							5	70	96	
							4	171	145	
							3	321	153	
							2a	479	67	
							2b	559	26	disseminated hydrate
							2c	585	37	massive hydrate @ 110 and 135cm
							1	622	154	
						GRAVITY 20	1	0	104	tube worm hole b/w 9-12cm depth
21	48 40.0853	126 50.9573	203	16:16:25	1264.7	741	5	0	126	
							4	131	130	
							3	281	154	
							2	440	145	
							1b	590	109	
							1a	711	30	
						GRAVITY 21	1	68	70	
22	48 40.2536	126 51.3838	203	19:05	1266	880	6	0	125	
							5	212	42	
							4	290	145	unidentified solid found b/w S3 and S4 (Scripts' sample)
							3	440	154	
							2	599	145	
							1	749	131	
						GRAVITY 22	2	55	46	
							1	101	37	

Core #	Latitude	Longitude	Day	Hour (GMT)	Water Depth (m)	Core Length (cm)	Section Number	Depth of Section Top (cm)	Section Length (cm)	Comments
23	48 41.6183	126 49.1328	203	22:08:46	1421.7	692	6	0	125	Corrected Values-empty gaps were created due to layers being pulled apart during extraction; thus, 35cm and 92cm were cut off and subtracted from S4 and S1, respectively.
							5	130	80	
							4	215	110	
							3	330	153	
23							2	488	170	
							1	672	20	
							6	0	125	Original Values
							5	130	80	
							4	215	145	
							3	365	153	
							2	523	170	
							1	207	117	25cm of sand the rest is water
						GRAVITY 23	1	50	102	
24	48 40.9825	126 50.6635	204	19:15:02	1210.5	619	4	0	145	
							3	150	163	
							2	318	145	
							1	468	136	
						GRAVITY 24	1	42	82	
							2	0	42	
25	48 40.3746	126 52.7305	204	22:02:14	1291.1	610	4	0	145	
							3	150	154	
							2	309	145	
							1	459	145	
						GRAVITY 25	2	0	50	
							1	50	68	
26	48 39.9420	126 52.2650	205	15:42:21	1319.7	448	3	0	143	
							2	148	145	
							1	298	140	

APPENDIX B

General Core Description

CORE	SECTION	DESCRIPTION
1	1	No apparent cracks in upper portion Homogeneous mud (note: we could not get velocity)
2	2	Cracks, dark layers
	3	Cracks, dark layers; 17 –25 cm sandy layers
	4	Brown layers, homogeneous mud
	5	Soft mud, homogeneous
5	1	Many dark layers at top, cracked 92 cm to bottom not cracked and homogeneous no velocity
	2	Smeared orange gel at top, very dark layer at bottom; homogeneous layer from 17 –47 cm
	3	0 – 110 cm: mud with brown layers 110 – 125 some thin black layers
	4 – 5	No photos
6 (hydrate)	4 – 5	No photos
	6	Homogeneous mud
7	1	More greenish from 96 cm to bottom No apparent cracks
	2	39 –62 greenish layer
	3	Brown layers in homogeneous mud
	4	Brown layers in homogeneous mud
	5	Soupy at top, homogeneous mud below
8	1 – 2	No photos
	3	Brown layers in homogeneous mud
	4	Brown layers in homogeneous mud, darker at bottom
9	1	Cracked, black layers
	2	Black layers, brown layers, a few cracks Smeared orange gel from 52 – 59 cm
	3	Homogeneous mud, some layering, cracks at bottom
	4	Brown layers in homogeneous mud 113 – 114 dark triangular inclusion
	5	Brown layers in homogeneous mud
10	1	Cracked and dark layers
	2	Cracked and dark layers
	3	Brown layers, black layers and cracks at bottom
	4	Brown layers in homogeneous mud
	5	Homogeneous mud
11	1	Cracks at bottom
	2	Cracks, a few faint black layers ~ 1 cm thick
	3	A few dark layers, small cracks,

		more layering at bottom
	4	Brown layers, a few darker at bottom, At ~ 126 cm orange gel
	5	Brown layering
12	1	Cracks at bottom, thick black layers at top
	2	Thick black layers, cracked
	3	Brown layers at top, 8 cm long layer at bottom
	4	Brown layers
	5	Mud, brown layers at bottom
13	1	Cracks at bottom, smaller at top Long dark layers at top
	2	Very dark layering, a few cracks
	3	Brownish layers, faint black layers at bottom
	4	Soupy at top, brownish layers at bottom
14	1	Cracks and black layers
	2	Black layers, 2 – 10 thick
	3	Homogeneous mud, several black layers at base
	4	Brown layers
	5	Soupy at top, soft mud, splitting problems
15	1	Cracks, faint black layering
	2	Cracks, faint black layering
	3	Many dark bands at top, cracked at bottom
	4	Brown faint layering at top, black at bottom
	5	Homogeneous mud, faint layering
16	1	Cracked, a few black layers
	2	Large cracks at bottom, more consolidated at top
	3	Faint layering at top, more pronounced in middle
	4	Mud layers at top, black layers at bottom with cracks
	5	Top 10 cm soupy, homogeneous mud with faint layering
17	1 – 6	Numerous thin black layers
23	1 – 5	Numerous thin layers

APPENDIX C

Sedimentological Core Description

CORE 9 **Location: 48° 40.1999'** **126° 50.7900'** **Depth: 1262 m**

- *Laminated glaciomarine mud* - laminations range from millimetres to tens of centimetres with notable stiffening below about 105 cm with increased frequency of laminations.
- *Lithology* - clay to mud with some floating sand grains concentrated in particular laminae. Laminae colour grades from abrupt colour change to a darker reddish cast at bed tops grading to a greener tint with depth. Sand fraction + 45 microns has quartz, micas, lithic fragments, and discoid foraminifera for the entire core length.
- *Pyrite zone* – from 85 to 495 cm BSF. Pyrite forms include: cubes, disseminations, agglutinations, filaments and burrow casts.
- *Carbon zone*: from 342 to 742 cm. Characterized by dull earthy black carbon flecks.
- *Slime zone*: Pink slime occurs from 261 to 265 cm, 341 to 345 cm, and from 395 to 399 cm in small voids parallel to bedding. Orange slime occurs at 463 cm, and from 516 to 520 cm.

CORE 11 **Location: 48°40.1181'** **126°51.4105'** **Depth:1269 m**

- *Glaciomarine mud with occasional thin beds of fine sand and silt.*
- *Core scrapes* - Sand fractions of whole core scrapes contain dominant foraminifera with lesser diatoms (some infilled by carbon), sooty carbon balls, orange rusty limonite or palagonite balls, gelatinous whitish bacterial clots, and finer grained mineral silt dominated by quartz and mica with minor greenish glauconite pellets.
- *Slime zone* – 158 to 161 cm and 202 to 205 cm. Occurs in open vugs and bedding plane splits.
- *Pyrite zone* – 180 to 342 cm. Pyrite occurs as silt sized microcrystalline burrow casts, filaments, subcircular platelets, spherical aggregates of silt with pyritohedra, and pyritized globular.
- *Carbon zone* - 342 to 790 cm. Clots and balls of black carbon rich mud that are oxidizing to orange limonitic patches (the latter below 542 cm). Both the carbon and

limonite zones extend to 790 cm. The orange colour and oxidation appear to postdate the coring.

CORE 19 **Location: 48° 39.9409' 126° 51.0576' Depth: 1271.8m**

- *Finely laminated glaciomarine clays and silts.* Periodic layers containing fine to medium grained sand and rare coarser intervals with grit.
- *Core scrapes* - mostly mineral sand including quartz, 2 micas, rock fragments, yellowish green pale glauconite aggregates and about 25% foraminifera.
- *Slime Zone* - from 97 to 169 cm, at 142, 159, and 167 cm, from 323 to 395 cm. Occurs in open gas expansion fractures and cracks.
- *Pyrite Zone* – from 100 to 350 cm. Occurs as cubes, polycrystalline aggregates, framboidal masses, dendritic branches, filamentous strands, thin crystals, plates and films, both alone and as partial coatings on sand grains, replacing tests or coating foraminifera.
- *Upper Oxidized zone (0-169)* - laminated glaciomarine mud with thin sandy bands. Sand cut has up to 25% foraminifera, mostly glacial derived mineral and rock fragments and lesser amounts of glauconite from shelf.
 97-169 cm - open curving vertical fracture changing horizontal orientation along its length.
 143-169 cm - mostly banded gray and green mud with some yellow banding.
- *Carbon Zone* - from 342 to 693 cm. In some cases pyrite is intergrown in the carbon balls. Black charcoal coloured bands with sand sized dull black soft earthy carbonaceous spherules in > 45 micron fraction of sand wash. Carbon rich bands at 342, 352, and 382 cm.
- *Detailed sand washes* - conducted at several locations. Pyrite crystals are the largest, most ornate and most abundant along the walls of the open fractures containing the slime, especially where it crosses the high porosity sand bed. Occurrence of curved filaments of pyrite 1 mm long and 0.3 mm wide but most pyrite is in the 0.5 micron size range. Pyrite crystals, infillings and coatings are also more abundant in partially oxidized sediments than in reduced dark coloured sediments. Pyrite appears to be enhanced on open fracture faces and in more porous beds within the muddy

sediments. From 342 to 693 there are abundant carbon coated foraminifera of same species that were pyritized higher up the core and plain calcite at the top of the core. Appearance of small carbonaceous and limonite balls looking like "concretions" that grew in situ. The material that the concretions are composed of is dull black and earthy in appearance. The carbon balls are soft and break apart easily under the spatula. There is no evidence of regular internal structure, just uniformly carbon coated or carbon agglutinated silt and clay particles.

- ***Limonite Zone*** – from 555 to 695 cm. Dark gray moderately banded glaciomarine clays and silts with distinctive flecks of black carbon and orange limonite concentrated in bedding orientations like a series of small spots. Abundant horizontal gas cracks occur within this zone.

CORE 20 **Location: 48° 40.0407' 126° 51.0174' Depth:1269m**

- ***0 to 50 cm*** - Mottled light grey clayey to slightly sandy uniform glaciomarine mud
- ***70 to 96 cm*** - faintly laminated somewhat fractured brownish grey oxidizing glaciomarine mud.
- ***101 to 104 cm*** - a band of carbon
- ***171 to 316 cm*** - massive to intermittently laminated variably oxidized tan to grey to olive mud with some suspended fine sand and voids due to gas fractures and carbonate crusts removed. Occurrence of minor amounts of shell fragments. Whole core scrape and sand wash reveals quartz, mica, foraminifera and fragments thereof, and a few pebbles of tan/beige carbonate crusts that are soft and internally of very fine grain size. These carbonate crusts appear to be unique to the hydrate core site compared to non-hydrate cores.
- ***321 to 470 cm*** - dark, H₂S rich, comprised of laminated grey tan and brown mud with abundant gas fractures that make up about 15% of core stratigraphic thickness for this interval. A sand cut from the whole core scrape reveals foraminifera and very fine grained authigenic pyrite.
- ***622 to 776 cm*** - very disturbed olive grey to brown mud with about 40% horizontal voids and gas gaps. Whole core scrape has foraminiferal sand and mineral silt with larger rusty appearing authigenic limonite balls.

CORE 22 **Location: 48° 40.2536' 126° 51.3833'** **Depth: 1266 m**

- *0 to 120 cm* - soft hemipelagic mud. Rare mineral grains include quartz, magnetite, epidote and sphene.

- *280 to 440 cm* - alternating oxidized mineral rich pinkish tan mud and reduced grey mud. Foraminifera are dominantly pelagic with globular tests.

773 to 827 cm - periodic intensely dark charcoal-like bands occur in laminated glaciomarine sediment. The carbon bands occur deeper than in the blank zone possibly due to lower methane flux and a deeper onset of sulfate reducing bacteria

VITA

SURNAME: Novosel

GIVEN NAME: Ivana

PLACE OF BIRTH: Vukovar, Croatia, Europe

EDUCATIONAL INSTITUTIONS ATTENDED:

University of Victoria	2000-2002
McMaster University	1996-2000

DEGREES AWARDED:

B.Sc. Geology (Honours)	2000
-------------------------	------

HONOURS AND AWARDS:

CGU Best Student Paper Presentation Award	2002
CSPG Undergraduate Thesis Award	2000
The Murray Ball Scholarship in Geology, McMaster University	1999
The J.P. Bickell Bursary, McMaster University	1999
Dean's Honour List Award, McMaster University	1999 & 2000

PUBLICATIONS, CONFERENCES, AND WORKSHOPS:

Novosel, I., Spence, G.D., and Hyndman, R.D., 2002, Physical Properties of Gas Hydrate Related Sediments, Offshore Vancouver Island, EOS, Transactions, AGU, v. 83, no. 47 (poster).

Novosel, I., Spence, G.D., Hyndman, R.D., and Hamilton, T., 2002, Physical and Sedimentological Properties of Gas Hydrate Related Sediments, Scientific Meeting of the Canadian Geophysical Union, Banff, Alberta, Canada, May 2002 (presentation).

Novosel, I., Spence, G.D., Hyndman, R.D., and Hamilton, T., 2002, Physical and Sedimentological Properties of Gas Hydrate Related Sediments, Centre for Earth and Ocean Research Annual Research Workshop, February 2002 (presentation).

- Novosel, I., Spence, G.D., Chapman, N.R., Riedel, M., Hyndman, R.D., Solem, C., Kastner, M., and Hamilton, T., 2000, Piston coring and seafloor observations of gas hydrates at a vent field, EOS, Transactions, AGU, v. 81, no. 48, F603 (poster).
- Solem, R.C., Spence, G., Vukajlovich, D., Hyndman, R., Riedel, M., Novosel, I., and Kastner, M., 2002, Methane advection and gas hydrate formation within an active vent field offshore Vancouver Island, Proceedings of the Fourth International Conference on Gas Hydrates, Yokohama, May 19-23, 2002 (paper).
- Spence, G., Riedel, M., and Novosel, I., 2000, VENTFLUX: Piston coring and heat flow near vent sites associated with marine gas hydrates offshore Vancouver Island, Cruise PGC00-02: 10-24 July 2000, CGC John P. Tully, University of Victoria CEOR Report 2000-4 (report).
- Winters, W.J., Novosel, I., Boldina, O.M., Waite, W.F., Lorenson, T.D., Paull, C.K., Bryant, W., Physical Properties of Sediment Related to Gas Hydrate in the Northern Gulf of Mexico, EOS, Transactions, AGU, v. 83, no. 47 (poster).

UNIVERSITY OF VICTORIA PARTIAL COPY RIGHT LISCENCE

I hereby grant the right to lend my thesis to users of the University of Victoria Library, and to make single copies only for such users or in response to a request from the Library of any other university, or similar institution, on its behalf or for one of its users. I further agree that permission for extensive copying of this thesis for scholarly purposes may be granted by me or a member of the University designated by me. It is understood that copying or publication of this thesis for financial gain by the University of Victoria shall not be allowed without my written permission.

Title of Thesis:

Physical Properties of Gas Hydrate Related Sediments, Offshore Vancouver Island

Author: 

Ivana Novosel

December 2002

1
←
C6S6


2
←
C6S6

3
←
C6S6

4
←
C6S6

5
←
C6S6

6
←
C6S6



C7, S1



C7, S1



C7, S1



C7, S1



← C7S2

← C7S2

← C7S2

← C7S2



TOP SECTION



C7, S3
←

C7, S3
←

C7, S3
←

C7, S3
←

TOP OF SECTION

C7 S4



C7 S4



C7 S4



TOP OF SECTION



C7, S5
→

C7, S5
→



C9,SI
←

C9,SI
←

C9,SI
←

C9,SI
←

TOP OF SECTION



C9, S2
←

C9, S2
←

C9, S2
←

C9, S2
←

TOP SECTION

C9S3
←

C9S3
←

C9S3
←

15





TOP

C9, S4
←

C9, S4
←

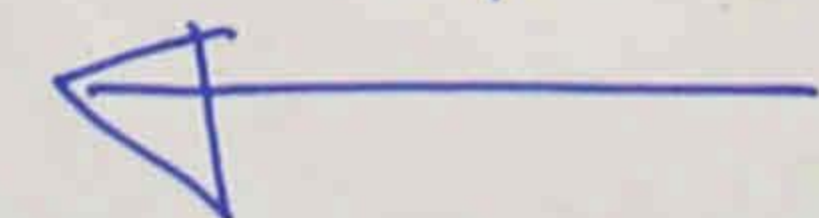
C9, S4
←

C9, S4
←

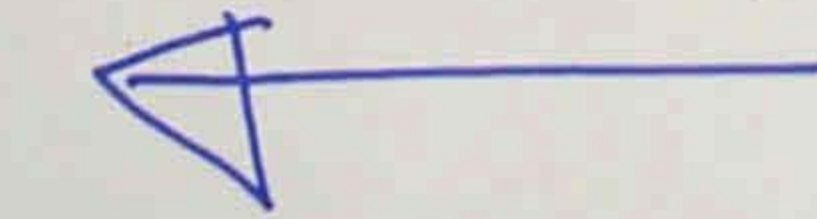
TOP OF SECTION



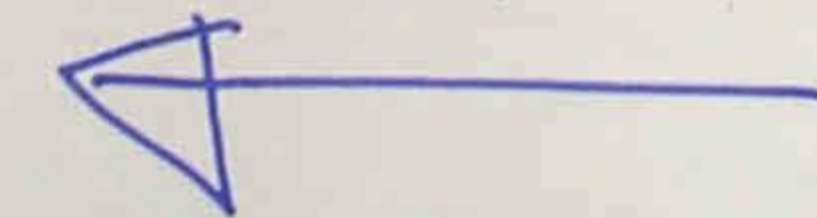
C9, S5



C9, S5



C9, S5



TOP OF SECTION

C10, S1
←

C10, S1
←

C10, S1
←

C10, S1
←



TOP SECTION



→
C10, S2

→
C10, S2

→
C10, S2

→
C10, S2

TOP SECTION

C10, S3
←

C10, S3
←

C10, S3
←

C10, S3
←



TOP OF SECTION



1
←
C10, S4

2
←
C10, S4

↑
↑

3
←
C10, S4

4
←
C10, S4

5
←
C10, S4

TOP OF SECTION


↔
C10, S5

↔
C10, S5

↔
C10, S5

↔
C10, S5

TOP OF SECTION



←
C11, S1

←
C11, S1

←
C11, S1

←
C11, S1

←
C11, S1

TOP OF SECTION



←
C11, S2

←
C11, S2

←
C11, S2

←
C11, S2

←
C11, S2

TOP OF SECTION



←
C11S3

←
C11S3

←
C11S3

←
C11S3

TOP OF SECTION

C11, S4



C11, S4




C11, S4



C11, S4





CISS
←

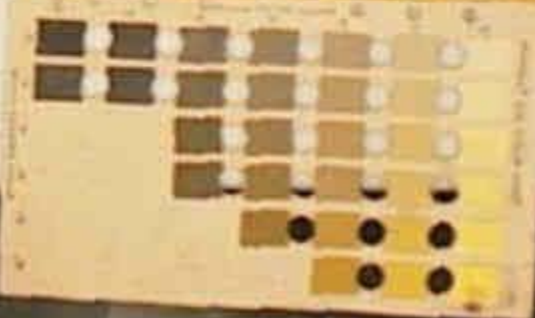
CISS
←

CISS
←

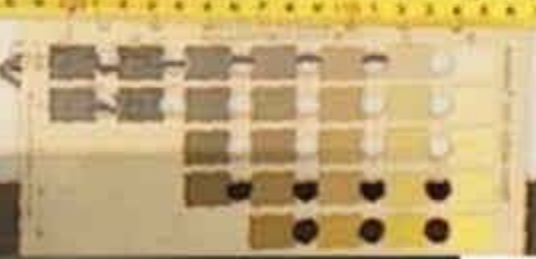
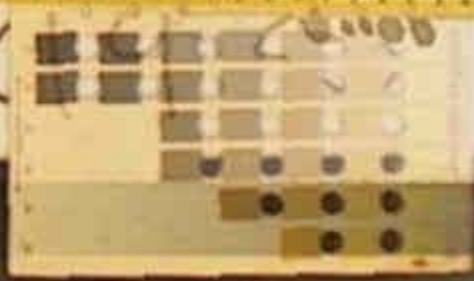
CISS
←

TOP

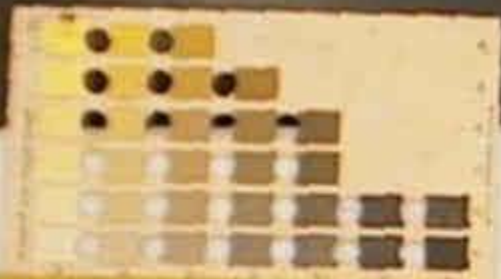
1-3750-511
1-3750-511
1-3750-511



●●●●●
C19 St
555-695



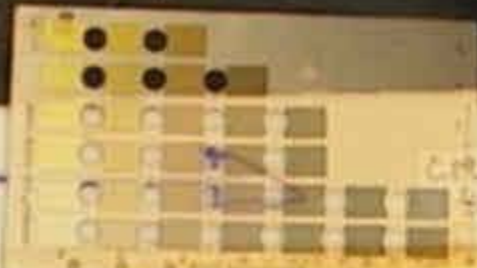
27
C19 St
555-695



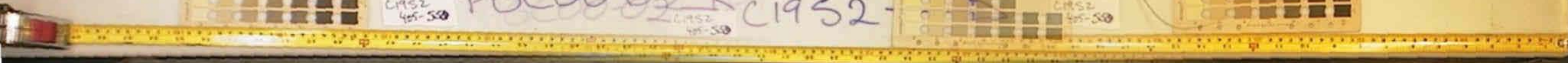
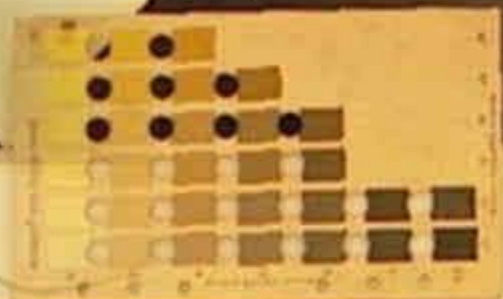
C1952
405-580

PGC00-02-1 C1952-

C1952
405-580



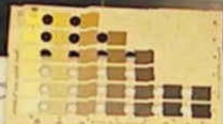
C1952
405-580



PGC00-02-1
C1952

53A

C1953A
325-400



00000





019538

PGC 1954

CASE
97-213

D C 1954

CASE
97-213



1954

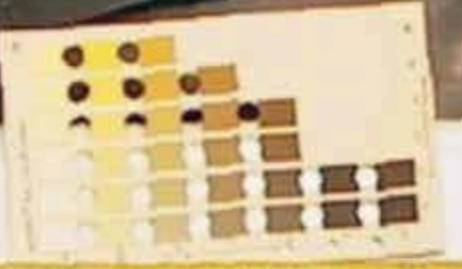


EXHIBIT 1
CASE 97-213

GC00-02

C1955 -

CASE
6-51



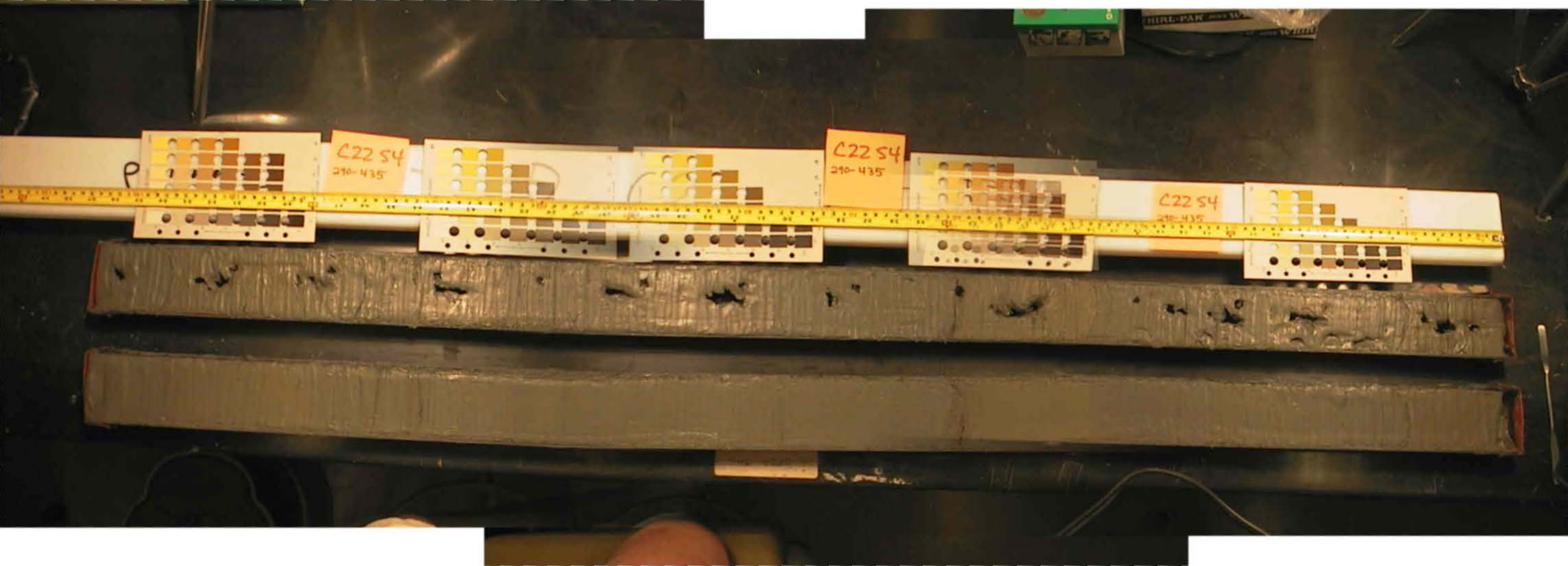
Small label with illegible text

PLC00-02

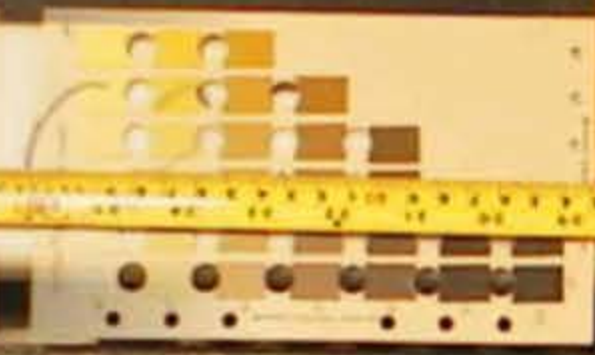
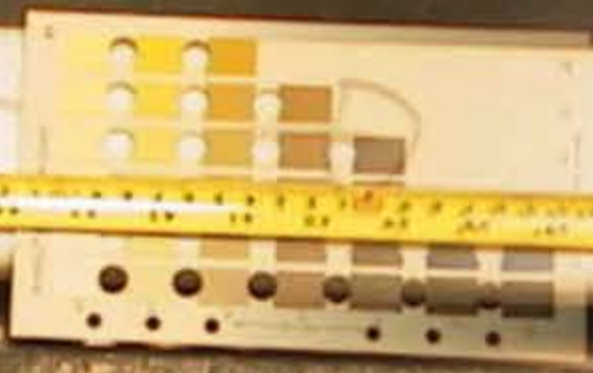
C72 S1

100

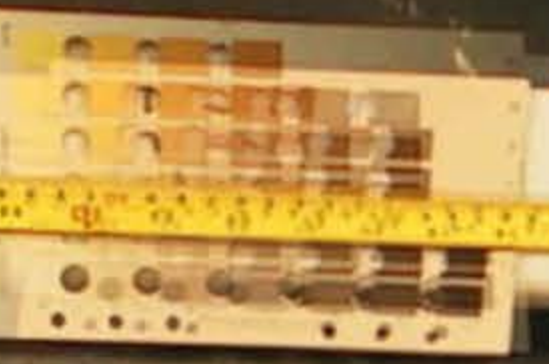




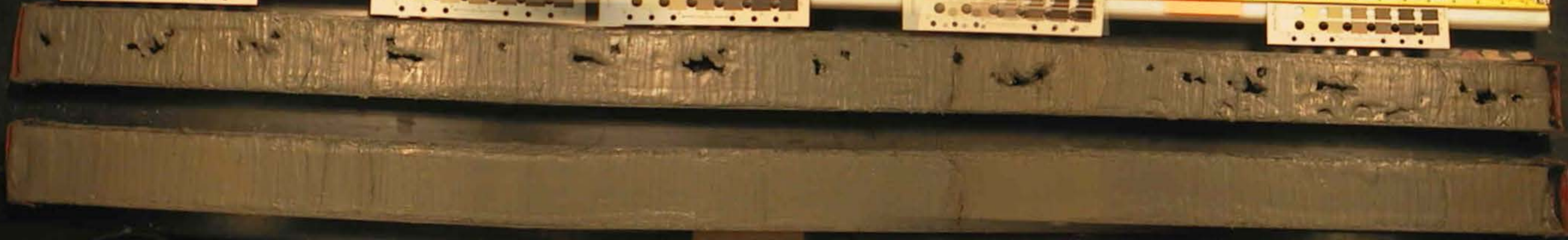
C22 S4
290-435



C22 S4
290-435



C22 S4
290-435



C2256
→

C2256
→



DON'T REUSE
THE CARD